

MASTER

**Impact of LES Subgrid-Scale Modeling on the
Acoustic and Flow Properties for Helmholtz
Resonators Without Mean Flow**

Autor:

QIN Yupeng

Matrikel-No:

03293504

Betreuer:

Killian Förner, M. Sc.
Prof. Wolfgang Polifke, Ph. D.

April 29, 2016

Erklärung

Hiermit versichere ich, die vorliegende Arbeit selbstständig verfasst zu haben. Ich habe keine anderen Quellen und Hilfsmittel als die angegebenen verwendet.

Ort, Datum

QIN Yupeng

Abstract

The impact of LES Subgrid-Scale (SGS) modeling on both acoustic and fluid dynamic properties is numerically investigated for Helmholtz Resonators without mean flow. Different available LES SGS models for compressible flow in OpenFoam are first examined theoretically. Nonlinear behavior in impedance and reflection coefficient are utilized for acoustic evaluation, while correlations and turbulent kinetic energy spectra, based on azimuthal velocity, are used for turbulent evaluation. The final comparison show very similar results for all implemented LES SGS models in OpenFoam in both acoustic and fluid dynamic properties. Only minor better conformance with experimental data is shown using the *SpalartAllmaras* model. The acoustic energy proportion absorbed in turbulence decreases with the growth of sound pressure level. These conclusions are confirmed for different Helmholtz Resonator geometries.

Contents

Nomenclature	v
1 Introduction	1
2 Theoretical Basis	3
2.1 LES Principle and Modeling	3
2.1.1 Governing Equations	3
2.1.2 Correlations	4
2.1.3 Energy Spectra	5
2.1.4 Filtered Navier-Stokes Equations	8
2.1.5 Subgrid-Scale Modeling	14
2.1.6 Wall Treatment	19
2.2 Basis Of Acoustics	21
2.2.1 Acoustic Equations	21
2.2.2 Helmholtz Resonator	22
3 Numerical Setup	24
3.1 PIMPLE with NSCBC	24
3.2 Test Cases	26
3.2.1 Hersh's Geometry	26
3.2.2 Förner's Geometry	30
4 Simulation Results	31
4.1 SGS Modeling Influence Of Acoustic Behavior	31
4.1.1 Correction SPL to AMP Transformation	33
4.1.2 Impact of SGS models	34
4.1.3 Nonlinear Resistance With Respect To SPL	37
4.2 Influence of The SGS Modeling on Turbulent Kinetic Energy Spectra and Correlation	40
4.2.1 Azimuthal Velocity	40
4.2.2 Correlations	42
4.2.3 Setting of Energy Spectra	45
4.2.4 Turbulent Kinetic Energy Spectra	48

4.2.5	Energy Spectra with different SPLs	50
4.2.6	Position and Mesh Quality Effect in Energy Spectra	51
4.3	SGS Comparison In Other Criteria	55
4.3.1	Visualization Through Vorticity and Q-Criterion	55
4.3.2	$k_{RES}/k_{SGS} = 4$ Criterion	56
4.4	Turbulence Judgment	58
5	Conclusion and Outlook	60
5.1	Conclusion	60
5.2	Outlook	61
	Appendices	62
A	Theoretical Deviations	63
A.1	Deviation of Helmholtz Resonator Equations	63
A.2	The Definition Of "pwelch" Function	66
A.2.1	Windowed PSD	67

Nomenclature

Roman Symbols

\bar{E}	Filtered Total Energy	$[\text{kg}\cdot\text{m}^2/\text{s}^2]$
\mathcal{D}_w	Windowed Power Spectra Density	$[\text{m}^2/\text{s}]$
$\mathcal{I}m$	Reactance	$[-]$
\mathcal{P}	Production of Residual Kinetic Energy	$[\text{m}^2/\text{s}^3]$
\mathcal{R}_f	Reflection Coefficient	$[-]$
$\mathcal{R}e$	Resistance	$[-]$
\mathcal{T}	Helmholtz Resonator Coefficient	$[-]$
\bar{K}	Filter Kinetic Energy	$[\text{m}^2/\text{s}^2]$
\bar{P}	Filtered Pressure	$[\text{Pa}]$
\bar{Q}_i	Redistribution and Dissipation of Kinetic Energy in Filtered Velocity Field	$[\text{m}^3/\text{s}^3]$
\bar{S}_{ij}	Filtered Strain Tensor Rate	$[\text{s}^{-1}]$
\bar{s}_{ij}	Strain Tensor Rate of Residual Velocity	$[\text{s}^{-1}]$
\bar{U}	Filter Velocity field	$[\text{m}/\text{s}]$
\hat{q}_i	Filtered Heat Flux Vector	$[\text{kg}\cdot\text{K}/\text{m}^2\cdot\text{s}]$
\hat{T}	Filtered Temperature	$[\text{K}]$
\hat{U}	Filtered Velocity	$[\text{m}/\text{s}]$
$\tilde{\Delta}$	Test Filter Width	$[\text{m}]$
$\tilde{\tilde{U}}$	Double Filtered Velocity	$[\text{m}/\text{s}]$
A_f	Pressure Amplitude	$[-]$

A_m	Orifice Area of Helmholtz Resonator	[m ²]
A_s	Coefficient in Sutherland's Law	[kg/(ms·K ^{0.5})]
A_{ca}	Cavity Area of Helmholtz Resonator	[m ²]
$B_{U_\theta U_\theta}$	Correlation	[m ² /s ²]
$B_{U_\theta U_\theta}^{norm}$	Normalized Correlation	[-]
c	Sound Velocity	[m/s]
C_k	Kolmogorov Constant	[-]
C_p	Specific Heat at Constant Pressure	[J/K·mol]
d_t	Distance to Nearest Trip Point	[m]
E	Total Energy	[kg·m ² /s ²]
$E(\kappa)$	Turbulent Kinetic Energy in Each Wavenumber Space	[m ³ /s ²]
E_{ij}	Dynamic Error Tensor	[m ² /s ²]
F	Mass Force	[N]
f	Frequency	[Hz]
F_w	Windowed Frequency in Matlab	[Hz]
f_μ	Damping Function	[-]
H_w	Windowed Discrete Fourier Transformed Signal	[-]
K	Kinetic Energy per unit Mass	[m ² /s ²]
k_{RES}	Resolved Filtered Kinetic Energy Spectra	[m ² /s ²]
k_{SGS}	Modeled Filtered Kinetic Energy Spectra	[m ² /s ²]
L	Characteristic Length	[m]
l_m	Orifice Length of Helmholtz Resonator	[m]
L_{no}	Window Length Without Overlapping in Frequency Space	[Hz]
L_o	Window Overlapping Length in Frequency Space	[Hz]
L_p	Sound Pressure Level	[dB]
L_w	Window Length in Frequency Space	[Hz]
L_{ij}	Leonard Stress	[m ² /s ²]

M	Mach Number	[-]
M_{sgs}	Mach Number in Subgrid-Scale	[-]
N	Windowed Frequency Number	[-]
P	Pressure	[Pa]
P^*	Fourier Transormed Pressure	[-]
P_w	Windowed Power Spectra Density in Matlab	[m ² /s]
Pr	Prandtle Number	[-]
Q'_i	Redistribution and Dissipation of Kinetic Energy in Residual Velocity Field	[m ³ /s ³]
R	Gas Constant	[J/(K·mol)]
Re	Reynolds Number	[-]
s	Entropy	[J/K]
S_{ij}	Strain Tensor	[s ⁻¹]
t	Time	[s]
T_s	Coefficient in Sutherland's Law	[K]
$T_{w,hole}$	Time Last In Simulation	[Hz]
T_{ij}	Eddy Viscosity of Sub-Test-Grid	[m ² /s ²]
U	Velocity	[m/s]
U'	Velocity Fluctuation	[m/s]
U'_{acou}	Velocity Fluctuation due to Acoustics	[m/s]
U'_{turb}	Velocity Fluctuation due to Turbulence	[m/s]
U^*	Fourier Transormed Velocity	[-]
U_θ	Azimuthal Velocity	[m/s]
$U_{\theta,rms}$	Velocity Square-root of Variance	[m/s]
V_{cell}	Volume of Grid	[m ³]
W	Window Number in Matlab	[-]
W_L	Window Overlapping Number in Matlab	[-]

x	Displacement	[m]
Z	Impedance	[-]
Greek Symbols		
$\bar{\sigma}_{ij}$	Filtered Viscous Stress Tensor	[kg/(m·s ²)]
χ	Viscosity Ratio in Spalart Allamras Model	[-]
Δt	Time Step	[s]
Δ	Filter Width	[m]
δ	Characteristic Flow Width	[m]
δ_t	Time Step between Two Time Poins	[s]
δ_U	Velocity Difference	[m/s]
δ_v	Viscous Length Scale	[m]
δ_w	Spacing along Wall to Trip Point	[m]
δ_x	Two-points Distance in x Direction	[m]
Δ_{cell}	Grid Length	[m]
δ_{ij}	Kronecker Delta	[-]
ϵ	Viscous Dissipation in Unresolved Scale	[m ² /s ³]
ϵ_{nl}	Resonator Loss Factor	[-]
η	Kolmogorov Motion Scale	[m]
γ	Specific Heat Ratio	[-]
κ, κ_n	wavenumber	[-]
λ	Thermal Conductivity	[kg·m/(K·s ³)]
μ	Dynamic Viscosity	[kg/(m·s)]
ν	Kinetic Viscosity	[m ² /s]
ν^*	Working Variable of Kinetic Viscosity	[m/s ²]
ω	Angular frequency	[rad/s]
ω_t	Vorticity at Trip Point	[s ⁻¹]
ω_{eig}	Resonator Eigenfrequency	[Hz]

$\bar{\epsilon}$	Viscous Dissipation in Resolved Scale	$[\text{m}^2/\text{s}^{-3}]$
$\bar{\rho}$	Filtered Density	$[\text{kg}/\text{m}^3]$
ρ	Density	$[\text{kg}/\text{m}^3]$
τ_{ij}^d	Residual Stress Tensor	$[\text{m}^2/\text{s}^2]$
τ_{ij}^r	Residual Stress Tensor	$[\text{m}^2/\text{s}^2]$
τ_w	Wall Shear Stress	$[\text{kg}/(\text{m}^2 \cdot \text{s})]$
τ_{ij}	Stress Tensor	$[\text{kg}/(\text{m} \cdot \text{s}^2)]$
θ_{maco}	Macrotemperature	$[\text{K}]$
ξ_{maco}	Macropressure	$[\text{Pa}]$
ζ	Loss Coefficient	$[-]$
u_τ	Friction Velocity	$[\text{m}/\text{s}]$

Acronyms

AMP	Amplitude Of Pressure
CFD	Computational Fluid Dynamics
CFL	Courant–Friedrichs–Lewy Number
DFT	Discrete Fourier Transform
DNS	Direct Numeric Simulation
EPSD	Empirical Power Spectral Density
GS	Grid Scale
LES	Large Eddy Simulation
NWM	Near Wall Modeling
NWR	Near Wall Resolution
PSD	Power Spectral Density
SGS	Subgrid-Scale
SPL	Sound Pressure Level
TKE	Turbulent Kinetic Energy

1 Introduction

Helmholtz Resonators were first used by Greeks to produce reverberation in open-air theaters [1]. As modern usage, it was utilized in turbofan aircraft engines to muffle inlet and exhaust noise [2]. The scientific interest in this resonator was thus stated as to understand the basic sound energy dissipation as well as to optimize the geometry for its utilized condition.

At lower sound pressure levels (SPL), acoustic energy is absorbed particularly by the resonator geometry through reflection within the resonator cavity. At higher SPL, the introduced acoustic perturbation promote flow separation especially at resonator necks, which can finally turn to turbulence by increasing the SPL. In such cases, turbulence also plays an important role in absorbing the input acoustic energy, which makes the resonator more efficient. This leads to the question how to quantify the influence of these structures in a Helmholtz Resonator.

Keller and Zauner [3] derived their mathematical model for Helmholtz Resonator from general resonators, where impedance and reflection coefficient serves to estimate acoustic properties. Hersh et al. [1] also provided a mathematical model from a basic force analysis, which is extremely complex to express. However, his experiment for that model can be used as referential experimental data. Förner did a lot of improvements [4–6] for that topic in Computational Fluid Dynamics (CFD) with OpenFoam based on Keller and Hersh’s works, but mainly in lower SPL and laminar conditions. For turbulence in higher SPLs, Zhang and Bodony [7] and Davidson [8] provided turbulent kinetic energy spectra and correlations as estimation tools for turbulent properties.

This thesis is concerned mainly with turbulent behavior in Helmholtz Resonator with higher SPLs with the simulation tool OpenFoam. Large Eddy Simulation (LES) approach is selected for those turbulence calculations, because it represents turbulence with high resolution and low computational cost in comparison to the Direct Numerical Simulation (DNS). As one of the most important parts in this work, different LES Subgrid-scales (SGS) models, that can be used in OpenFoam, will be investigated in detail. The setup of Helmholtz Resonator includes the part of acoustic theory, since the simulated turbulence is initially caused by acoustic perturbation. Discussion of result is therefore consist of acoustics and fluid turbulence estimations. For the evaluation of acoustic characteristics, the impedance and reflection coefficient with respect to frequency and SPL are used. As turbulent properties, correlations and TKE spectra will be used to judge SGS models both spatially and temporally.

In this thesis two different Helmholtz Resonator geometries are considered. The simulation according to these geometries are set up as in Hersh et al. [1] and Förner et al. [4], such that the given measurement can be used as experimental criteria to compare with the simulation results. These two geometries are used to confirm final conclusions, which are

targeted as follows:

- Compare the acoustic effect of different LES SGS models with the experimental result and conclude the optional choice for high SPL resonator.
- Compare the fluid dynamic effect of different LES SGS models and make judgment of the turbulence phenomenon.
- Discuss the advantage and disadvantage of each LES SGS model in simulation of Helmholtz Resonator.
- Make the judgment, whether the observed flow separation at resonator is turbulence.

2 Theoretical Basis

2.1 LES Principle and Modeling

Smagorinsky [9] first formulated the basic LES equations in early 1960's. Unable to resolve all the scales of motion due to limited computational resources, only large scales could be correctly resolved, and the impact of small scales has to be modeled following the theory of Kolmogorov's theory [10]. According to his result, the smallest motion scales were uniform and only drain energy from larger scales through the cascade process. These scales are thus successfully approximated rather than to be costly calculated. The large scales, which contain most of the energy, in the meanwhile, do most of transportation and are significantly affected by the boundary conditions should be calculated directly. This is the basic idea of LES.

2.1.1 Governing Equations

Fluid motion is governed by the Navier-Stokes Equations, which mainly describes the conservation of mass and momentum. In this thesis, Newtonian compressible fluid are considered. A Newtonian fluid is defined as the fluid whose viscous stress is linear to the velocity gradient vertical to the mean flow direction. A compressible fluid is defined as a fluid whose density can vary with time and space. The continuity equation can be formulated as follows [11]:

$$\frac{d\rho}{dt} + \rho \frac{\partial U_i}{\partial x_i} = 0, \quad (2.1)$$

where ρ stands for density, t for time, x for displacement, and U for velocity. The momentum transport equation presents the fluid particle mass times the acceleration equals the sum of acted forces. It can be expressed as [11]:

$$\rho \frac{dU_i}{dt} = -\frac{\partial P}{\partial x_i} + \frac{\partial \tau_{ji}}{\partial x_j} + \rho F_i = -\frac{\partial P}{\partial x_i} + \frac{\partial}{\partial x_j} \left(2\mu S_{ij} - \frac{2}{3}\mu \frac{\partial U_k}{\partial x_k} \delta_{ij} \right) + \rho F_i, \quad (2.2)$$

where P presents the pressure, F the mass forces, and μ dynamic viscosity. For Newtonian viscous fluids, the stress tensor τ_{ij} and the rate of strain tensor S_{ij} are defined as:

$$\tau_{ij} = 2\mu S_{ij} - \frac{2}{3}\mu S_{kk} \delta_{ij}, \quad (2.3)$$

$$S_{ij} = \frac{1}{2} \left(\frac{\partial U_i}{\partial x_j} + \frac{\partial U_j}{\partial x_i} \right). \quad (2.4)$$

Here, δ_{ij} denotes the Kronecker delta,

$$\delta_{ij} = \begin{cases} 1, & \text{if } i=j \\ 0, & \text{otherwise,} \end{cases} \quad (2.5)$$

The energy transport equation for a compressible flow can be formulated as [11]:

$$\rho \frac{d(I + K)}{dt} = \frac{\partial \sigma_{ji} U_i}{\partial x_j} - \frac{\partial q_i}{\partial x_i} + \rho U_i f_i, \quad (2.6)$$

where I donates internal energy which is usually ignored without large temperature change, and $K = (U_i U_i)/2$ the kinetic energy. The stress term σ_{ij} includes both the pressure stress and viscous stress:

$$\sigma_{ij} = -P\delta_{ij} + 2\mu S_{ij} - \frac{2}{3}\mu S_{kk}\delta_{ij}. \quad (2.7)$$

2.1.2 Correlations

Two-points Correlation

The two-points correlation is used to evaluate some turbulent length characteristics. The spatial power spectral density can be generated from two-points correlation with help of Fourier transformation. Take two points x^A and x^B with a distance of δ_x from one of the coordinate directions like x . The two-points correlation of velocity in azimuthal direction U'_θ can be written as [11]:

$$B_{U_\theta U_\theta}(x^A, \delta_x) = \langle U'_\theta(x^A) U'_\theta(x^B) \rangle = \langle U'_\theta(x^A) U'_\theta(x^A + \delta_x) \rangle, \quad (2.8)$$

with $\langle \cdot \rangle$ denoting an appropriate ensemble average. The normalized two-points correlation can be expressed like:

$$B_{U_\theta U_\theta}^{norm}(x^A, \delta_x) = \frac{\langle U'_\theta(x^A) U'_\theta(x^A + \delta_x) \rangle}{U_{\theta,rms}(x^A) U_{\theta,rms}(x^A + \delta_x)}, \quad (2.9)$$

where the index *rms* stands for square-root of variance:

$$U_{\theta,rms} = \langle U_\theta'^2 \rangle^{1/2}. \quad (2.10)$$

By homogeneous direction, the two-points correlation does not depend on the distance between the two selected points instead of the location of x^A . Thus $U'_{\theta,rms}(x^A) = U'_{\theta,rms}(x^A + \delta_x) = U'_{\theta,rms}$, Eq. (2.9) can be reduced to:

$$B_{U_\theta U_\theta}^{norm}(x^A, \delta_x) = \frac{\langle U'_\theta(x^A) U'_\theta(x^A + \delta_x) \rangle}{U_{\theta,rms}^2}. \quad (2.11)$$

Obviously, the correlation $B_{U_\theta U_\theta}$ increases when selected points are close to each other, and decrease when the distance become huge, see Fig. 2.1. The correlation $B_{U_\theta U_\theta}$ tends to zero when the distance between two points is large enough, such that the point x^A including eddies have no more influence of the velocity of point x^B . With negative influence in velocity, the correlation can also be smaller as zero. Thus, the normalized $B_{U_\theta U_\theta}^{norm}$ varies in a range of -1 to $+1$ with the distance between selected points as Fig. 2.1 shows.

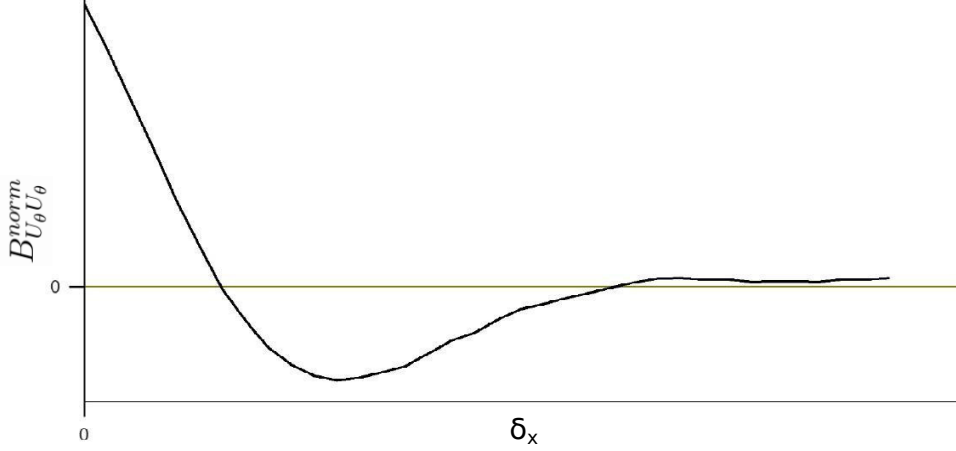


Figure 2.1: Sketch of typical two-points correlation.

Auto Correlation

The auto-correlation can be computed in only one location with different time steps. Similar as the derivation of two-points correlation, chose a two instances in time t^A and t^B with time step δ_t in between. The auto correlation of the velocity fluctuation in azimuthal direction U'_θ presents:

$$B_{U_\theta U_\theta}(t^A, \delta_t) = \langle U'_\theta(t^A)U'_\theta(t^B) \rangle = \langle U'_\theta(t^A)U'_\theta(t^A + \delta_t) \rangle. \quad (2.12)$$

In the situation of constant mean velocity, the homogeneous will also exist in "time direction", $B_{U_\theta U_\theta}$ will therefore no depend on time points, but only on time step δ_t . Thus a similar normalized auto-correlation over time can be formulated as:

$$B_{U_\theta U_\theta}^{norm}(\delta_t) = \frac{\langle U'_\theta(t)U'_\theta(t + \delta_t) \rangle}{U_{\theta, rms}^2}. \quad (2.13)$$

2.1.3 Energy Spectra

Since a wide range of scales can be observed in turbulent fluctuations, it is easier to evaluate the turbulence mechanisms with help of Fourier series. The presented discussion strictly follows Davidson [11]. With a general Fourier series, periodic function g with a period of $2L$ can be formulated as [11]:

$$g(x) = \frac{1}{2}a_0 + \sum_{n=1}^{\infty} (a_n \cos(\kappa_n x) + b_n \sin(\kappa_n x)), \quad (2.14)$$

where x acts as spatial coordinate and the Fourier coefficients are defined as:

$$\begin{aligned} a_n &= \frac{1}{L} \int_{-L}^L g(x) \cos(\kappa_n x) dx, \\ b_n &= \frac{1}{L} \int_{-L}^L g(x) \sin(\kappa_n x) dx, \end{aligned} \quad (2.15)$$

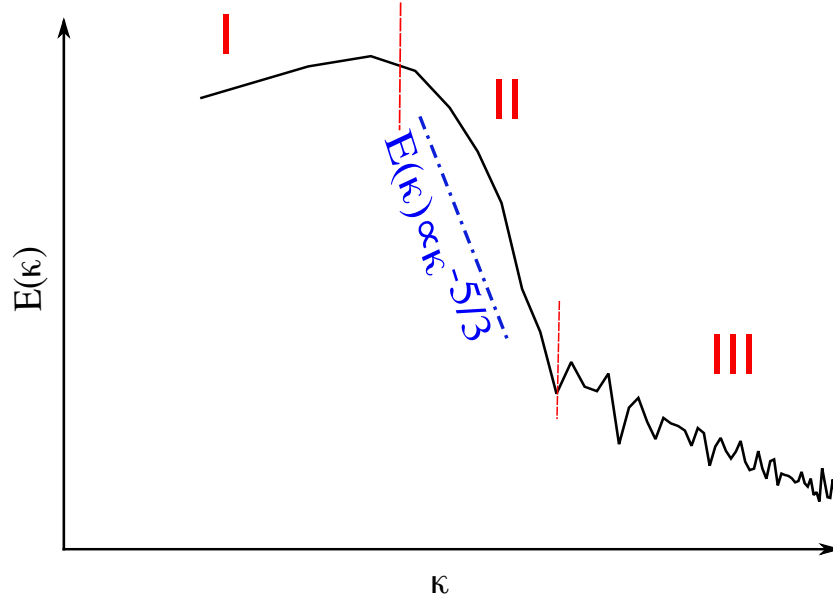


Figure 2.2: Spectrum for turbulent kinetic energy (TKE). I: Range for large energy eddies. II: The inertial subrange. III: Range for small, isotropic scales

where n reads the n^{th} harmonic wavenumber κ_n , with the definition:

$$\kappa_n = \frac{n\pi}{L} \quad \text{or} \quad \kappa = \frac{2\pi}{L}. \quad (2.16)$$

The largest wavenumber, that can be resolved is determined by the two grid lengths: $2\pi/(2\Delta_{\text{cell}})$. And the smallest wavenumber comes from the largest geometries scale, like in this thesis the resonator cavity length l_{ca} , which then be defined as: $2\pi/l_{ca}$.

The similar wavenumber transform is also available by analysis of turbulent kinetic energy $U'_i U'_i / 2$, which is more convenient to study in all eddy sizes in wave number space. The energy of each eddy in wavenumber can be expressed as:

$$E(\kappa)d\kappa, \quad (2.17)$$

where $E(\kappa)$ denotes the turbulent kinetic Energy by each wavenumber space. Thus the wavenumber can be treated as proportional to the inverse of an eddy's diameter. And a total turbulent kinetic energy turns to be the integrating of Eq. (2.17) of the whole wavenumber space:

$$K = \int_0^\infty E(\kappa)d\kappa = \sum_{n=0}^\infty (a_n^2 + b_n^2). \quad (2.18)$$

The distribution of turbulence kinetic energy in regards of its wave number is also called turbulent kinetic energy spectrum, as presented in Fig. 2.2. It can be separated to three regions: I, II, III:

I Region of large eddies that includes most of the energy. In this region the energy transfers from mean flow kinetic energy (in the situation of this thesis acoustic energy)

2.1 LES Principle and Modeling

to turbulent kinetic energy. This part of energy is called production term \mathcal{P} and defined in Eq. (2.40).

III Dissipation range. It is where the dissipation take place with small and isotropic eddies. At this part the turbulent kinetic energy transfers to inner energy with a governed parameter of ϵ , which is defined in Eq. (2.43).

II Inertial subrange. In this region, the middle sized eddy presents also as isotropic. Production from region I will be transfered to the dissipation part in region III through a transition process in this region. Thus a energy equivalence reads: $\mathcal{P} = \epsilon$. As larger eddies size in this region connect those from region I, while the smaller sizes connect those from region III, it can be imagine that turbulent kinetic energy in this region can be characterized by wavenumber κ and dissipation rate ϵ .

$$\begin{aligned} E &= \kappa^a \epsilon^b \\ [m^3/s^2] &= [1/m] [m^2/s^3] \end{aligned} \quad (2.19)$$

A simple dimensional analysis gives $b = 2/3$ and $a = -5/3$. so that

$$E(\kappa) = C_K \epsilon^{2/3} \kappa^{-5/3}, \quad (2.20)$$

where the C_K is called Kolmogorov constant $C_K \approx 1.5$. Eq. (2.20) is always called Kolmogorov spectrum law or simply $-5/3$ law. And the $-5/3$ decay in inertial region acts as a very important criterion in evaluating turbulent behaviors.

Alike the derivation in wavenumber space, Fourier series can be expressed in frequency space. Consider a periodic function h with a fundamental period of T and fundamental frequency of $f = 1/T$. The periodic function can be expressed as:

$$h(t) = \sum_{n=-\infty}^{\infty} c_n e^{i2\pi n f t} \quad (2.21)$$

where n also reads the n^{th} harmonic of fundamental frequency f_0 . The coefficient c_n can be computed as:

$$c_n = \frac{1}{T_0} \int_{T_0} h(t) e^{-i2\pi n f t} dt. \quad (2.22)$$

Thus, the turbulent kinetic energy in frequency space can be computed as:

$$k = \int_{-\infty}^{\infty} E(t) dt = \sum_{-\infty}^{\infty} |c_n|^2 = \sum_{n=-\infty}^{\infty} \mathcal{D}(n f_0). \quad (2.23)$$

$\mathcal{D}(n f)$ is the power Spectrum of $h(t)$. It is a series of coefficient, with each of them describes the contribution of the n^{th} harmonic fundamental frequency f . Since the connection of wave between space and time domain: wavenumber and frequency is proportional to each other: $f \propto \kappa$, the Kolmogorov's $-5/3$ law is also available in frequency space.

There are two ways to calculate the TKE spectrum from simulated velocity data in both wavenumber and frequency space:

- Calculate the discrete Fourier transform (like "fft" in Matlab) of every single velocity at the investigated points, and get the two-points covariant of these transformed velocities, which is actually twice the value of TKE.
- Calculate the two-points covariant of real velocities the $B_{U_\theta U_\theta}$ like in Sec. 2.1.2, and perform the discrete Fourier transform on this correlation. Still the final TKE value should be half of the transformed value.

Overmore the function of "pwelch" is usually preferred to calculate the power spectrum density (PSD) instead of discrete Fourier transform with "fft" function, since automatic data optimization is also made through the function of "pwelch" (detailed discussion in Sec. 4.2.3), so that the presentation of TKE shows less fluctuation in curves like "fft" function does.

2.1.4 Filtered Navier-Stokes Equations

In Direct Numeric Simulation (DNS), governing equations are computed down to the Kolmogorov motion scale η , which is the smallest scale of motion. However, in LES a low-pass filtering operation, which relates mainly to spatial grid properties is performed. The filter width Δ becomes thus a significant parameter and separates the whole flow into larger Grid Scale (GS) and the smaller Sub-Grid Scale (SGS). As its scale is larger than the defined filter width, the GS motion is resolved precisely, but the impact of SGS on GS has to be modeled as well. In the meanwhile with motion scale smaller than the filter width, SGS can be modeled without direct computation.

As mentioned above, every variable in LES consist of GS and SGS parts:

$$\underbrace{\bar{f}}_{GS} = f - \underbrace{f'}_{SGS}. \quad (2.24)$$

The general filtering operation can be used to exactly define the GS:

$$\bar{f}(x, t) = \int G(x, x', \Delta) f(x', t) dx', \quad (2.25)$$

where the filter function $G(x, x', \Delta)$ must satisfies the normalization condition:

$$\int G(x, x', \Delta) dx' = 1. \quad (2.26)$$

Figure 2.3 gives a comparison between filtered and unfiltered motion properties in both spacial space and spectral space.

Some of the most common filters include:

- The Top-Hat Filter, with its definition also in real space:

$$G(x, \Delta) = \begin{cases} \frac{1}{\delta}, & \text{if } |x'| \leq \frac{\Delta}{2} \\ 0, & \text{otherwise,} \end{cases} \quad (2.27)$$

where δ presents characteristic flow width. This is the most common choice for finite volume method, because the averages of flow variables over finite volume grid are linear functions of x , with the filter width of Δ

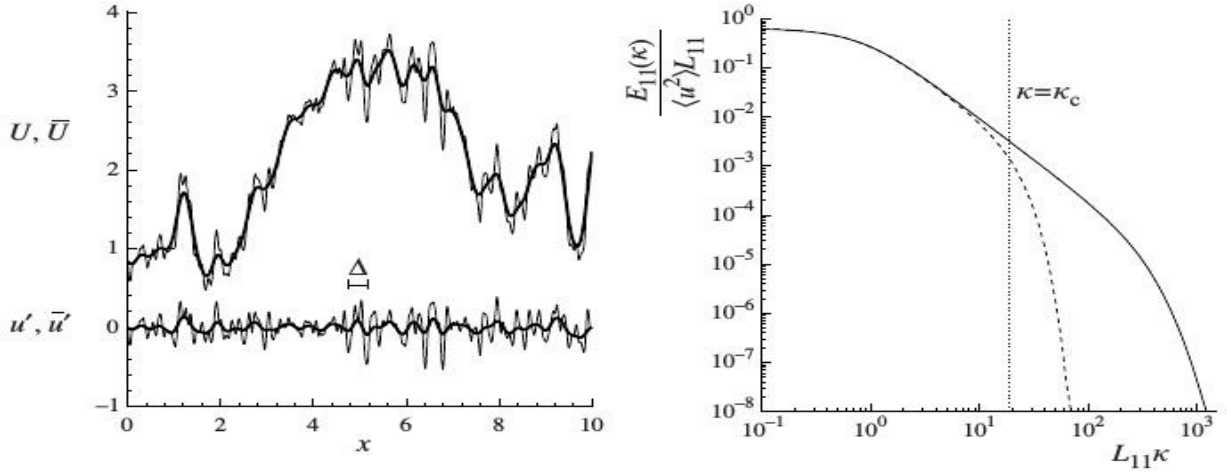


Figure 2.3: The filtered signal in spacial space (left) and spectral space (right) [12].

- The Sharp Fourier Cutoff Filter, with its definition in Fourier space:

$$\hat{G}(x, \Delta) = \begin{cases} \frac{1}{\delta}, & \text{if } \kappa \leq \frac{\pi}{\Delta} \\ 0, & \text{otherwise,} \end{cases} \quad (2.28)$$

where \hat{G} denote the Fourier coefficient of the filter function and κ the wavenumber. This model eliminates all the wave numbers above a chosen frequency, and hardly be applied to inhomogeneous flows. As it also does not smooth the resolved scales as the former two do, the Sharp Fourier Cutoff Filter is usually used in conjunction with spectral methods [13].

In smooth filter like the Top-Hat filter, the boundary between resolved scale and unresolved scale is not clearly defined, which results the SGS stress presenting the influence from both the resolved part and the unresolved part. In the meanwhile, the sharp Fourier cutoff filter serves as a clear separation between unresolved scale and resolved scale, so that the SGS stress presents only the effect from smaller scale on large ones. In this thesis a smooth filter (which can be defined in OpenFoam) is preferred for a relatively homogeneous calculated volume.

Filtered Incompressible Equations

At first, the filtered incompressible Navier-Stokes equations will be derived, with the ignoring of filter effects also in density ρ and pressure P . Only the velocity is considered. Thus, if we apply the filter operation of Eq. (2.24) on the velocity field, it can be defined as:

$$U(x, t) = \bar{U}(x, t) + u'(x, t), \quad (2.29)$$

where $\bar{U}(x, t)$ denotes the filtered velocity part and $u'(x, t)$ the residual (Sub-Grid Scale) part. In order to obtain the governing equations of filtered velocity field, the filter operation

should be applied on the Navier-Stokes Equation [12]. The continuity equation Eq. (2.1) can be filtered as:

$$\frac{\partial \bar{U}_i}{\partial x_i} = 0. \quad (2.30)$$

The filtered momentum equation can be rewrite from Eq. (2.2) as:

$$\frac{\partial \bar{U}_j}{\partial x_i} + \frac{\partial \bar{U}_i \bar{U}_j}{\partial x_i} = \nu \frac{\partial^2 \bar{U}_j}{\partial x_i^2} - \frac{1}{\rho} \frac{\partial \bar{P}}{\partial x_j}. \quad (2.31)$$

It is quite important to distinguish between the filtered product $\overline{U_i U_j}$ and the product of filtered velocities $\bar{U}_i \bar{U}_j$ here. The difference between these two is defined as residual stress tensor [12]:

$$\tau_{ij}^r = \overline{U_i U_j} - \bar{U}_i \bar{U}_j. \quad (2.32)$$

The residual stress tensor is related to the residual (Sub-Grid Scale) kinetic energy k_{SGS} as $\tau_{ii}^r = 2k_{SGS}$. The deviatoric stress tensor τ_{ij}^d can be derived from residual stress tensor as:

$$\tau_{ij}^d = \tau_{ij}^r - \frac{2}{3} k_{SGS} \delta_{ij}, \quad (2.33)$$

In tensor analysis, tensor A_{ij} can be write as the summation of deviatoric part and hydrostatic (residual) part as $A_{ij} = A_{ij}^d + A_{ij}^r$, where the hydrostatic part is defined as $A_{ij}^r = \frac{1}{3} A_{ii} \delta_{ij}$, and so the deviatoric part as $A_{ij}^d = A_{ij} - \frac{1}{3} A_{ii} \delta_{ij}$ [14]. In order to include the hydrostatic residual stress into filtered momentum equation, a modified filtered pressure is defined as $\bar{P} = \bar{P} + \frac{2}{3} k_{SGS}$. So that the filtered momentum equation formulates as:

$$\frac{\partial \bar{U}_j}{\partial t} + \bar{U}_i \frac{\partial \bar{U}_j}{\partial x_i} = \nu \frac{\partial^2 \bar{U}_j}{\partial x_i^2} - \frac{\partial \tau_{ij}^r}{\partial x_i} - \frac{1}{\rho} \frac{\partial \bar{P}}{\partial x_j}. \quad (2.34)$$

By comparison of the non-filtered (2.2) and the filtered (2.34) momentum equations, an extra unknown quantity τ_{ij}^r is observed, that makes the whole equation a not closed one. It therefore must be modeled for further computation. In this thesis, it will be discussed how this term can be modeled with different methods. In deviation of filtered energy conservation equation, kinetic energy K can be first filtered as:

$$\bar{K} = \frac{1}{2} \overline{U_i U_i} = k_{RES} + k_{SGS}, \quad (2.35)$$

where k_{RES} and k_{SGS} present the resolved part and Sub-Grid part of kinetic energy respectively. They can be defined as:

$$k_{RES} = \frac{1}{2} (\bar{U}_i \bar{U}_i), \quad (2.36)$$

$$k_{SGS} = \bar{K} - k_{RES} = \frac{1}{2} (\overline{U_i U_i} - \bar{U}_i \bar{U}_i) = \frac{1}{2} \tau_{ii}^r. \quad (2.37)$$

By combination of Eqs. (2.6), (2.36) and (2.37), the energy conservation equations for k_{GS} and k_{SGS} can be deduced as [12]:

$$\frac{\partial k_{RES}}{\partial t} + \bar{U}_i \frac{\partial k_{RES}}{\partial x_i} = -\frac{\partial \bar{Q}_i}{\partial x_i} - \mathcal{P} - \bar{\epsilon}, \quad (2.38)$$

2.1 LES Principle and Modeling

$$\frac{\partial k_{SGS}}{\partial t} + \bar{U}_i \frac{\partial k_{SGS}}{\partial x_i} = -\frac{\partial Q'_i}{\partial x_i} + \mathcal{P} - \epsilon. \quad (2.39)$$

Here, \mathcal{P} presents the production of residual kinetic energy:

$$\mathcal{P} = -\tau_{ij}^d \bar{S}_{ij}, \quad (2.40)$$

where \bar{S}_{ij} is the filtered strain tensor rate:

$$\bar{S}_{ij} = \frac{1}{2} \left(\frac{\partial \bar{U}_i}{\partial x_j} + \frac{\partial \bar{U}_j}{\partial x_i} \right). \quad (2.41)$$

The production term acts as a sink term in resolved kinetic energy conservation (2.38), and as a source term in unresolved kinetic energy conservation (2.39). Because the energy in this term is transferred from the large scale (filtered and resolved velocities) to the small scales (residual and unresolved velocities) [12]. The viscous dissipation terms are defined respectively as:

$$\bar{\epsilon} = 2\nu \bar{S}_{ij} \bar{S}_{ij}, \quad (2.42)$$

$$\epsilon = 2\nu \bar{s}_{ij} \bar{s}_{ij}, \quad (2.43)$$

where \bar{s}_{ij} is the filtered strain tensor rate of residual velocities:

$$\bar{s}_{ij} = \frac{1}{2} \left(\frac{\partial \bar{u}'_i}{\partial x_j} + \frac{\partial \bar{u}'_j}{\partial x_i} \right). \quad (2.44)$$

The term $\bar{\epsilon}$, the viscous dissipation directly from the filtered velocity field is relatively small compared with ϵ the viscous dissipation from the residual velocity field. This means that most energy is dissipated in the sub-grid scales [12]. The term \bar{Q}_i and Q'_i represent the redistribution and the dissipation of kinetic energy in filtered and residual velocity fields:

$$\bar{Q}_i = \bar{U}_j \left(2\nu \bar{S}_{ij} - \tau_{ij}^d - \frac{\bar{P}}{\rho} \delta_{ij} \right), \quad (2.45)$$

$$Q'_i = \bar{U}_j \left(2\nu \bar{s}_{ij} - \tau_{ij}^d - \frac{\bar{P}}{\rho} \delta_{ij} \right), \quad (2.46)$$

where the first terms represent diffusion while the other two represent energy redistribution by velocity and pressure fluctuations.

As a criterion for the LES with near-wall resolution, 80% of the kinetic energy should be resolved while other 20% be modeled, which means $k_{RES}/k_{SGS} > 4$ [15]. To fulfill this requirement the grid width should not be too coarse to resolve 80% energy, otherwise the simulation is more strongly dependent on the SGS modeling. That topic will be discussed deeply later in Sec. 2.1.5.

Compressible Filtered Equations

With the above preparation of LES definition in incompressible flows, we now consider more about the compressible flows. The main difference between compressible and incompressible problem is the variable density. Especially, when we consider this variation in filtered set of Navier-Stokes equations, three preliminary choice must be made [16]:

- The original set of unfiltered variables or equations.
- The filter.
- The filtered variables.

The first problem arises for huge numbers of formulations for the compressible Navier-Stokes equations exist rely on different choice of basic variables to describe the flow. Velocity is for example usually described with velocity and momentum. However, energy conservation can be expressed using two independent variables among: density, entropy, total energy, internal energy, enthalpy and so on. The difference of filter choice is already discussed in Section 2.1.4. The last point is actually the most difficult and important. If we consider the set of variables like $(\rho, \rho U, E)$, where E is the total energy, the direct application of filtering procedure from incompressible flows leads to the filtered variables $(\bar{\rho}, \bar{\rho U}, \bar{E})$. The term $\bar{\rho U}$ can be rewritten as:

$$\bar{\rho U} \equiv \bar{\rho} \hat{U}, \quad (2.47)$$

where $\hat{U} = \bar{\rho U} / \bar{\rho}$ is also filtered velocity. $\hat{\cdot}$ only represents a change of variable. The problem of basic variables choice arises because $\bar{\rho U}$, \bar{E} , and \bar{P} are nonlinear functions of other variables which can be decomposed. Thus different sub-grid terms will arise from the filtered equations as well as adding needs for specific Subgrid-modeling. Usually two systems are used to define the filtered problem:

- System I: It was suggested by Vreman [17], that with the basic filtered variables $\bar{\rho}, \bar{\rho} \hat{U}, \bar{E}$, the macropresure ξ and the macrotemperature θ can be defined as:

$$\xi_{maco} = \bar{P} + \frac{1}{3} \tau_{kk} = \bar{\rho} R \theta - \frac{3\gamma - 5}{6} \tau_{kk}, \quad (2.48)$$

$$\theta_{maco} = \hat{T} + \frac{\gamma(\gamma - 1) M^2 \tau_{kk}}{2} \bar{\rho}, \quad (2.49)$$

where M is Mach number. Since τ_{kk} is defined as $\tau_{kk} = \gamma M_{sgs}^2 \bar{P}$, and M_{sgs}^2 represents the sub-grid scale Mach number, which is certainly very small, some authors suggested that this term can be neglected.

- System II: Vreman [17] also imposed another system, in which the selected variables are $(\bar{\rho}, \hat{U}, \bar{E})$ The synthetic total energy is defined as:

$$\bar{E} = \frac{\bar{P}}{\gamma - 1} + \bar{\rho} \hat{U}^2 \quad (2.50)$$

and correspond to the computational total energy [16]. With this system no sub-grid contribution appears in the filtered equation of state.

2.1 LES Principle and Modeling

The choice of system for governing equations can change the closure problem by modifying the sub-grid terms. For application used in aeroacoustics and aero-optics system II is preferred as direct pressure and temperature can be derived. But system I is simpler for the energy equation, and is simpler implemented.

Using System II, and the similar method in derivation of incompressible filtered Navier-Stokes equations, the compressible Navier-Stokes equations (Eqs. (2.1), (2.2), (2.6)) can be filtered as:

$$\frac{\partial \bar{\rho}}{\partial t} + \frac{\partial(\bar{\rho}\widehat{U}_j)}{\partial x_j} = 0, \quad (2.51)$$

$$\frac{\partial \bar{\rho}\widehat{U}_j}{\partial t} + \frac{\partial(\bar{\rho}\widehat{U}_i\widehat{U}_j)}{\partial x_j} + \frac{\partial \bar{P}}{\partial x_i} - \frac{\partial \bar{\sigma}_{ij}}{\partial x_j} = \frac{\partial \bar{\rho}\tau_{ij}}{\partial x_j}, \quad (2.52)$$

$$\frac{\partial \bar{E}}{\partial t} + \frac{\partial((\bar{E} + \bar{P})\widehat{U}_j)}{\partial x_j} - \frac{\partial(\bar{\sigma}_{ij}\widehat{U}_j)}{\partial x_j} + \frac{\partial \bar{q}_i}{\partial x_j} = -\alpha - \beta - \pi + \varepsilon. \quad (2.53)$$

In the above Equations, the viscous stress tensor is defined as:

$$\bar{\sigma}_{ij} = \frac{\mu(\widehat{T})}{Re} \bar{S}_{ij}, \quad (2.54)$$

$$\bar{S}_{ij} = \frac{\partial \widehat{U}_i}{\partial x_j} + \frac{\partial \widehat{U}_j}{\partial x_i} - \frac{2}{3} \delta_{ij} \frac{\partial \widehat{U}_k}{\partial x_k}. \quad (2.55)$$

The dynamic viscosity $\mu(\widehat{T})$ can be derived from the Sutherland's law of air. While the filtered heat flux vector is defined as:

$$\bar{q}_j = \frac{\mu(\widehat{T})}{(\gamma - 1)Re Pr M^2} \frac{\partial \widehat{T}}{\partial x_j}, \quad (2.56)$$

where the Reynolds number Re and Prandtl number Pr are defined as:

$$Re = \frac{\rho U_j L}{\mu}, \quad Pr = \frac{C_p \mu}{\lambda}, \quad (2.57)$$

with L and λ represent characteristic length and thermal conductivity, respectively. The filtered temperature \widehat{T} comes from the state equation:

$$\widehat{T} = \gamma M^2 \frac{\bar{P}}{\bar{\rho}}. \quad (2.58)$$

The right-hand sides of Eqs. (2.52) and (2.53) contain sub-grid terms, that describe the effect of unresolved sub-grid scales. Especially the terms of filtered energy equation can be formulated as [18]:

$$\alpha = \widehat{U}_i \frac{\bar{\rho}\tau_{ij}}{x_j}, \quad (2.59)$$

$$\beta = \frac{\partial}{\partial x_j} \left[\left(\overline{P U_j} - \bar{P} \widehat{U}_j \right) / (\gamma - 1) \right], \quad (2.60)$$

$$\pi = P \frac{\overline{\partial U_j}}{\partial x_j} - \overline{P} \frac{\partial \widehat{U}_j}{\partial x_j}, \quad (2.61)$$

$$\varepsilon = \overline{\sigma_{ij} \frac{\partial U_i}{\partial x_j}} - \overline{\sigma}_{ij} \frac{\partial \widehat{U}_i}{\partial x_j}. \quad (2.62)$$

2.1.5 Subgrid-Scale Modeling

By LES various models are used in order to make the simulation more accurate and efficient in different geometries, flow and boundary conditions. In OpenFoam version 2.3.1, with the limiting of compressible LES modeling, there are totally five available SGS models, which will be discussed in following sections:

- Smagorinsky model
- One equation eddy model
- Homogeneous dynamic one equation eddy model
- Deardorff's Model
- Spalart-Allmaras Model

Algebraic Smagorinsky Model

Algebraic Smagorinsky model [9] is the basic and simplest LES model which can be produced with the following steps:

$$\tau_{ij} - \frac{1}{3} \delta_{ij} \tau_{kk} = -2\nu_{SGS} \overline{S}_{ij}, \quad (2.63)$$

$$\overline{S}_{ij} = \frac{1}{2} \left(\frac{\partial \overline{U}_i}{\partial x_j} + \frac{\partial \overline{U}_j}{\partial x_i} \right), \quad (2.64)$$

$$\nu_{SGS} = (C_s \Delta)^2 |\overline{S}|, \quad (2.65)$$

where the scalar $|\overline{S}|$ is the norm of $\frac{\partial \overline{U}_i}{\partial x_j} + \frac{\partial \overline{U}_j}{\partial x_i}$ in the boussinesq assumption. It can be presented as:

$$|\overline{S}| = \sqrt{2 \overline{S}_{ij} \overline{S}_{ij}}, \quad (2.66)$$

Parameter C_s , the Smagorinsky Constant varies with the isotropic turbulence decay in a range between 0.18 and 0.23. Δ is defined as the filter-width which takes the local grid size:

$$\Delta = (V_{cell})^{1/3}. \quad (2.67)$$

Close to the boundary condition, the SGS viscosity becomes huge for the large velocity gradient. While the SGS turbulent fluctuations near wall go to zero, so as the SGS viscosity. A Van driest damping function f_μ is thus desirable:

$$f_\mu = 1 - \exp(-x_2^+ / 26). \quad (2.68)$$

2.1 LES Principle and Modeling

In OpenFoam, the damping function, which is only needed by Smagorinsky Model, can be defined in the file "LESProperties". As a simple LES model, it has the lowest calculation cost of all the models. However, the main disadvantage of this model related to the variation of the defined Smagorinsky Constant C_s .

One Equation Eddy Model

Most one equation models are solving one equation for their own subgrid-scale quantity, which also based on the eddy-viscosity concept. One such typical scale like kinetic energy k_{SGS} , is defined as the subtracting of kinetic energy and the resolved kinetic energy:

$$k_{SGS} = \overline{K} - k_{RES} = \frac{1}{2}\tau_{ii}. \quad (2.69)$$

The transport equation for SGS turbulent energy can be derived by first subtracting the filtered equations of motion from their resolved parts to give a relation to the fluctuating component of velocity u' . And then multiply the result by the sub-grid velocity vector to give the equation, which was first formulated by Yoshizawa [19] as:

$$\frac{\partial k_{SGS}}{\partial t} + \frac{\partial}{\partial x_j}(\overline{u}_j k_{SGS}) = \frac{\partial}{\partial x_j} \left[(\nu + \nu_{SGS}) \frac{\partial k_{SGS}}{\partial x_j} \right] + 2\nu_{SGS} \overline{S}_{ij} \overline{S}_{ij} - \frac{1}{\Delta} C_e k_{SGS}^{3/2}, \quad (2.70)$$

$$\nu_{SGS} = C_k k_{SGS}^{1/2} \overline{\Delta}. \quad (2.71)$$

The production term $2\nu_{SGS} \overline{S}_{ij} \overline{S}_{ij}$ in this equation is equivalent to the SGS dissipation in the equation for the resolved turbulent kinetic energy k_{RES} . Default values of model coefficients C_e and C_k are given in OpenFoam as $C_e = 1.048$ and $C_k = 0.094$.

Actually under ideal equilibrium circumstances one equation models performs no better than the Smagorinsky model [13]. They all have the main deficiency of not addressing the discrepancy between the principal axes of the SGS stress and the rate of strain tensor, which is common to most eddy viscosity models. However, one equation model provides a more accurate time scale which is independent of velocity scale definition. This advantage glittered by modeling transitional flows or flows with large scale unsteadiness like Fureby [20] shows in channel flows.

Dynamic Models

As an improvement of Smagorinsky model, dynamic model was first formulated by Germano [21]. In his procedure, coefficients of SGS model should also be parts of calculation from the energy of smallest resolved scales. The sub-grid scale model in grid filter:

$$\tau_{ij}^r = \overline{U_i U_j} - \overline{U_i} \overline{U_j}. \quad (2.72)$$

Test filter with a width $\tilde{\Delta}$ larger than the original filter-width Δ (typically $\tilde{\Delta} = 2\Delta$). Apply it to the filtered N-S equation, the in "test filter" modeled sub-grid stress can be written as:

$$T_{ij}^r = \widetilde{\overline{U_i U_j}} - \widetilde{\overline{U_i}} \widetilde{\overline{U_j}}. \quad (2.73)$$

The resolved part of SGS stress at the test filter, known as the Leonard stress can be computed from LES fields with following relation:

$$L_{ij} = \widetilde{\overline{U_i U_j}} - \widetilde{\overline{U_i}} \widetilde{\overline{U_j}}, \quad (2.74)$$

with above definition:

$$L_{ij} = T_{ij}^r - \widetilde{\tau_{ij}^r}. \quad (2.75)$$

Eq. (2.75), known as Germano identity, forms the basis of dynamic models. This identity was used by Piomelli [22] to derive model coefficients as shown in the following steps. First parameters α_{ij} and β_{ij} were used to model generalized eddy-viscosity of subgrid and sub-test-grid in the deviatoric part.

$$\tau_{ij}^r = -2C_e \alpha_{ij}, T_{ij}^r = -2C_e \beta_{ij}. \quad (2.76)$$

Five independent equations are thus used to derive the single coefficient, which caused over-determining problem. Based on the least-squares method Lilly [23] attempted to remedy this problem with the help of minimizing an error, which was produced by two approximation Eqs. (2.75) and (2.76). The error can be formed as:

$$E_{ij} = L_{ij}^d - T_{ij}^r - \widetilde{\tau_{ij}^r} = L_{ij}^d + 2C_e M_{ij}, \quad (2.77)$$

where $M_{ij} = \beta_{ij} - \widetilde{\alpha_{ij}}$. The constant C_s is assumed to be smooth on the scale and can be derived from the the filtering operation with the least-squares minimization:

$$\frac{\partial \langle E_{ij} E_{ij} \rangle}{\partial C_e} = 2 \left\langle E_{ij} \frac{\partial E_{ij}}{\partial C_e} \right\rangle = 0, \quad (2.78)$$

Combine Eqs. (2.77) and (2.78):

$$\langle (L_{ij}^d + 2C_e M_{ij}) M_{ij} \rangle = 0, \quad (2.79)$$

where C_e can be finally derived as:

$$C_e = -\frac{1}{2} \frac{\langle L_{ij}^d M_{ij} \rangle}{\langle M_{ij} M_{ij} \rangle}. \quad (2.80)$$

These model coefficients vary with time and space, and invalidate the original value, which was assumed constant at first and then removed from the filtering operation. Some stability problems are caused by the removing process. Integral formulation of the identity Eq. (2.74) was introduced by Ghosal [24] to remove the inconsistency. The total viscosity (molecular and SGS) must larger as zero for his improvement. The solution of this integral through the use of least-square method leads to a constrained optimization problem, which is known as the dynamic localization model. This model is reported to produce good results with the cost of calculation time.

As the advantage of dynamic model, many problem with traditional "static" methods, especially the sub-grid scale modeling were successfully resolved. It adjusts the free shear and channel flows by lowing the coefficient in areas of high shear and near the walls, where

van Driest damping was used by other methods. In laminar part will the eddy viscosity automatically be changed to zero.

As disadvantage, in order to avoid excessive fluctuations in the model coefficients, additional averaging for all the homogeneous directions, along streamlines or in local regions of the flow should also be iterated. Even the local average requires local homogeneous flow or large averaging volume to smooth the model coefficients. Also, de Villar [13] reported that some negative dissipation randomly occur in this procedure unless the scheme is somehow artificially bounded. Piomelli [25] and Germano [21] interpret this as energy transport from unresolved to resolved scale. However, it can also violate the conservation of energy conservation and lead to unphysical results if unchecked.

Deardorff's Model

A major weakness for all the eddy-viscosity based models above is the assumption of isotropy in the unresolved scales. This is true for only a large subset of flows and filters, which actually unusual in practice. If the mesh spacing is too large, the unresolved motion may be anisotropic. Even the smallest scales could not satisfy the isotropy assumption by solid boundaries. In these cases, anisotropic grids will resolve isotropic eddies differently with their own orientation. Further refinement of the mesh can reduce this problem, but a better result can only be achieved if abandon the assumptions of isotropy.

By ignoring isotropy assumptions, the equation that is similar to the one-equation turbulent energy model (Eq. (2.70)) can be formulated with the complete SGS stress tensor τ_{ij} (in OpenFoam defined in the file "B"). The first model was derived by Deardorff [26] and then developed by Fureby et al. [27] as the following:

$$\frac{\partial \tau_{ij}}{\partial t} + \frac{\partial}{\partial x_i} (\tau_{ij} \bar{U}_i) = 2\nu_{SGS} \bar{S}_{ij} \bar{S}_{ij} + \underbrace{\frac{\partial}{\partial x_i} \left[(\nu + \nu_{SGS}) \frac{\partial \tau_{ij}}{\partial x_j} \right]}_{\mathbf{M}} + \underbrace{\frac{2}{5} k_{SGS} \bar{S}_{ij} - \frac{1}{\Delta} c_M k_{SGS}^{1/2} \tau_{ij}}_{\mathbf{\Pi}} - \underbrace{\frac{2}{3\Delta} C_e k_{SGS}^{1/2}}_{\mathbf{E}}, \quad (2.81)$$

where

$$\nu_{SGS} = c_k \Delta K^{1/2}, \quad (2.82)$$

$$c_k = 0.07, c_M = 4.15, c_e = 1.05. \quad (2.83)$$

In right hand-side of Eq. (2.81): \mathbf{M} is an approximation for the triple correlation tensor, $\mathbf{\Pi}$ models the pressure velocity-gradient and the dissipation tensor is approximated by the \mathbf{E} term, which is assumed to be isotropic. Fureby et al. [27] also proved that the differential stress model produces backscatter similar to the linear combination model with enough fine mesh, but with the inter-scale transfer limited by the transported SGS energy. With decreasing spatial resolution, the modeled energy transfer behaves more like an eddy viscosity model.

Since the stress tensor τ by Eq. (2.81) is symmetric ($\tau_{ij} = \tau_{ji}$), only 6 tensor components are needed to be defined in file "B" for the simulation. But it is still more expensive as the

algebraic or one equation models. However, it costs only a small part of the overall calculation in consideration of the resolved pressure momentum calculation. The major advantage of this model is proven to be his good performing in big range of flow conditions [27].

Spalart-Allmaras Model

The Spalart-Allmaras Model [28] is a one equation model which has been derived largely with the help of empiricism. It gives the proper behavior in 2-D mixing layers, wakes, and flat-plate boundary layers. A field equation for the working variable ν^* can be formulated as:

$$\begin{aligned} \frac{\partial \nu^*}{\partial t} + U_j \frac{\partial \nu^*}{\partial x_j} = & C_{b1}(1 - f_{t2})\bar{S}\nu^* - \left[C_{w1}f_w - \frac{C_{b1}}{\kappa_0^2}f_{t2} \right] \left(\frac{\nu^*}{d} \right)^2 \\ & + \frac{1}{\sigma} \left[\frac{\partial}{\partial x_j} \left((\nu + \nu^*) \frac{\partial \nu^*}{\partial x_j} \right) + C_{b2} \frac{\partial \nu^*}{\partial x_i} \frac{\partial \nu^*}{\partial x_i} \right], \end{aligned} \quad (2.84)$$

the left-hand side represents advection along the particle path while the terms on the right-hand side represent diffusion, anti-diffusion, production, destruction and a trip term, respectively [29]. Boundary condition for the model are specified as: $\nu^* = 0$ on solid walls; $\nu^* = \nu_\infty^* < 0.1\nu_\infty$ along inlet ($u \cdot n < 0$) and $\nu^* = 0.1\nu_\infty$ as interior values along outlet. This results in the low value of $\mu_{SGS\infty} = 2.79 \times 10^{-7}\mu_\infty$ in the free stream. An initial condition can be taken as $\nu^* = \nu_\infty^*$ everywhere. Some coefficients above are defined using the following functions:

$$\chi = \frac{\nu^*}{\nu} \quad (2.85)$$

$$f_{v1} = \frac{\chi^3}{\chi^3 + c_{v1}^3} \quad (2.86)$$

$$f_{v2} = \left(1 + \frac{\chi}{c_{v2}} \right)^{-3} \quad (2.87)$$

$$f_{v3} = \frac{(1 + \chi f_{v1})(1 - f_{v2})}{\chi} \quad (2.88)$$

$$S^* = |S_{ij}|f_{v3} + \frac{\nu^*}{\kappa_0^2 d^2} f_{v2} \quad (2.89)$$

where d is the distance to the closest wall. Since all these functions are also well calculated as $\chi \rightarrow 0$, one can replace χ with $\max(\chi, 0.001)$ to prevent division by zero in Eq. (2.88). The destruction term is constructed with the aid of the following functions:

$$r = \frac{\nu^*}{S^* \kappa_0^2 d^2}, \quad (2.90)$$

$$g = r + c_{w2}(r^6 - r), \quad (2.91)$$

$$f_w = g \left(\frac{1 + c_{w3}^6}{g^6 + c_{w3}^6} \right)^{1/6}. \quad (2.92)$$

2.1 LES Principle and Modeling

Function f_{t2} is used as a damper into the production and destruction terms in order to make $\nu^* = 0$ still a stable solution. It is formulated as:

$$f_{t2} = c_{t3} \exp(-c_{t4}\chi^2). \quad (2.93)$$

The strip term $f_{t1}\delta_U U^2$ allows one to specify explicitly the boundary transition locations. The function f_{t1} is given by:

$$f_{t1} = c_{t1}g_t \exp\left(-c_{t2}\frac{\omega_t^2}{\Delta U^2}(d^2 + g_t^2)d_t^2\right), \quad (2.94)$$

where d_t is the distance to the nearest trip point, ω_t is the vorticity at the wall at the trip point, δ_U is the norm of the difference between the velocity at the trip point and the field point under consideration, and $g_t = \min(0.1, \delta_U/\omega_t\delta_w)$ where δ_w is the spacing along wall at the trip point. With this help, the eddy viscosity is given by:

$$\nu_{SGS} = \nu^* f_{v1}. \quad (2.95)$$

As f_w stays almost constant for large g number, r can be replaced by $\min(r, 2)$ in order to prevent overflow in Eq. (2.92), all the constants are defined as follows:

$$\begin{aligned} c_{b1} &= 0.1355, c_{b2} = 0.622, \\ \sigma &= 2/3, \kappa_0 = 0.41, \\ c_{w1} &= \frac{c_{b1}}{\kappa^2} + \frac{1+c_{b2}}{\sigma}, c_{w2} = 0.3, c_{w3} = 2, \\ c_{v1} &= 7.1, c_{v2} = 5, \\ c_{t1} &= 1, c_{t2} = 2, c_{t3} = 1.2, c_{t4} = 0.5. \end{aligned}$$

In the original version S^* could also be negative with the definition, which could then disturb the value of r and result in stalled convergence. In the above improved version, functions f_{v3} has been introduced an definition of f_{v2} has been changed, ensuring S^* to be non-negative. It can however be zero, so that a protection against division by zero when calculation r is needed.

2.1.6 Wall Treatment

Compared with the overall flow fields, the viscous effect become significant in the thin near-wall sublayer. Since all terms like production, dissipation, kinetic energy, Reynolds stress achieve their peak values when $y^+ < 20^1$. In LES, generally there are two ways to deal with the boundary condition problem [12]:

- LES-NWR (near wall resolution) \rightarrow All parts in computational domain are resolved.

The grid spacing and filter width should be the same order as viscous length scale δ_v which defined as:

$$\delta_v \equiv \nu \sqrt{\frac{\rho}{\tau_w}} = \frac{\nu}{u_\tau}, \quad (2.96)$$

¹ y^+ is wall coordinate, that is defined as $y^+ = \frac{yu_\tau}{\nu}$ with y the distance to wall and u_τ the friction velocity

where τ_w and u_τ are named wall shear stress and friction velocity, respectively. Therefore it is not suitable for high-Reynolds-number flows, for a high grid spacing demand and simulation cost.

- LES-NWM (near wall modeling) \rightarrow The near wall region be modeled.

The near wall progress is not resolved but modeled. It is usually used by high-Reynolds-number flow, where the SGS model coefficient at boundary shows only low accuracy. Transforms like Van Driest damper (Eq. (2.68)) turn out to be suitable. Different kinds of wall functions can also be chose (even in OpenFoam) to model the fluid profile in the boundary nearest grid point. Dynamic model can do even better by iterating those coefficients within the simulation progress.

In this thesis, the Re number will respect to the velocity amplitude, which is very moderate. Nevertheless, it can be observed that turbulence structures develop due to the pulsating nature of the flow. Thus, for a more accuracy simulation first way (LES-NWR) is therefore preferred. Accordingly, the grid spacing at the walls must be fine enough.

2.2 Basis Of Acoustics

2.2.1 Acoustic Equations

With the assumption of zero mean flow velocity, i.e. $U_0 = 0$, acoustic quantities P , ρ and U can be separated into mean part (with index₀) and fluctuation part (with superscript ') as:

$$\begin{aligned} P &= P_0 + P', \\ \rho &= \rho_0 + \rho', \\ U &= U_0 + U'. \end{aligned} \tag{2.97}$$

Consider now the perfect gas. Set Eq. (2.97) in the continuity (2.1) and momentum transport equations (2.2), and neglect the products of small quantities:

$$\frac{\partial \rho'}{\partial t} + \rho \nabla \cdot U' = 0, \tag{2.98}$$

$$\rho \frac{\partial U'}{\partial t} + \nabla P' = 0. \tag{2.99}$$

Use the definition of sound speed c and Taylor expansion of P around P_0 with respect to ρ at constant entropy s yields:

$$P = P_0 + \left(\frac{\partial P_0}{\partial \rho} \right)_s \rho' + \mathcal{O}(\rho'^2). \tag{2.100}$$

$$c^2 \equiv \left(\frac{\partial P_0}{\partial \rho} \right)_s, \tag{2.101}$$

The first-order approximation for pressure fluctuation can be formed as:

$$P' = c^2 \rho', \tag{2.102}$$

By inserting Eq. (2.98) into Eq. (2.102), it can be rewritten as:

$$\frac{1}{c^2} \frac{\partial P'}{\partial t} + \rho \nabla \cdot U' = 0. \tag{2.103}$$

The time differentiating of Eq. (2.103) subtract the divergence of Eq. (2.99) yields the wave equation respect to the pressure disturbance:

$$\frac{\partial^2 P'}{\partial t^2} - c^2 \nabla^2 P' = 0. \tag{2.104}$$

In one dimension, wave equation can be factorized as:

$$\left(\frac{\partial}{\partial t} + c \frac{\partial}{\partial x} \right) \left(\frac{\partial}{\partial t} - c \frac{\partial}{\partial x} \right) P' = 0. \tag{2.105}$$

The general solution of the equation above can be written as:

$$\frac{P'(x, t)}{\rho c} = f(x - ct) + g(x + ct), \quad (2.106)$$

where f and g describes the wave moving in positive and negative direction. In the one dimensional cases, the so-called Riemann invariants f , g as the solution of Eq. (2.99), can be expressed in terms of P' and U' :

$$f = \frac{1}{2} \left(\frac{P'}{\rho_0 c} + U' \right), \quad (2.107)$$

$$g = \frac{1}{2} \left(\frac{P'}{\rho_0 c} - U' \right). \quad (2.108)$$

2.2.2 Helmholtz Resonator

The Helmholtz Resonator consists of a cavity room and backing volume with the connection of a orifice (see Fig. 3.2). Due to variable geometry, sound pressure level (SPL), the flow in and out of resonator could be laminar or turbulent. A derivation of the flow motion in Helmholtz Resonator is listed in App. A.1, with a final result of the motion in the neck of the resonator can be approximately described by Keller and Zauner [3] as:

$$(1 + \mathcal{T})l_m \rho \frac{\partial^2 U}{\partial t^2} - \frac{A_m \rho c^2}{V} U = -\zeta \rho \frac{\partial U}{\partial t} |U| - \mathcal{T} l_m \rho \omega \frac{\partial U}{\partial t} - \frac{\partial P}{\partial t}, \quad (2.109)$$

with \mathcal{T} a coefficient, l_m the orifice length, A_m the orifice area and ζ the loss coefficient (see App. A.1)

As the acoustic resonator is always described with respect to frequency, parameter of velocity and pressure can therefore be formulated in the form of $U = U^* e^{i\omega t}$, $P = P^* e^{i\omega t}$. Eq. (2.109) can be rewritten as:

$$\underbrace{(1 + \mathcal{T})l_m \rho \omega i U^*}_{\mathbf{A}} + \underbrace{\mathcal{T} \rho l_m \omega U^*}_{\mathbf{B1}} + \underbrace{\epsilon_{nl} \mathcal{T} \rho d_m \omega U^*}_{\mathbf{B2}} - \underbrace{\frac{A \rho c^2}{V \omega} i U^*}_{\mathbf{C}} = -P^*, \quad (2.110)$$

where the loss factor ϵ_{nl} accounting for the nonlinear losses [30] can be expressed as

$$\zeta \rho U^{*2} \approx \epsilon_{nl} \mathcal{T} \rho d_m \omega U^*, \quad (2.111)$$

This factor depends both on the resonator geometry and especially the SPL [6].

In Eq. (2.110) the first term A on left hand-side accounts for air mass within the neck region, while the second term represents the linear dissipation loss B1 due to friction of fluid oscillation near wall and the nonlinear losses B2 due to vortex shedding. The third term C reflected effect of compression. The right hand-side shows an acceleration caused by pressure difference [6]. An very important criterion: the eigenfrequency of resonator can be calculated from Eq. (2.110) as:

$$\omega_{eig} = c \sqrt{\frac{A_m}{V(1 + \mathcal{T}l_m)}}, \quad (2.112)$$

Finally, the a normalized impedance can be expressed as:

$$Z(\omega) = \frac{P^*}{U^*} = \rho \frac{A_{ca}}{A_m} \left(1 + \frac{\gamma - 1}{\sqrt{\text{Pr}}}\right) \left(1 + \epsilon_{nl} + \frac{l_m}{d_m}\right) \sqrt{2\nu_{air}\omega} + i \frac{A_{ca}}{A_m} \left[l_m \rho \omega \left(1 + \mathcal{T} - \frac{A_m \rho c^2}{V\omega}\right)\right], \quad (2.113)$$

where the real part and imaginary part are defined as resistance \mathcal{Re} and reactance \mathcal{Im} :

$$\mathcal{Re}(Z) = \rho \frac{A_{ca}}{A_m} \left(1 + \frac{\gamma - 1}{\sqrt{\text{Pr}}}\right) \left(1 + \epsilon_{nl} + \frac{l_m}{d_m}\right) \sqrt{2\nu_{air}\omega}, \quad (2.114)$$

$$\mathcal{Im}(Z) = \frac{A_{ca}}{A_m} \left[l_m \rho \omega \left(1 + \mathcal{T} - \frac{A_m \rho c^2}{V\omega}\right)\right]. \quad (2.115)$$

By studying Eqs. (2.110) and (2.113), it can be observed that the resistance part is constructed by pressure term and losses term, where nonlinearity may exists, and the reactance includes mass term and compression. Another important factor: the reflection coefficient $\mathcal{R}_f(\omega)$ also relates to the normalized impedance Z , which can be defined as:

$$\mathcal{R}_f(\omega) = \frac{g^*}{f^*} = \frac{Z - \rho c}{Z + \rho c}, \quad (2.116)$$

with \star indicates the Fourier transferred quantity.

3 Numerical Setup

In this chapter, the basic solver settings used for the presented simulations are presented. Simulation algorithms and addition smooth methods are first introduced in Sec. 3.1. On the one hand, the target of algorithm choice is to make the whole simulation process stable, and on the other hand, the chosen setup must ensure an accurate reproduction of the physical processes. Geometries and meshes are presented in Sec. 3.2. All cases are simulated with 3D structured meshes. On one side, different geometries and meshes will help to ensure the conclusions that achieved are general, on the other side, different geometries and grid sizes can also be treated as alternative parameters in the analysis of final results.

3.1 PIMPLE with NSCBC

All simulations presented this thesis are performed with PIMPLE algorithm in OpenFoam, which combines the processes of SIMPLE and PISO, whose flow chart is depicted in Fig. 3.1. In the inner PISO loop, a combination of pressure equation and velocity correction is calculated, while the energy equation is solved in the outer SIMPLE loops. This process suits especially to in high frequency fluctuating fluid fields and unstable fluid simulations. Compared with the pure PISO algorithm, calculation for the inner time steps stays more stable by the PIMPLE process, since the energy equation will not be calculated. And the danger of instable break up can thus be enormously reduced.

In OpenFoam, the parameters of PIMPLE algorithm are defined in the file "fvsolution", a sample code line can be defined as follows:

$$\begin{aligned} nOuterCorrector & 20; \\ nCorrectors & 3; \end{aligned}$$

It means in each time step the outer loop will be computed till converged or 20 times if not converged, and for each outer loop the pressure equation with velocity correction iterates 3 times.

In this thesis, PIMPLE algorithms that coupled with Navier-Stokes Characteristic Boundary Condition (NSCBC) from the paper of Poinot and Lele [31] will be used. With this boundary condition, it is possible to insert a acoustic wave "f", while ensuring low acoustic reflections for the leaving wave "g".

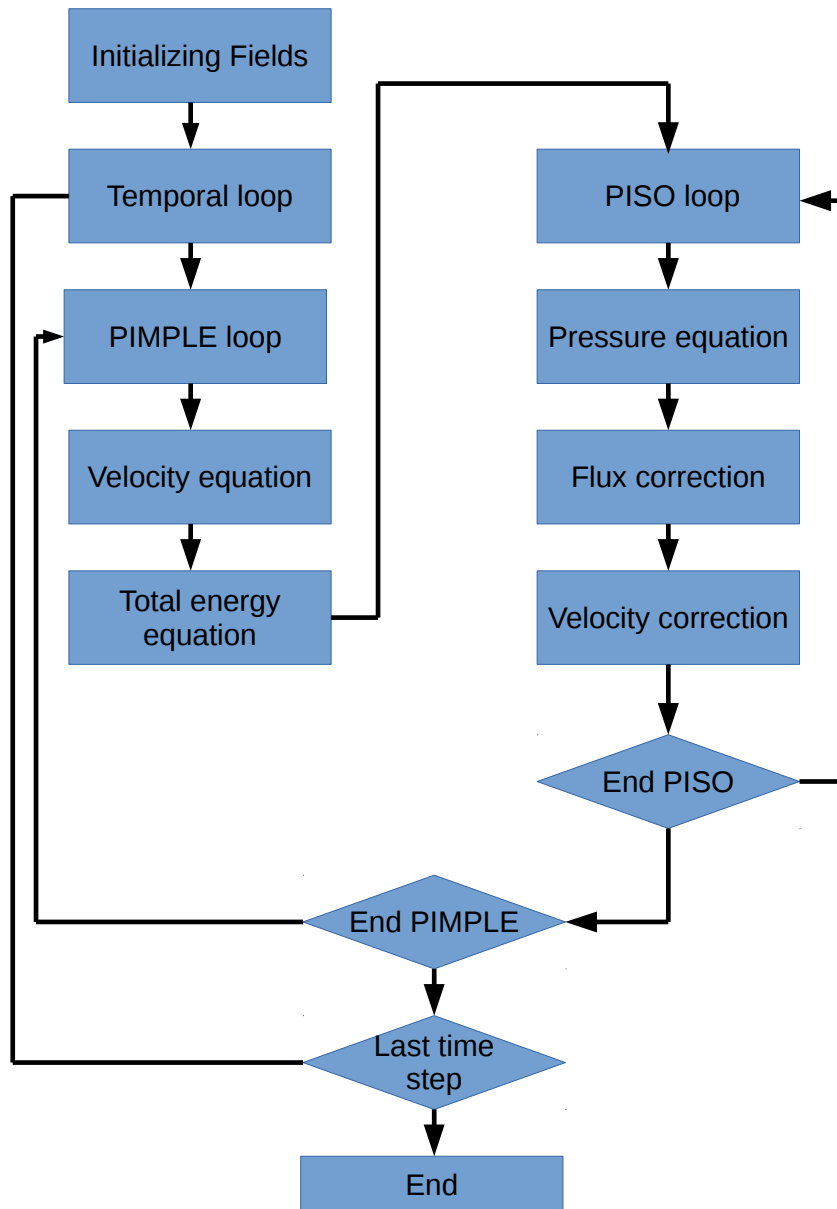


Figure 3.1: PIMPLE Algorithms

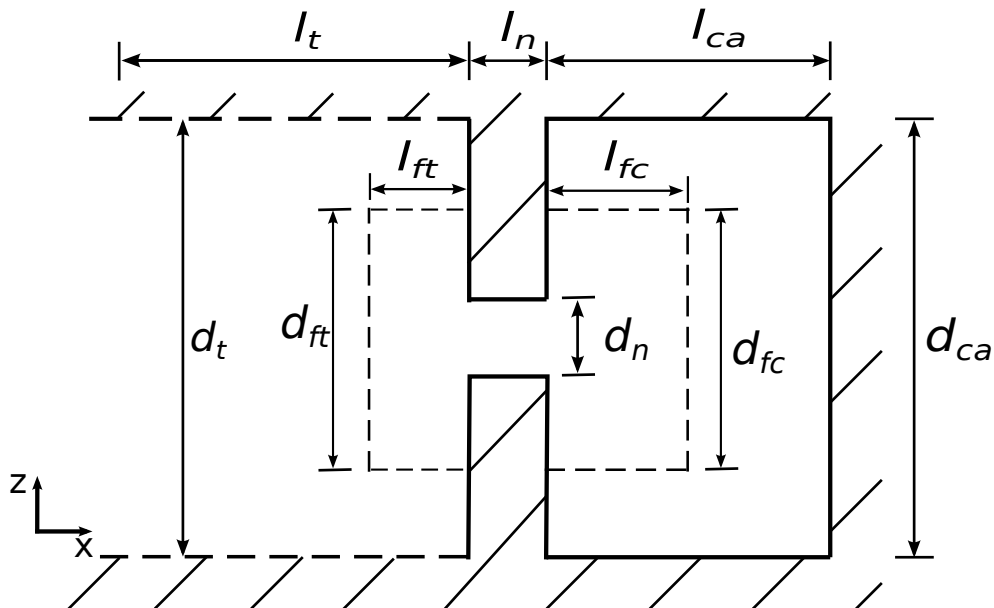


Figure 3.2: Helmholtz Resonator geometry in the simulations

3.2 Test Cases

In order to ensure mesh independence, different meshes are built up for the simulation, which will be introduced in this section. Moreover two different geometries are used to enable more general conclusions in the end. With actually the same construction (as in Fig. 2.3 presented), Helmholtz Resonators from Hersh and Förner vary only in geometry sizes. Hersh's geometry will be investigated in special detail, because more series of experimental data are given in his paper [1]. In the mean while, Förner's geometry is used also with measurement [4] to prove, that the conclusion from Hersh's simulation is a general one.

3.2.1 Hersh's Geometry

A typical Helmholtz Resonator is structured as Fig. 3.2. In the simulated cases, it consists of three parts: backing volume, the neck and impedance tube outside the resonator. Whole structure is generated as a 3-D axis symmetric cylinder, whose geometrical size is tabulated in Table 3.1.

Geometry [mm]	Outside Tube		Orifice		Cavity	
	length l_t	diameter d_t	length l_n	diameter d_n	length l_{ca}	diameter d_{ca}
Hersh	100	50.8	1.59	6.35	25.4	50.8
Förner	50	50	4	4.2	20	50

Table 3.1: Helmholtz Resonator geometries from Hersh et al. [1] and Förner et al. [4].

In part close to the neck, where the fluid separates and then develops into turbulence,

meshes need to be refined properly. However, over-sized refinement region will enormously enhance the total computation cost without obviously improving the result since only little computational region is filled with vorticity structures. As shown in Fig. 3.2, also the sizes of refinement region differ with the resonator geometry, which can be formulated in Table 3.2.

Geometry [mm]	Tube Refinement		Cavity Refinement	
	length l_{ft}	diameter d_{ft}	length l_{fc}	diameter d_{fc}
Hersh	10	12	10	12
Förner	15	12	15	12

Table 3.2: Refinement of Hersh and Förner’s geometry.

Mesh Variation

In this section the mesh setting of each geometry is presented. From the direction of positive symmetric axis (+X direction), the mesh can be divided in four parts like in Fig. 3.3a. Block I and II are inside resonator orifice diameter, while sizes of Block III and IV can be referred to the geometry defined in Sec. 3.2.1. This block separation validate both in Hersh’s and Förner’s geometry.

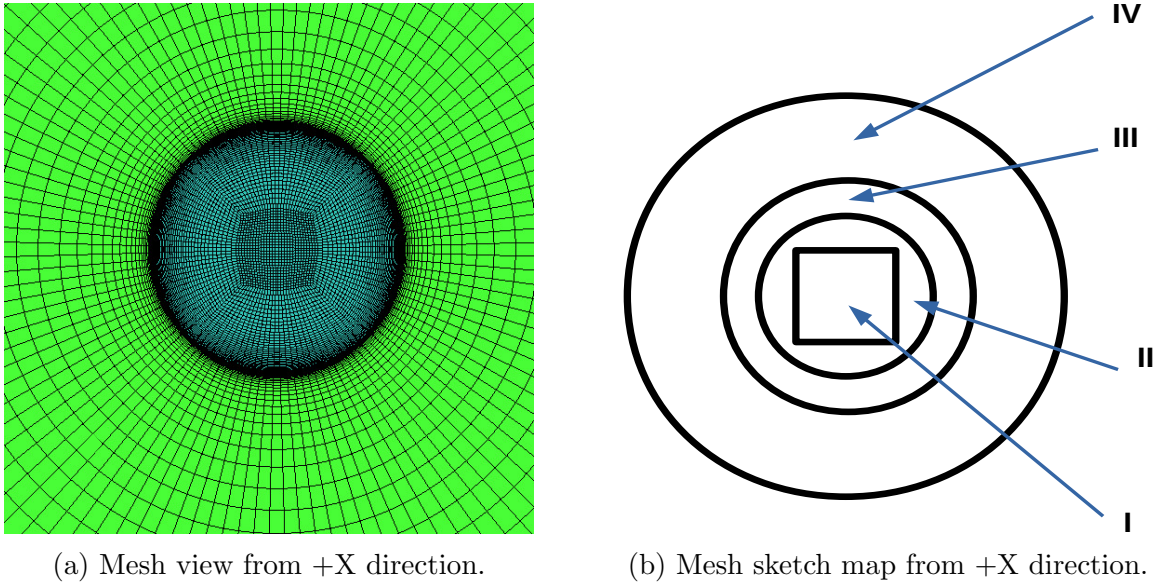


Figure 3.3: Mesh structure from +X direction with notation of blocks, I: H grid region inside orifice; II: O grid region inside orifice; III: refinement region of O grid; IV: coarse grid region of O grid.

Three meshes with different grid size (coarse[HC], middle[HM] and fine[HF]) are utilized in the simulation of Hersh’s resonator. On the one hand, different grid scale means also different computation node numbers, which results in different simulation quality and

computational cost. In simulation of turbulence, the grid size plays even more important role, as the ratio between grid scales and turbulence length scales can influence the simulation result significantly. It can be evaluated through spatial TKE spectrum and two-points correlation in Secs. 4.2.2 and 4.2.4. On the other hand, the suitable grid scale also varies with different SGS-Models, compare the final results of different models in all of these three meshes, the relationship between grid scale and SGS-models can also be evaluated as will be discussed in Sec. 4.2.6. Last but not least, the results from different grids are also to be compared with the Hersh's experimental data, so that the grid influence can be quantitatively appraised. Table 3.3 presents the detailed definition of these three grid sizes in Hersh's geometry.

Outline and directions	node numbers of meshes		
	coarse (HC)	middle (HM)	fine (HF)
circumferential	64	80	120
orifice region in X	48	60	75
tube refinement in X	32	40	50
cavity refinement in X	32	40	50
tube in X	24	30	38
cavity in X	12	15	19
block II in radial	24	30	38
block III in radial	12	15	19
block IV in radial	12	12	19
space ratio	1.4	1.3	1.3
wall resolution	0.02[mm]	0.02[mm]	0.02[mm]

Table 3.3: Mesh data for Hersh's resonator geometry.

Compared with normal mesh setting, an extremely fine grid separation is made in circumferential direction and especially for the fine mesh. That is because of a utilization of azimuthal velocity for the estimation of fluid dynamic properties (see Sec. 4.2.1). And a refinement in that direction can help to enhance the analysis accuracy.

Boundary Conditions

As presented in Fig. 3.4, the whole boundary is divided into three part: inlet I, tube II and wall III. For more general case inlet covers the boundary where the acoustic signal is imposed, and the tube hold the mean fluid velocity, which flows along the z direction queer to resonator orifice. In thesis, this velocity is set to be 0 to simplify the situation, therefore no mean velocity is implemented in this simulation, but in the future the similar simulation with mean flow still make sense. The wall boundary included all the solidity boundaries in a real geometry. Thus, general parameters for all available models can be defined in Tab. 3.4. By the definition of inlet velocity "U", an acoustic signal file "inletf.txt" will be included, which is generated through program Matlab following the definition of NSCBC 3.1. In dynamic models a very small velocity field instead of value zero is needed

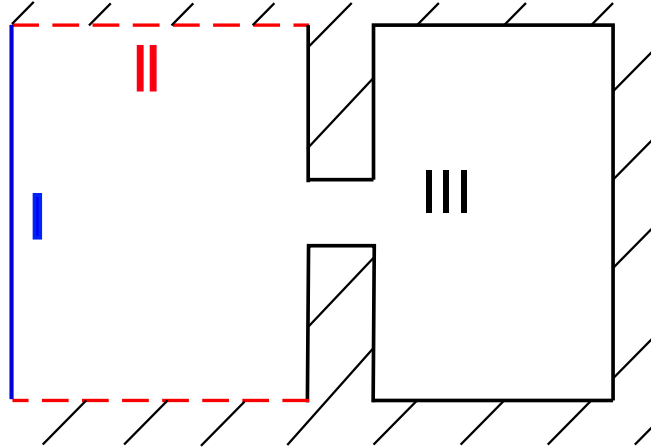


Figure 3.4: Helmholtz Resonator with boundary: I–Inlet; II–Tube; III–Wall.

to initialize the SGS coefficient calculation. Boundary condition "muSgs" and "alphaSgs" should also be defined for all SGS models besides laminar one. They describe the characters of SGS thermal diffusivity and dynamic viscosity, respectively.

Parameter	Inlet	Tube	Wall	Initial field
U [m/s]	NSCBC	symmetry	fixed velocity field (0 0 0)	fixed velocity field (0 0 0)
p [Pa]	NSCBC	symmetry	Zero gradient	fixed value 10^6
T [K]	fixed value 293	symmetry	Zero gradient	fixed value 293
alphaSgs [kg/(m · s)]	Zero gradient	Zero gradient	Zero gradient	fixed value 0
muSgs [kg/(m · s)]	Zero gradient	Zero gradient	Zero gradient	fixed value 0

Table 3.4: Initial and general boundary conditions of all SGS Models.

Parameter	Inlet	Tube	Wall	Initial field
k [m ² /s ²]	Zerogradient	symmetry	Zerogradient	fixed value 10^{-8}
nuTilda [m ² /s]	fixed value 4.44×10^{-5}	Zerogradient	fixed value 0	fixed value 4.44×10^{-5}
B [m ² /s ²]	Zerogradient	symmetry	Zerogradient	fixed field (0 0 0 0 0 0)

Table 3.5: Initial and boundary conditions of special SGS Models parameters.

However, in some SGS models special parameters can be added, which are defined in Tab. 3.5. "k" is actual SGS kinetic energy k_{SGS} in Sec. 2.1.5. It is required in one Equation eddy model and homogeneous dynamic one Equation eddy model. Considering the boundary effect, a very small initial value k_{SGS} instead of 0 is desired to ease the danger of simulation breaking up. "nuTilda" is needed in SpalartAllamra model as ν^* in Sec. 2.1.5. Referring Gomez [32], the value of "nuTilda" can be defined as three times that of air kinetic viscosity. At last, parameter "B", the complete SGS stress tensor is only needed by Deardorff's model. For a symmetric third-order matrix, only 6 items should be included by the definition.

3.2.2 Förner's Geometry

No big diversity between the geometrical structure of Förner's and Hersh's geometry can be noticed, except the ratio of resonator orifice diameter to length value. That ratio is 1.05 by Förner's geometry and 4 by Hersh's. The resonator size changes as Tab. 3.1 and Tab. 3.2 present. As the result, mesh data also varies as presented in Tab. 3.6. This mesh is referred to as FM in the following discussions. With the geometrical diversity between these two cases, a difference in eigenfrequency should also be concerned as about 380Hz in Förner's geometry and about 560Hz in all Hersh's geometries.

Outline	node number in Förner's Mesh(FM)
circumferential direction	80
orifice region in X direction	75
tube refinement in X direction	70
cavity refinement in X direction	70
tube in X direction	25
cavity in X direction	10
block II in radial direction	15
block III in radial direction	18
block IV in radial direction	25
space ratio	1.1
wall resolution	0.01[mm]

Table 3.6: Mesh data for Förner's resonator geometry FM.

4 Simulation Results

In this chapter, the simulation results are discussed with the purpose to evaluate the performance of different LES Subgrid-Scale models. This discussion consists of three parts as considering of acoustic, fluid dynamic and other criteria. In first part, impedance and reflection coefficient are considered to evaluate acoustic properties. While in fluid dynamic part, spatial and temporal correlations and turbulent kinetic energy spectra are used. All other criteria like Q-criterion and E/k criterion are described and utilized in the third part.

4.1 SGS Modeling Influence Of Acoustic Behavior

Acoustic analysis belongs to the most important contents in this work, since the mean purpose of Helmholtz Resonator is to dampen the SPL and dissipate the acoustic energy. According to the theoretical discussion in Sec. 2.2.2, the impedance Z and reflection coefficient \mathcal{R}_f may act as useful criteria in the analysis of acoustic behaviors in Helmholtz Resonator. In this section, most of the discussion is based on the impedance, while the reflection coefficient is used in concerning about the SPL differences for his connection to energy.

The presented impedance are normalized (see Eq. (2.113)) in this work to allow a better comparison between different geometries. The real part of impedance is also called resistance " $\mathcal{Re}(Z)$ " and the imaginary part is called reactance " $\mathcal{Im}(Z)$ " (see Eqs. (2.114) (2.115)).

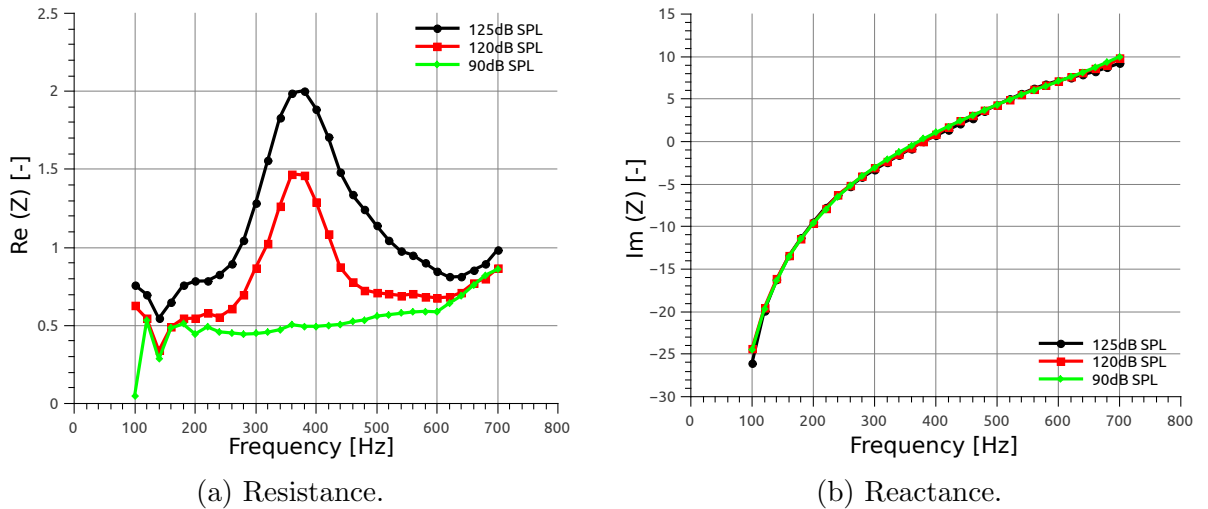


Figure 4.1: Impedance: Nonlinear behavior in the resistance and linear behavior in the reactance by geometry FM.

This strategy is widely used in analysis of acoustic properties in Helmholtz Resonator (see [1, 33]). The resistance part and reactance part of impedance are therefore separated, since the former one may presents a non-linearity behavior with the influence of SPL and geometry, which is described in model of Eq. (2.111) with the nonlinear loss factor ϵ_{nl} in the resistance. However, with the including of the mass term and compression term, the reactance part always shows a very good linearity with different SPLs. A typical impedance series of Helmholtz Resonator with respect to frequency, where non-linearity in resistance and linearity in reactance with the changed SPLs is presented in Fig. 4.1. It can be seen that the resistance changes with the SPL and behaves nonlinear, while the reactance does not.

Most helpful details can also be presented through the loss factor and the nonlinearity caused by it. Since it is proven to be the most sensible to SPL difference as well as the utilized SGS models. So that the difference between variety of SGS models can be figured out more directly.

Compared with the impedance, the gain of reflection coefficient represents the absorption of acoustic energy more directly. According to Eq. (2.116), it is defined as the ratio of Fourier transformed reflection wave g to the Fourier transformed initial wave f . Therefore, larger gain of this coefficient means the the resonator damps inefficiently, as less acoustic energy are in resonator absorbed. While a smaller number of it implies more acoustic energy is damped through resonator.

Figure 4.2 shows the reflection coefficient numbers of a certain SPL with respect to the frequency. As expected close to eigenfrequency, the coefficient decreases to its smallest value, where the turbulence is proved to be most strongly excited. However, since the value at each frequency also changes with different SPLs, which will be further discussed in Sec. 4.1.3, linear behavior of Resistance according to different SPLs is not possible. And that is also the basic reason of Resistance nonlinearity.

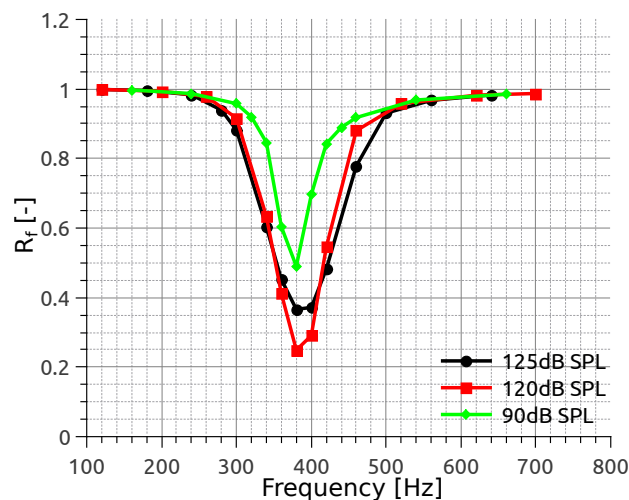


Figure 4.2: Typical gain of the reflection coefficient with respect to frequency and SPL with FM geometry.

4.1.1 Correction SPL to AMP Transformation

To make a meaningful comparison with the experimental data, the velocity conditions should be set to match that of Hersh's geometry [1] in the simulation. However, the SPL value is measured at a certain position l_t away from the neck (see Fig. 3.2) in experiment. While in the simulation, this must be defined for the inlet boundary to match the experiment. Therefore, a correction for the signal definition is needed. According to Förner et al. [5], a transform of the acoustic signal definition from SPL to pressure amplitude (AMP) of the wave A_f with $f = A_f \exp(i\omega t)$ can be used to set the acoustic input wave correctly. As the characteristic wave can be expressed as:

$$\frac{P'(l_t)}{\rho_0 c_0} = [1 + \mathcal{R}_f \exp(-i\omega 2l_t/c_0)]f(l_t). \quad (4.1)$$

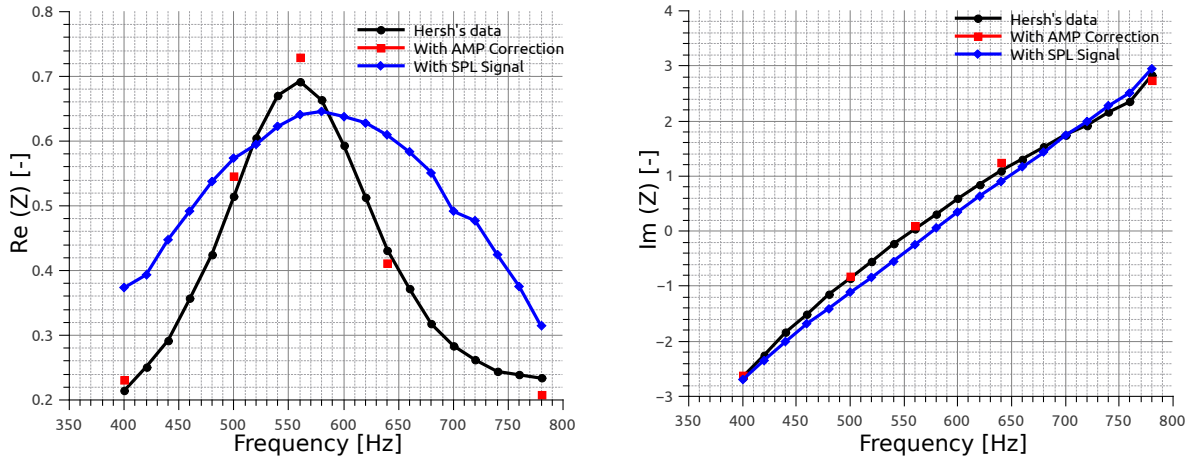
The reflection coefficient \mathcal{R}_f must be calculated with a iterative process if it is not known before. But in order to reduce the simulation cost, values are directly taken from Hersh's paper [1]. Thus, the relationship between the measured SPL of Hersh and the needed wave pressure amplitude in simulation can be formulated as [4]:

$$A_f = 10^{L_p/20} \frac{\sqrt{2}P_{ref}}{|1 + \mathcal{R}_f \exp(-i\omega 2l_t/c_0)|\rho_0 c_0}. \quad (4.2)$$

where the SPL value L_p is defined as:

$$L_p = 20 \log_{10} \left(\frac{P'}{P_{ref}} \right) \quad (4.3)$$

Figure 4.3 makes the above discussed topic visible. Especially from the resistance part, simulation results from through SPL numbers defined acoustic signals present huge inaccuracy if compared with the experimental data. In the meanwhile, those through AMP



(a) Resistance by AMP correction.

(b) Reactance by AMP correction.

Figure 4.3: Impedance comparison between the simulation results of SPL and corrected AMP defined signals.

defined acoustic signals shows relative reasonable results compared with the experimental data. Thus, the comparison between simulated and experimental results seem to be more reliable if a AMP correction is acted. Therefore when the impedance curve of a special SPL is simulated, a series of corresponding AMP values at different frequencies should be computed at first for the setting of the NSCBC. In the following sections, all signals are defined according to corrected AMP acoustic waves.

4.1.2 Impact of SGS models

With the previous preparations, the influence on the impedance and reflection coefficients caused by SGS model differences will be discussed in this section as one of the most important part of this work. A comparable laminar model without SGS modeling and all available compressible LES SGS models that listed in Sec. 2.1.5 except Deardorff's model will be utilized in this comparison. Deardorff's model is not discussed here due to its unstable behavior for the setup consideration. Simulation of Deardorff's model works out only with quite small frequency, where the non-linearity performance can not be notice in resistance even with different SPLs, which certainly make no sense for the evaluation. The reason of this unstable behavior is still unclear. As authors assumption, at the time point of reflected wave passing by the orifice region, an interference caused by initial acoustic wave and the reflected wave may excited some unknown and unstable factor within the complete SGS stress tensor τ_{ij} , which dominants the iteration of Deardorff's model. And that instability can finally break the modeled NS-equation at the very same time point. However, no other condition or setting changes except reducing frequency range can help vanishing that error, so that this model has to be left for future discussion in other topics.

The comparison between experimental data and simulated results of geometry "FH" is presented in Fig. 4.4. The subfigures (a) and (b) show out result of the 130dB case, (c) and (d) the result for a SPL of 140dB case. In general, the largest differences between experimental and simulated results (Smagorinsky model as example) exist mostly in resistance part by eigenfrequency range. The difference of measured and simulated reactance is quite ignorable. Only in the resistance part, some larger variety presents by eigenfrequency range (here about 600Hz) and high frequency ranges (here above 700Hz). Since all models present with relatively similar behavior, only one curve of Smagorinsky model is printed and the others are shown only with selected points. Even though these minimum differences in the figure, Spalart Allmaras model will always be the one, that for most selected frequencies closest to the experimental data, especially in higher frequency ranges. This is reasonable, since besides the Deardorff's model, Spalart Allmaras model is left to be the only one that considers the complete SGS stress tensor. More empirical coefficients are in that model also imposed to ensure his accuracy with different geometries. And in each flow condition a special defined trip term ν^* can make a better adjustment for his environment. However, even the simplest laminar model without any consideration of LES SGS also prints a reasonable and very similar data series, which is unexpected. It means by case of no mean flow, the simulation of by acoustics generated turbulence is relatively independent from the turbulent model whatever be use. A complex SGS modeling utilization for acoustic analysis is only needed by very precise simulations, otherwise laminar model is enough to fulfill the

4.1 SGS Modeling Influence Of Acoustic Behavior

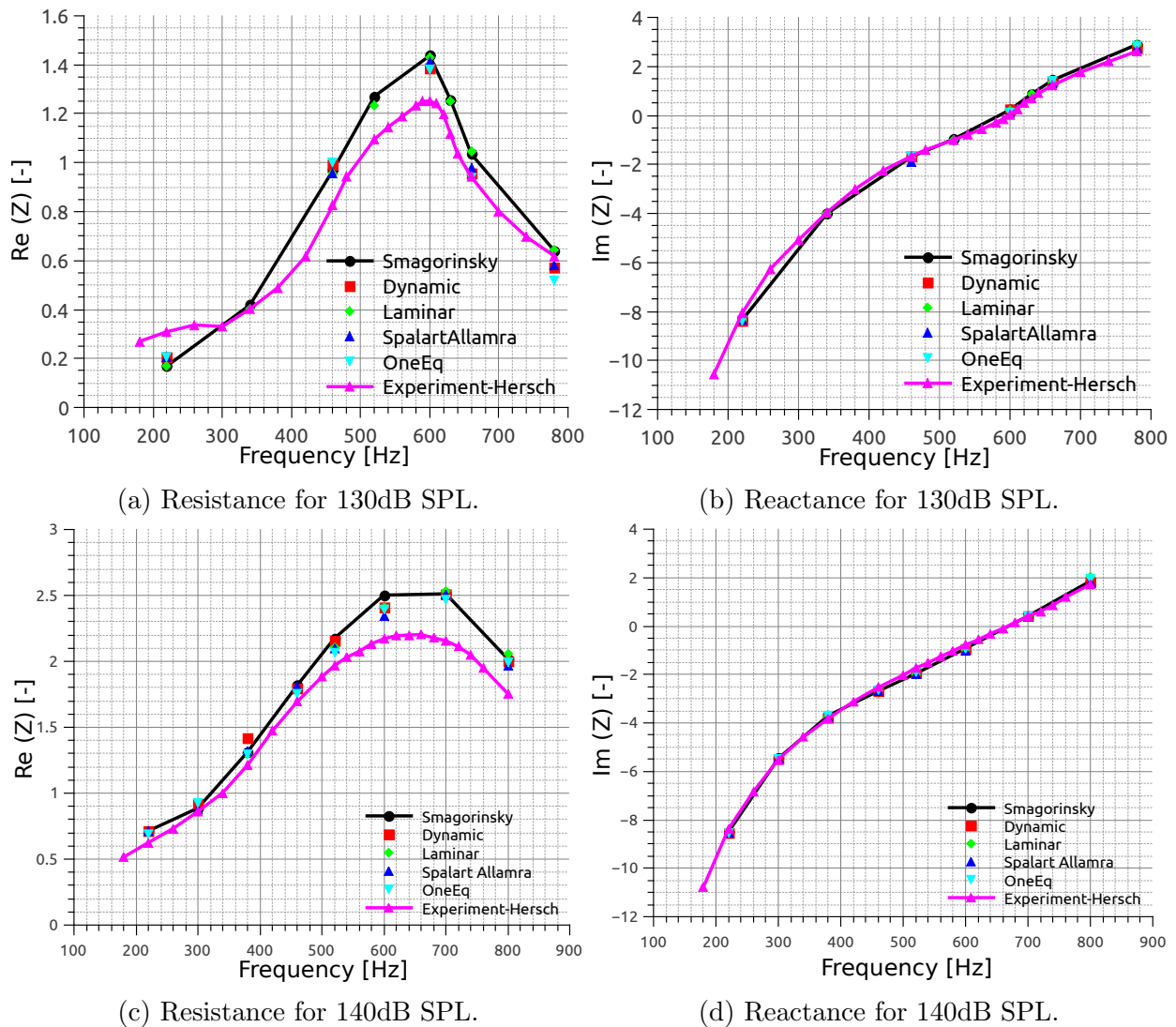


Figure 4.4: Impedance with difference SGS models of SPL 130dB and 140dB in Hersh's geometry "FH".

estimation. However, it is not discussed in this work whether laminar modeling still works in the case of larger mean flow, where the mean flow can also generate turbulence itself.

Similar comparison can also be made for Förner's geometry "FM" as presented in Fig. 4.5. An Obvious distinction from the one of Hersh's is that a larger difference between the experimental and simulated results exists in relatively linear range (below 300Hz and over 500Hz). However, as shown in Hersh's case, different SGS models still result in only a small impedance variety. For all comparable simulated frequencies and SPLs, different SGS models present almost the same values. Therefore the conclusion can be made, as the LES SGS models variety impacts non-linearity in impedance resistance in a Helmholtz Resonator only with quite small range by means of CFD.

Besides the comparison of impedance, influence of different SGS models in reflection coefficient can be found in Fig. 4.6. Only the comparison of high SPLs in each geometry

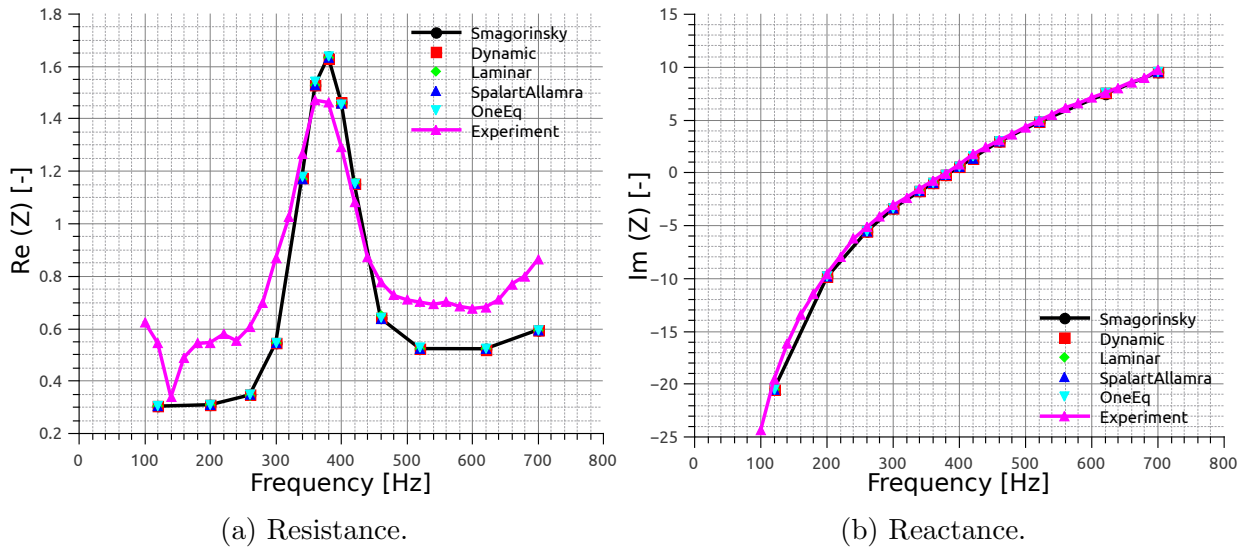


Figure 4.5: Impedance with different SGS models by SPL 120dB in Förner's geometry "FM".

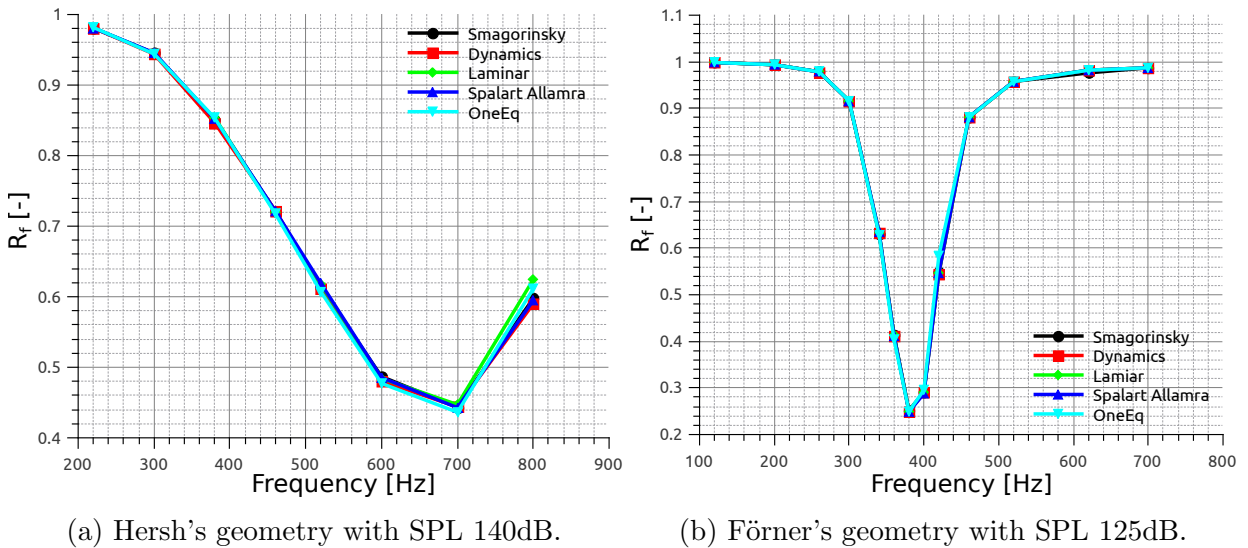


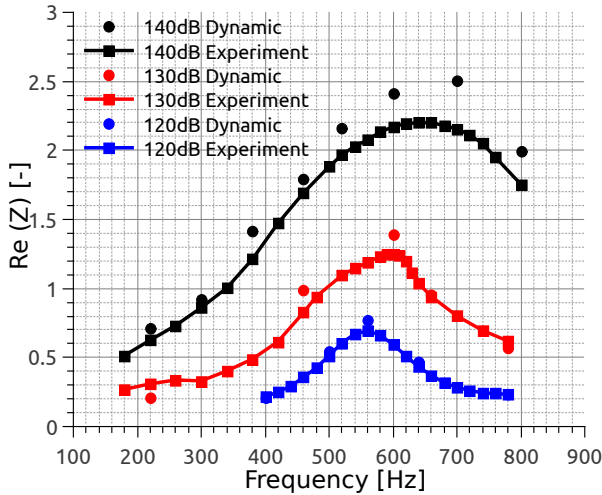
Figure 4.6: Reflection coefficient for different SGS models with meshes "HF" and "FM".

is listed here, since the nonlinearity, according to previous discussion, is extremely strong by those SPLs, and different SGS models varies more. As expected, in general only minor differences can be observed in coefficient gain for different SGS Models. Relatively, some differences by high frequency range in Hersh's geometry is more obvious, which can also be reflected from impedance discussions.

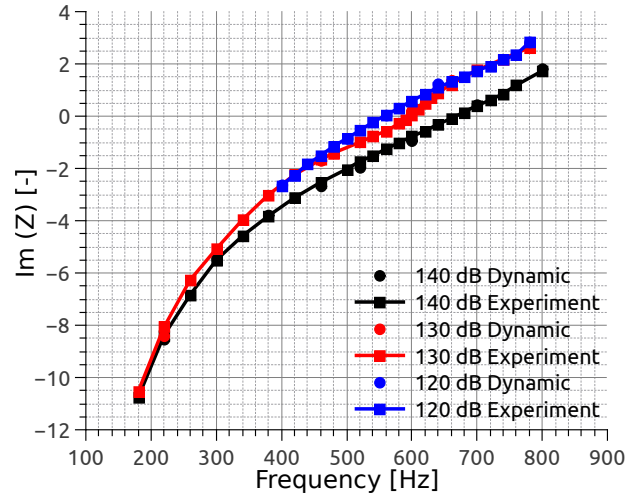
4.1.3 Nonlinear Resistance With Respect To SPL

Our discussion on LES SGS models depends fully on the assumption, that the turbulence close to neck is already generated by acoustics. However, the flow does not separate by lower SPLs, so that the turbulence close to neck will not be generated. As the result, the nonlinearity behavior in resistance will also disappear. In this section, the above resistance nonlinearity with its respect to SPL will be quantified. As comparison, experimental data and simulated results (here the dynamic model) are selected. Both the results from Hersh's geometry "FH" and Förner's one "FM" are presented in Fig. 4.7.

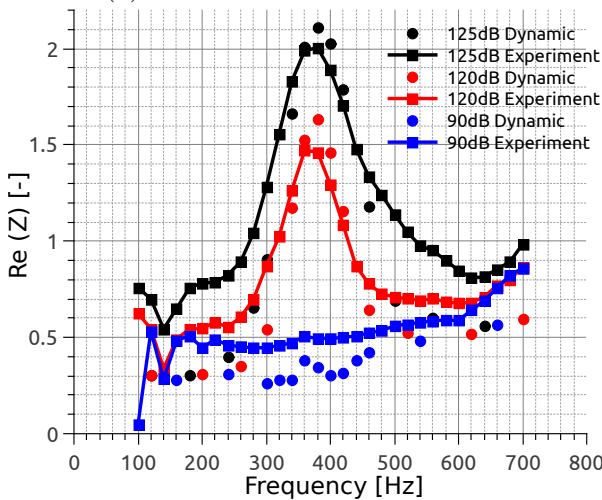
Consider first Hersh's geometry in Fig. 4.7. The strongest nonlinear behavior occurs in the frequency space between 560Hz and 640Hz. As the eigenfrequency of Hersh's geometry is around 580Hz, where also the highest nonlinear behavior occurs as expected. Considering the resistance, the nonlinear behavior of resistance becomes stronger with the growth of



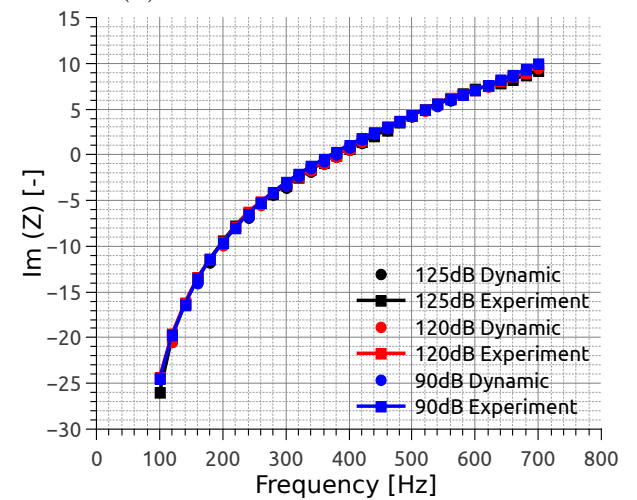
(a) Resistance of Hersh's "FH".



(b) Reactance of Hersh's "FH".



(c) Resistance of Förner's "FM".



(d) Reactance of Förner's "FM".

Figure 4.7: Impedance with different SPLs in Hersh and Förner's geometries.

SPL, and the difference between experimental and simulated results also enlarges. Results of simulation in this geometry is more reliable for lower SPL with a better conformity with the experimental data if compared with the higher SPLs. However, the variety of SPLs has not that strong impact on the reactance, where both of the three utilized SPL curves behaves linearly with the similar form and value. No remarkable difference between experiment and simulation because of SPL changes can be noticed if regarding only the reactance part.

When the geometry of Förner is considered, the former conclusion about reactance turns to be strictly true. Even the difference for change in SPLs is not noticeable. But as discussed in previous section, relatively less similarity is expressed in the resistance comparison between experiment and simulation in Förner's geometry. Consider the curves, where nonlinear behavior is triggered (with SPL of 120dB and of SPL 125dB), close to the eigenfrequency, the resistance obtain from simulation is always higher than that from experiment. Only away from the eigenfrequency, this prediction of the numerics vanishes and the experiment measures higher resistance values. However, for SPL 90 dB, where flow rarely separates, a linear relation can be followed in both experimental and simulated curves, with the simulated value always smaller than the experimental ones.

Also for very high SPLs, the effective length decrease, which drive the eigenfrequency shift to higher frequency range. This can be seen in Hersh's geometry, where the neck length is very small, such that a shift in the end correction has a huge impact. For Förner's geometry, the neck is larger and not so high SPLs are investigated. Therefore no shift in eigenfrequency is visible.

As conclusion, simulated resistance values around the eigenfrequency are always larger as the experimental data. But the comparison in relative linear parts depends on the accuracy of SPL to AMP correction and geometry. No useful messages about SPL varieties can be figured out from reactance curves.

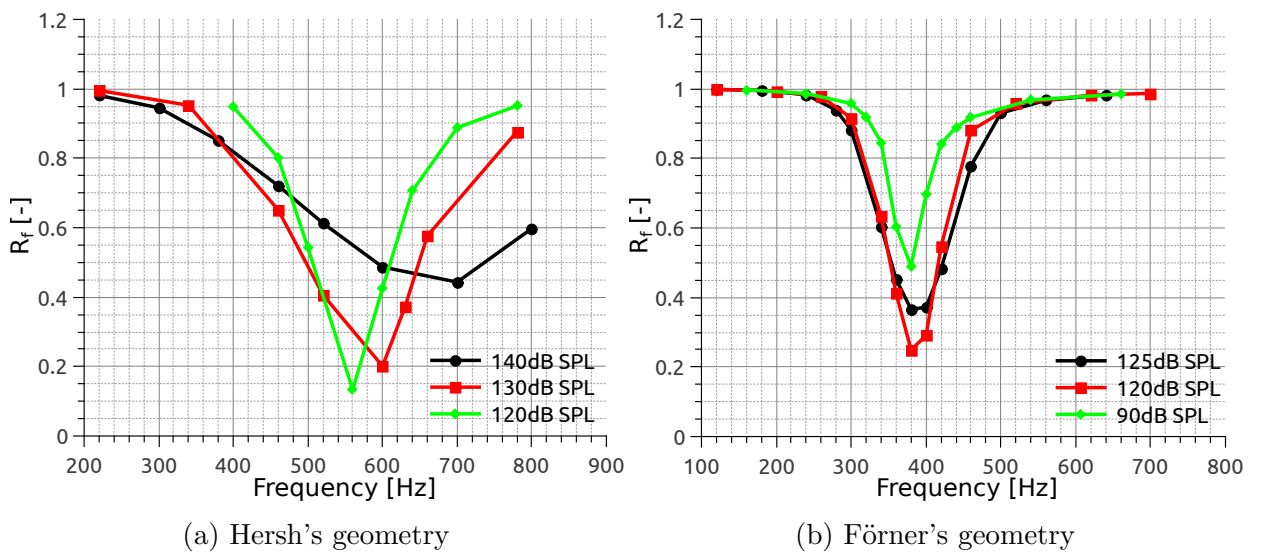


Figure 4.8: Reflection coefficient \mathcal{R}_f by dynamic model simulation with variety of SPL in mesh "HF" and "FM".

As introduced in Sec. 4.1, nonlinearity of resistance can be traced back to the change of resonator reflection coefficient " \mathcal{R}_f " with SPL differences as shown in Fig. 4.8. By Förner's geometry, we find the value of reflection coefficients are usually larger by simulation of linear case (90 dB SPL) than those by simulation of nonlinear case (like 120 dB SPL). Since the generated turbulent structure will help to absorb acoustic energy to make the reflection coefficients even smaller. However, by further increasing of SPL, only the growth of absorbed absolute quantity of acoustic energy can be achieved, while the relative proportion of absorbed parts to the whole acoustic energy parts decreases. This conclusion can be summarized through the raising of reflection coefficients again with further growth of SPL both in Förner's geometry (from 120dB to 125db) and Hersh's geometry (from 120dB to 140dB). Thus, with further growth of SPL, there should be a critical SPL value, beyond which even the absolute quantity of absorbed acoustic energy will not change. This assumption can be proven through turbulent kinetic energy spectra analysis in Sec. 4.2.5. However, it is true only when the overdamped frequency for all SPLs are very close (can be regarded as eigenfrequency) as the example in Förner's geometry. A resonator is overdamped when the normalized resistance $\mathcal{R}_e > 1$, where the gain of the reflection coefficient increases strongly with the increasing of the SPL. However, if the overdamped frequency also varies strongly (can not be treated as eigenfrequency) with the change of SPLs, as Hersh's geometry, this conclusion is not quite sure. As example we can consider the frequency of 700Hz in Hersh's geometry, since \mathcal{R}_f is smaller for SPL 140dB case than for 130dB and 120dB ones, even by higher SPL, resonator can absorb both large proportion and absolute quantity of acoustic energy.

4.2 Influence of The SGS Modeling on Turbulent Kinetic Energy Spectra and Correlation

In the previous section of the acoustic analysis, only minor differences resulting from of SGS model utilization can be observed. Therefore, we concentrate more on the part of pure CFD analysis to evaluate the turbulence behavior. According to Davidson's investigation [8], correlations and energy spectrum belong to the most popular and effective methods to have a deep look into the turbulence. Because of that, correlations, including spatial two-points and temporal auto-correlation, as well as turbulent energy spectra in frequency and wave number space, will be the focus point in the following discussion of SGS modeling comparison.

4.2.1 Azimuthal Velocity

Generally in full developed turbulent system, the selected velocity direction will not play a very significant roll, since the turbulence is homogeneous. However, in our system, where the original mean velocity is zero and the turbulence is generated by acoustic signals, the velocity fluctuation includes therefore not only the part caused by turbulence but also a part due to the acoustic signal fluctuation if consider only directions in axial and radial directions. The complete velocity fluctuation can be expressed with both acoustic component U'_{acou} and pure turbulent component U'_{turb} as:

$$U' = U'_{acou} + U'_{turb}. \quad (4.4)$$

Thus, estimation criteria like correlation and turbulent kinetic energy, which base on velocity fluctuation, will lose their accuracy or shows very unreasonable characters, if the acoustic velocity fluctuation is still included in the analysis. To deal with this problem, Zhang and Bodony has provided a clever strategy in their paper [7]. They transformed their velocity in a cylindrical coordinate system and considered only the azimuthal velocity that is vertical to the acoustic signal transfer direction instead of the axial and radial direction.

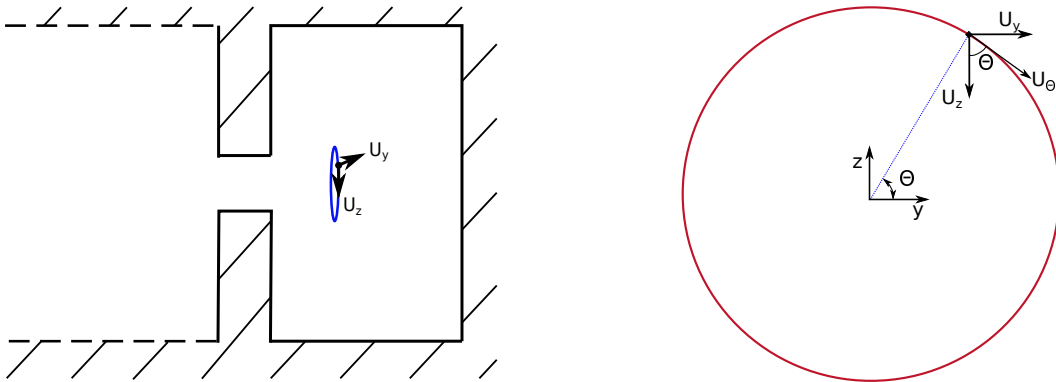


Figure 4.9: Measurement of the azimuthal velocity in resonator.

4.2 Influence of The SGS Modeling on Turbulent Kinetic Energy Spectra and Correlation

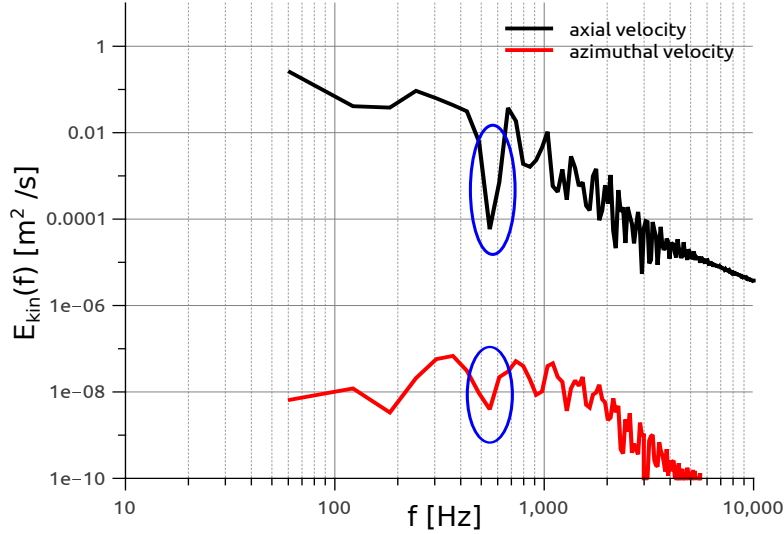


Figure 4.10: TKE spectra with azimuthal and axial velocity.

In our cases this strategy will also be used as illustrated in Fig. 4.9. Since the acoustics is by definition irrotational, it does not influence the azimuthal velocity component in our axis-symmetric cases. With its tight relationship to the location coordinates, the azimuthal velocities must be calculated in each investigated point. Azimuthal velocity transform from Cartesian coordinate can be expressed as:

$$U_{\theta} = U_y \cdot \sin \theta + U_z \cdot \cos \theta = U_y \cdot \frac{Z}{\sqrt{Y^2 + Z^2}} + U_z \cdot \frac{Y}{\sqrt{Y^2 + Z^2}}, \quad (4.5)$$

where U_y and U_z donate velocity in Y and Z-direction, Y, Z the monitored locations. Through azimuthal velocity transformation, acoustic factors, especially the resonance near eigenfrequency range can be sharply reduced. A comparison of TKE spectra (see Sec. 4.2.4) based on both axial velocity and cylindrical azimuthal velocity is presented in Fig. 4.10.

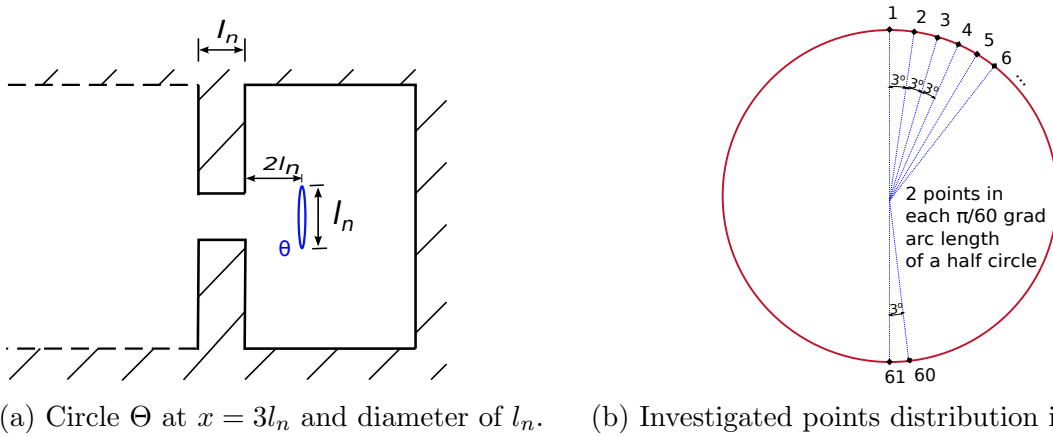
The acoustic signal in Fig. 4.10 is generated with a frequency of 400Hz, which is close to the eigenfrequency of geometry "FM" according to Sec. 4.1. From the comparison, an obvious peak shaped form can be found in the curve of axial velocity around the resonance frequency of 400Hz, which shows a strong relationship with acoustic characters. In the meantime, azimuthal velocity curve present a good reduction of acoustic effect in vanishing the spike shaped form around the same region. The TKE spectra values also varies strongly between that of axial velocity and azimuthal velocity. On the one hand, an acoustic longitudinal wave excited fluctuation mainly in its propagating axial direction, on the other hand, by reducing acoustic fluctuation part, some energy that shows acoustic perturbation are therefore ignored. In the following sections only the estimation based on azimuthal velocity is used to reduce the acoustic influence as much as possible.

4.2.2 Correlations

From the discussion of Sec. 2.1.2, two varieties of correlation can help to investigate the turbulence simulation depending separately on spatial (grid size) and temporal (time step) criteria. Their setting and analysis are discussed in this section.

Two-points correlation

According to the discussion in Sec. 4.2.1, the azimuthal velocity is utilized to study the pure turbulent behavior in the situation of this work. As a result, the two-points correlation should also present the turbulence characters in circumferential direction, which can also be regarded as homogeneous turbulent direction. Therefore, the probe-points must be located along a circle in the Y-Z plane.



(a) Circle Θ at $x = 3l_n$ and diameter of l_n . (b) Investigated points distribution in circle Θ .

Figure 4.11: Setting of investigated points and circle.

Figure 4.11 defines the circle and points that fulfill former discussed conditions. The concerned circle Θ with radius of half orifice length is located at Y-Z plane with distance of twice orifice length to the end of resonator neck like Fig. 4.11a shows. 61 investigated points are distributed along the half circumference of circle Θ , which means one point in each $\Psi = 3^\circ$ arc length as shown in Fig. 4.11b. Thus, the minimum resolved unit is determined by the resonator geometry characteristic length l_{ca} as $\pi R\Psi/l_{ca}$, while the maximum resolved unit is determined by the minimum mesh grid size Δ_{cell} as $\pi R\Psi/\Delta_{cell}$. In the analysis for only two-points correlation of different SGS models, other conditions are set as presented in Tab. 4.1 presents:

Conditions	signal SPL	signal frequency	mesh
Value	120dB	600Hz	HF

Table 4.1: Condition of two-points correlation analysis.

With the former settings, the normalized two-points correlation (see Eq. (4.8)) for different SGS models according to azimuthal velocity is calculated and presented in Fig. 4.12.

4.2 Influence of The SGS Modeling on Turbulent Kinetic Energy Spectra and Correlation

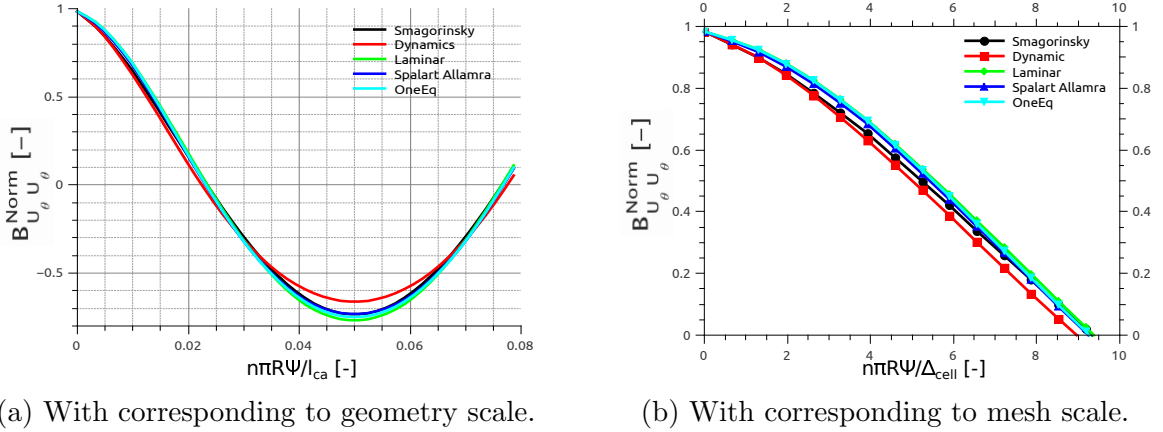


Figure 4.12: Two-points correlation with different models.

The left figure shows the normalized two-points correlation that corresponds to geometry resonator scale. It presents a high fluctuation amplitude (between ± 0.7) if compared with the auto-correlation (between ± 0.2) in later section. It actually means the spatial resolution is not as good as the temporal one, so that the relationship between two selected spatial points can express more unstable factors as the two from temporal points do. However, if Fig. 4.12b on the right hand-side is considered, the spatial resolution still satisfies the need to a accurate simulation. Since before the normalized two-points correlation falls to 0.1, which is often characterized as a turbulent length scale limitation (see [8]), there are already 8 to 10 grids to cover the largest turbulent scale. These cell numbers varies only a little within different SGS numbers, which means each model can provide a suitable spatial resolving in the simulated case. Combining also the curves from Fig. 4.12a, the dynamic model performs a little better for its relative smoother fluctuation than the other SGS model. However, it is actually not so important in the discussing.

Auto-correlation

Similar settings can also be utilized to investigate the behavior of the velocity auto-correlation. Different from the probe-points series in two-points correlation, only one probe-point is needed for the auto-correlation. The Auto-correlation can be computed through the velocities of each two different time steps in that point. As the two-points correlation presents main characters in spatial mesh settings, auto-correlations depends more on time step setting. Original time steps of simulations in this thesis are initialed to be 6×10^{-7} s and the maximum time step is limited as 1×10^{-6} s. During the simulation process, a proper time step between the initial value and the maximum value is chosen by the solver automatically as to improve the simulation efficiency, while a certain maximal CFL-number is chosen. The same condition setting as two-points correlation analysis is read from Tab. 4.1. The single monitored point is chosen to be *point 1* in Fig. 4.11b. Using the mathematical methods from Sec. 2.1.2, curves running of normalized auto-correlation at *point 1* for different SGS models are computed as presented Fig. 4.13.

Different from two-points correlation in Fig. 4.12, more accurate curves is presented

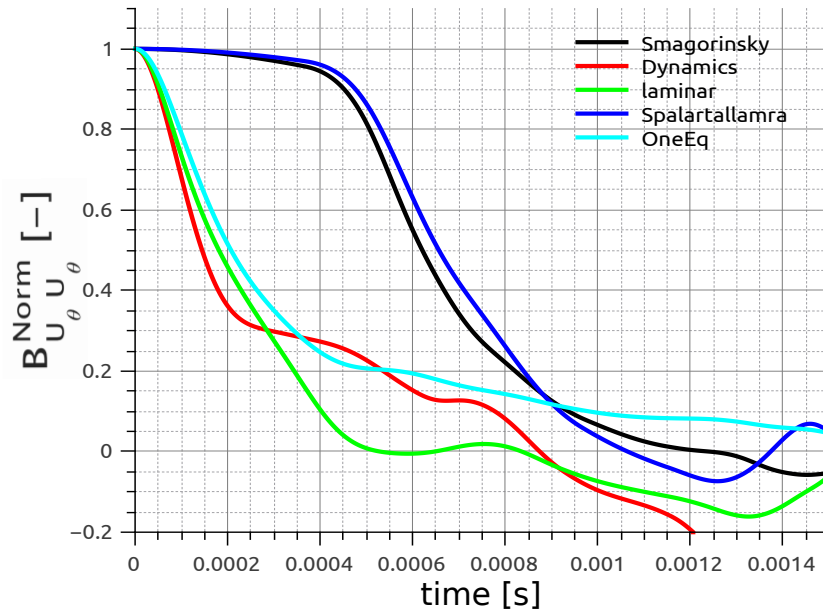


Figure 4.13: Auto-correlation with different models

in Fig. 4.13, as chronological velocity series including thousands of samplings in time is generated automatically while the spatial local points have to be defined by hand. For most curves, that corresponds to different SGS models, correlation fluctuations are between -0.2 and 0.2 for relatively bigger time steps, which also presents a better homogeneous character in temporal series.

Comparing all the SGS models, Smagorinsky model and Spalart Allmaras model shows the best behavior in this chronological valuating, since these two curve last the longest with a correlation value of about 1, and the time integral scales also presents larger number of $6.23 \times 10^{-4}s$ and $6.49 \times 10^{-4}s$, respectively. The value of other three models are around $2.5 \times 10^{-4}s$. It means the velocity influence in Smagorinsky and Spalart Allmaras model can last longer, or with another expression: a tight relationship in velocities of same point exists within a longer time distance in these two models as the other three. So that on the one hand, if with the same time step setting these two models can resolve bigger time-scale vortex in turbulence better. And on the other hand, the simulation time steps in these two models can theoretically be defined relatively bigger as the other three models as to seek better efficiency. However, considering that the former time step is limited between 6×10^{-7} and 1×10^{-6} , and the actual time step that chosen by the solver turns out to be 1×10^{-6} in all models by observing simulation "log" file. Extra efficiency overage can thus be used by rising the defined time step. By a roughly time step rising in all models to the initial value 5×10^{-6} and the maximum value 1×10^{-5} only the Spalart Allmaras model still converges. The model of Smagorinsky works without converging, which unexpectedly enhances the simulation time cost as the result, while the simulation for other three model even broken up after minutes of iteration. Consider only the successfully finished Spalart Allmaras model, all the acoustic and turbulent properties present the same behavior as the smaller time step case. In the mean while, the time cost changes promptly from about

4.2 Influence of The SGS Modeling on Turbulent Kinetic Energy Spectra and Correlation

23×56 per "hour/CPU" in MPPII¹ to 8.5×56 per "hour/CPU"! Therefore a suitable time step setting for different models can improve the simulation efficiency significantly, which might be an interesting point to study further.

4.2.3 Setting of Energy Spectra

Based on the theoretical analysis in Sec. 2.1.3, energy spectra can be generated with a Fourier transformation from velocity covariants. The spatial two-points covariant and auto-covariant can be Fourier transformed to spatial TKE spectra in wavenumber space and temporal TKE spectra in frequency space, respectively. Both energy spectra can be used to evaluate the time step setting and mesh quality. The Komogolov's $-5/3$ law (see Sec. 2.1.3) provides a useful criterion to distinguish the turbulence behavior for the considered SGS models. The Fourier transformation is implemented in the post-processing through obtained velocity series with help of a "Matlab" program. There are dozens functions to make Fourier transformation in "Matlab", and two of them: "fft" and "pwelch" is chosen in the following to do the transformation job.

"fft" Function

fft is short for **fast discrete Fourier transform(DFT)**, which transforms the data from time domain to frequency domain. The transformed function is normalized through dividing each transform by the square root of the signal (here velocity series) length, in order to preserve the signal energy and noise level. It is the most effective way to achieve a discrete Fourier transform, especially when the input data number can be written as 2^m . However, because of leakage phenomenon, which derives from an insufficient frequency resolution of DFT, this function always bring some problem by result analyzing. In signal or energy spectrum evaluation, another function "pwelch" is always preferred to smooth as well as optimize the concluded data by Fourier transform processes.

"pwelch" Function

pwelch is short for **Welch's power spectral density**. It calculates the PSD of a signal without knowing the Fourier transformed value, in the meanwhile a windowing implementation optimizes final data structure smoothly. Usually it performs better in a power signal, which can be regarded as infinite long broadband. However, in a limited time domain, the PSD can also be used to calculate the energy spectrum. A detailed derivation of the "pwelch" function is presented in Appendix A.2. The connection between the "pwelch" function and the "fft" function in time and frequency space is formulated here as:

$$\mathcal{D}_w(n) = \frac{|H_w[n]|^2}{N^2}, \quad (4.6)$$

where $\mathcal{D}_w(n)$ is a windowed PSD coefficient ("pwelch"), and $H_w[n]$ denotes a windowed discrete Fourier transformed signal and N is the windowed frequency number. Considering

¹MPPII is short for Massively Parallel Processing II, which is a cluster system of the LRZ.

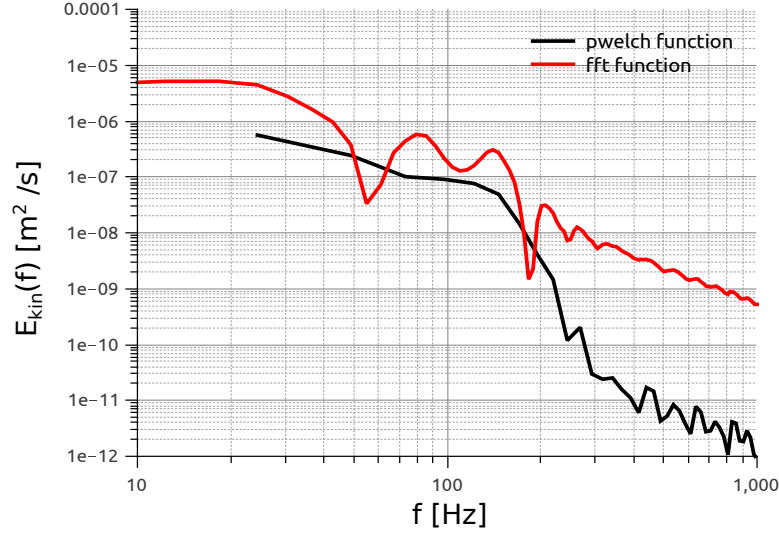


Figure 4.14: Temporal energy spectra with FFT and Pwelch function.

a so-called *Equivalent Noise Band Width* (ENBW):

$$ENBW = \frac{\sum_{k_i=0}^{N-1} r^2[k_i]}{(\sum_{k_i=0}^{N-1} r[k_i])^2} N \Delta f, \quad (4.7)$$

where $r[k_i]$ is a window function. With the help of ENBW, an empirical PSD is defined as:

$$\mathcal{ED}[n] = \frac{|H_w[n]|^2}{ENBW}. \quad (4.8)$$

In LES simulation with influence of input acoustic signals like in this work, empirical PSD in Eq. (4.8) suits better for reducing the effect of noise level.

The grammar of function *pwelch* for frequency space can following the similar estimation from Davidson [8] be written as:

$$[P_w \quad F_w] = \text{pwelch}(U_\theta, W, W_L, [], 1/\Delta t),$$

where P_w , F_w , U_θ , W , W_L and Δt donate the windowed PSD, windowed frequency, signal series (here resolved azimuthal velocity), window number, window overlapping number and the simulated time step as sample length, respectively.

Figure 4.14 presents a sample of the TKE curve computed by both "fft" and "pwelch" function with the same chronological U_θ series. Within the frequency range between 10 and 1000 Hz, three TKE spectrum ranges (see Sec. 2.1.3) are best constructed. The curve generated directly through "fft" function develops relatively flat without clearly showing the range difference. Further more the TKE fluctuations is relatively stronger with the growing of frequency domain. Since the mean velocity in this thesis is actually zero, if every monitored time points is considered, the velocity fluctuation switches between positive and negative sign very frequently, however, by considering a finite range of time domain, the averaging azimuthal velocity in each window space presents a comparatively less fluctuation,

4.2 Influence of The SGS Modeling on Turbulent Kinetic Energy Spectra and Correlation

and that is also why the window function can help to reduced the influence of background noise. In comparison, "pwelch" curve shows a definite improving tendency that reflect the Kolmogorov's Law (see Sec. 2.1.3) with a relative later curve beginning than the "fft". This starting point of "pwelch" function can be controlled by setting a suitable window length with the thinking of the whole simulation time range T_{whole} (here 0.03s) and the minimum detected frequency should be $f_{min} = 1/T_{min}$, which should be calculated in this simulation as 66.6 Hz ($2/T_{whole}$, 2 same period of sample can be recognized) in ideal cases. However, different factors like grid quality and SGS models can make also sense. But compared with the uncontrollability in "fft", it can be more reliable with "pwelch" in this situation.

Window Setting of "pwelch" Function

As discussed in the previous section, the "pwelch" function is called in Matlab as:

$$[P_w \ F_w] = pwelch(U_\theta, W, W_L, [], 1/\Delta t),$$

with W and W_L controlling the window setting. The meaning of these two parameters can be explained through Fig. 4.15, where L_w , L_o and L_{no} denote the window length, window overlapping length (both through the former and next window overlapped) and the not overlapping length, respectively. The complete data length $L_{data} = W \cdot L_w$, and the overlapped data length $L_{odata} = L_o \cdot W = L_w \cdot W_L$. In the algorithm of this function, once $L_w = L_{data}/W$ is calculated, all the settings can be generated perfectly. Since $L_{data} < L_{odata}$, a default condition included in the definition reads $W_L < W$. The default value of W_L can be called with "[]", which means the half of W number is used.

Figure 4.16 provides a comparison between different window numbers and overlapping number. Reducing the window number from 3750 step wise to 200, the curve changes as in Fig. 4.16a. With the number L_w increasing, the minimal resolved frequency becomes larger, while the curves turns out to be smoother. However, when the window number becomes smaller than 500, the curve will not strictly follow original curve running in all the three regions. Generally, the window number between 1000 and 2000 is to be preferred for both smooth and precise curve. In Fig. 4.16b, the window number L_w is chosen as 1000, different curves express the variety of window overlapping setting. However, no big

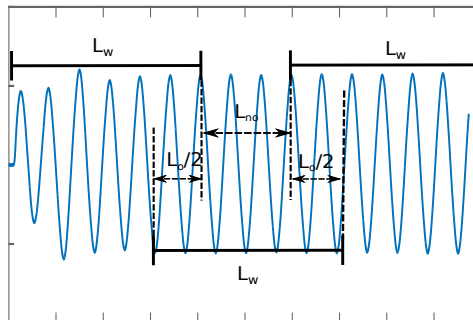


Figure 4.15: Window and the window overlapping in "pwelch" function.

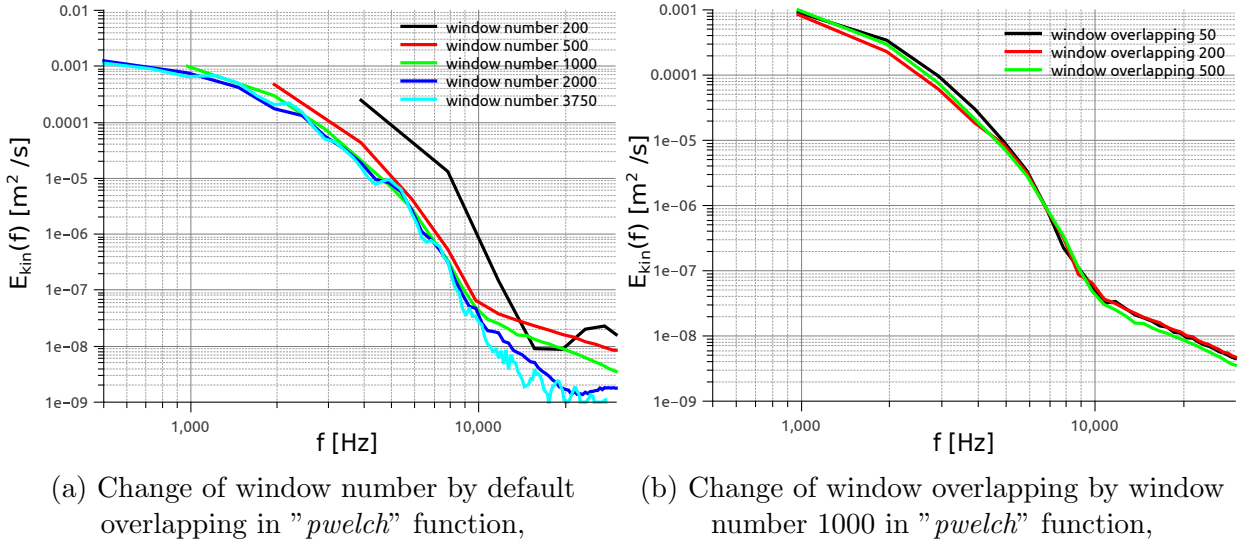


Figure 4.16: TKE spectra with different window settings with mesh HF in 130 dB.

difference can be noticed with only the changing of overlapping, so that in all the following analysis overlapping is set to Matlab default.

4.2.4 Turbulent Kinetic Energy Spectra

With preparations in the previous sections, analysis of both spatial and temporal spectra can be generated by Fourier Transform in this section. However, as more data can be achieved in a temporal velocity series, the further analysis in following sections are performed in frequency domain.

Spatial Energy Spectra

Spatial TKE spectrum is derived from two-points covariance $B_{U_\theta U_\theta}$ in Eq. (2.8) with a Fourier Transform. The simple method of "fft" will not be selected due to its bad prediction because of leakage. Instead, a "pwelch" transform is implemented, and the resulted series follows a windowed Fourier Transform in Eq. (4.8).

Figure 4.17 shows how the curves of different SGS model vary in a spatial energy spectra, where the X-axis is the wavenumber corresponding to grid length. According to this figure, all SGS models present reasonable curve performance the region II between about the wavenumber 5×10^3 to 2×10^4 in moderating the Komogolov's $-5/3$ law, which means all these models can accurately describe the turbulence behavior in this geometry as the discussion in acoustic part already proved. However, some difference can still be fund within these TKE values. According to the discussion in Sec. 4.2.2, as a full viscous stress tensor τ_{ij} is considered in Spalart Allmaras model, it presents with higher energy compared with other models as expected. However, it is quite unexpected, why the most energetic one turns out to be the one equation eddy model, while the similar dynamic model shows the least energy level. Since only limited numbers of velocity data are available in spatial

4.2 Influence of The SGS Modeling on Turbulent Kinetic Energy Spectra and Correlation

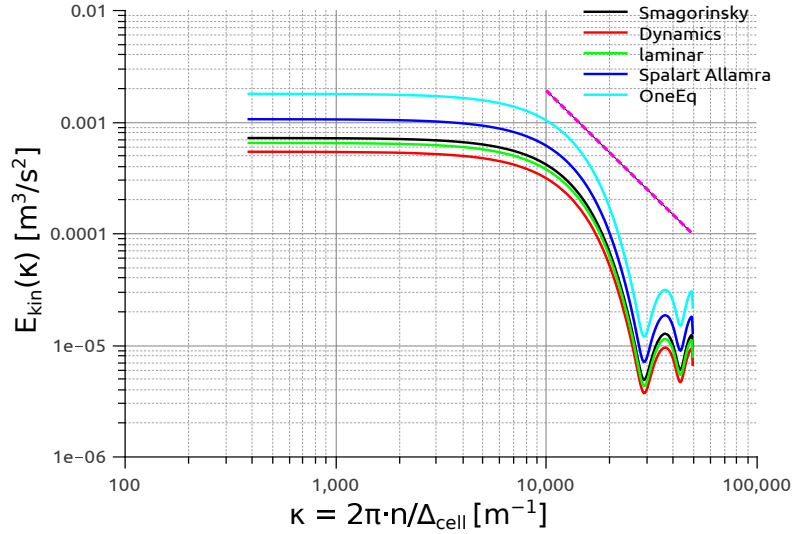


Figure 4.17: Spatial energy spectra with different SGS models.

spectra, all SGS models draw only with quite smooth curves, where detailed differences could actually be lost.

Temporal Energy Spectra

Different from spatial energy spectra, temporal energy spectra of TKE base theoretically on the auto-covariance in Eq. (2.12) with a subsequent performance of the Fourier Transform. In the algorithm the "pwelch" function is used of for velocity $U'(t)$ series. With adjusted window settings, data visualization of temporal energy spectra for both Hersh and Förner's geometry are expressed in Fig. 4.18. In both geometry a frequency that close to their resonator eigenfrequency (580Hz and 380Hz) are chosen to make the turbulence behavior stronger with their resonance.

In Fig. 4.18a with a Hersh's geometry "FH", the curves in region II and III can be recognized from frequency range 500Hz to 4000Hz and after 4000Hz, respectively. Spalart Allmaras, dynamic, Smagorinsky and even laminar model draw only similar curves with $-5/3$ slop in region II. As expected, Spalart Allmaras model has the highest TKE compared with the other three models. However, a irregular development can be observed in one equation eddy line, where an unexpected turn point at about 1050Hz exists. In modeling homogeneous turbulent scales region III, all models act similar without any noticeable energy difference. Energy spectra in Förner's geometry "MF" are presented in Fig. 4.18b, where all the three regions can be easily recognized. In region I from 500Hz to about 1000Hz, all models extend flatly with only lower energy in model one equation eddy and Smagorinsky. In region II up to 8000Hz, five curves end up with almost the same TKE value. Compared with Fig. 4.18a, unstable curves are presented in region III, which proves stronger influence caused by resonance can exist when the orifice diameter to length ratio becomes smaller.

Concluded from the correlation and the TKE spectra analysis, the variation of SGS models also leads to a small difference in flow properties at a Helmholtz Resonator. How-

ever, in order to reduce the acoustic effect in analyzing, the azimuthal velocity is preferred, such as transform error arises in one equation eddy based models. In TKE spectra running some unexpected phenomena occur also special in one equation eddy model, which make it unreliable. Compare the other three models, Spalart Allmaras model performs always better in both correlations and TKE spectra analysis. In the following discussion, this model is utilized without further emphasize.

Ignoring the difference caused by SGS models, there are still some factors that changes the TKE spectra characters, which can have even more significant influence. Therefore conditions like in following sections should be considered carefully by the setup of simulations.

4.2.5 Energy Spectra with different SPLs

In our discussion, turbulence is generated simply through the acoustic excitation from inlet. No turbulence would even exist for low SPL numbers, in contrast however, turbulence should becomes stronger by an enhanced SPL. A quantified analysis in this section investigates the SPL influence on turbulence character with the specialty of TKE spectra.

Figure 4.19 presents typical TKE spectra corresponding to different SPLs in both Hersh's and Föner's geometries "FH" and "FM". Focusing first on the "FM" mesh in Fig. 4.19b, for different SPL numbers, the available transferred energy from acoustic to turbulent also differs. Therefore, in each discrete frequency number, a TKE difference can be distinguished in this figure. Leaving out the 105 dB line, the region I&II as well as region II&III separations can be recognized in 120 dB and 125 dB at about 1050 Hz and 8000 Hz, respectively. Since a clear $-5/3$ slop are measurable in those two lines. However, from the 105 dB curve, no such slop can be found. It can be concluded that for that low SPL as 105 dB no turbulence structure develops. A comparable acoustic influence is also figured out in Sec. 4.1.3. By Hersh's geometry "FH", the "pwlch" has windowed out the curves of region I in all models. Only the separation between region II and III can be found out at about

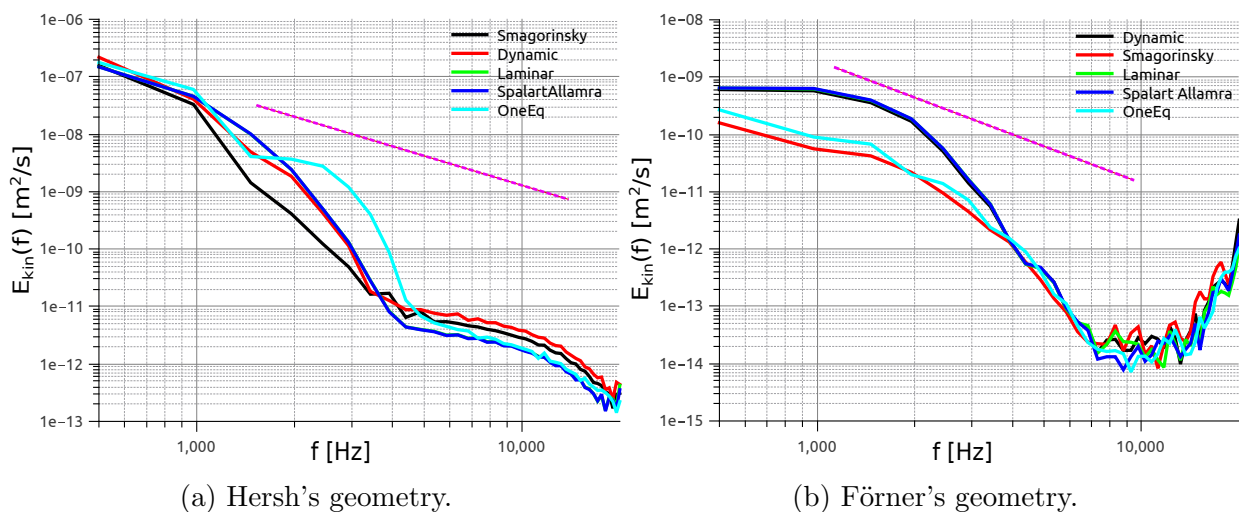


Figure 4.18: Temporal energy spectra with different SGS models in 120 dB SPL.

4.2 Influence of The SGS Modeling on Turbulent Kinetic Energy Spectra and Correlation

10500 Hz. As presented also in Förner’s case, the $-5/3$ slop can only be recognized in high energy curves. In low energy curve as the 110 dB one, very flat slop means no homogeneous full turbulence is structured by the acoustic signal, where the Kolmogolov’s ” $-5/3$ ” law also vanishes. However, the most obvious difference between these two geometry is presented in high SPL curves. No markable difference between the 130 dB and 140 dB curves can be found in Fig. 4.19a. An assumption is that by very high SPL of about 130 dB to 140 dB, homogeneous turbulence is generated in all directions in Helmholtz Resonator, where the dissipation also reaches its highest level. So that the generated turbulence can not absorb more acoustic energy except those to balance the dissipation. This can also be proven in acoustic part of Fig. 4.8, where the absolute value of reflection coefficient \mathcal{R}_f for 140 dB reads 0.16 and for 120 dB and 130 dB reads about 0.45.

4.2.6 Position and Mesh Quality Effect in Energy Spectra

Above discussions are only valuable when the same grid meshes and investigated points are used. As an addition part, how these two factors influence the simulation will be estimated in this section. The influence of detected position will be discussed as the first part.

Position Variation

Variation in axial direction	$x = 3l_n$	$x = 6l_n$
Point names	XV1	XV2

Table 4.2: Position variation in axial direction with $R = 0.5l_n$.

As shown in Fig. 4.20 and Tabs. 4.2, 4.3, 4.4, three different position variations in axial, radial and azimuthal directions are discussed in this section, respectively. All these simulation above are compared with the same mesh ”HF”. Temporal TKE spectra are used for comparison in-depth.

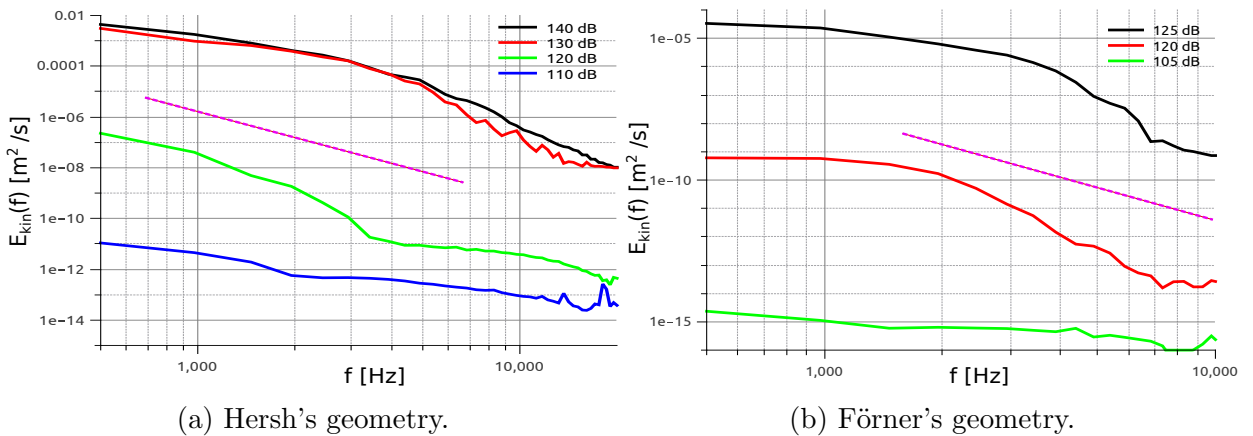


Figure 4.19: TKE spectra with different SPLs.

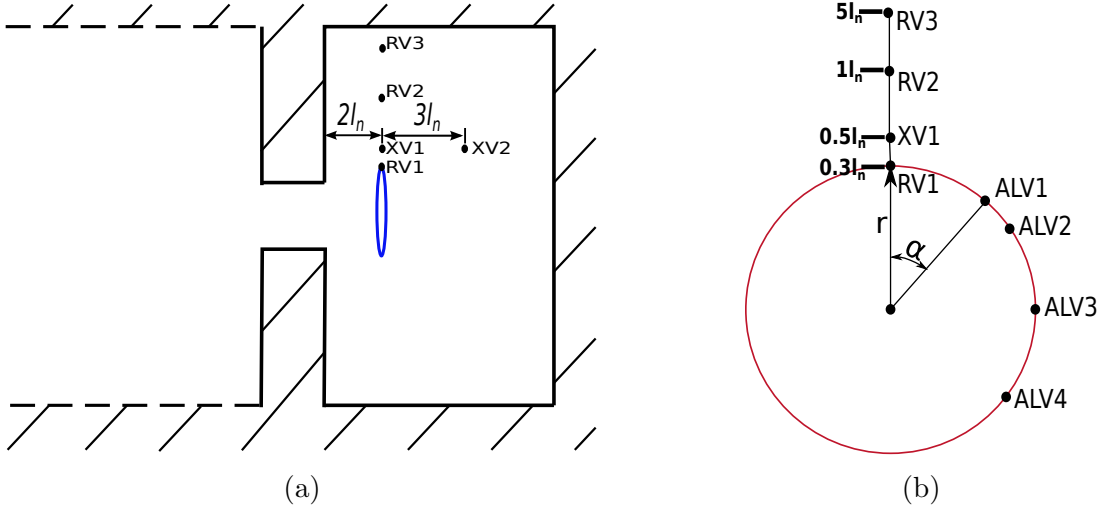


Figure 4.20: Position of detected points.

Variation in radial direction	$R = 0.3l_n$	$R = l_n$	$R = 5l_n$
Point names	RV1	RV2	RV3

Table 4.3: Position variation in radial direction with $x = 3l_n$.

Variation in azimuthal direction	$\alpha = \pi/4$	$\alpha = \pi/3$	$\alpha = \pi/2$	$\alpha = 3\pi/4$
Point names	ALV1	ALV2	ALV3	ALV4

Table 4.4: Position variation in azimuthal direction with $x = 3l_n$, $R = 0.3l_n$

Results of temporal TKE spectra variations according to different axial positions and SPLs are presented in Fig. 4.21. As expected, the more distance to neck located point XV2 always turns to be the less energetic one compared with the spectra of point XV1 also with different SPLs. By lower SPL, turbulent character is more obvious by points XV1 for his better following of "-5/3" law. By higher SPL, variation of axial direction becomes smaller for the better development of turbulent structures.

Similar comparison can also be made for variations in radial and azimuthal directions as shown in Fig. 4.22. SPL 120dB is chosen since from above axial comparison, more difference can be expressed by lower SPL. However, variations of both directions are quite small if compared with that of axial direction, which means the turbulence is therefore more homogeneous in these two directions.

Mesh Quality Variation

Besides position variations, different mesh qualities also influence the final result. Since fine mesh can express turbulence with small scales better as the coarse one.

Figure 4.23 present the result of temporal TKE spectra comparison for different mesh

4.2 Influence of The SGS Modeling on Turbulent Kinetic Energy Spectra and Correlation

of Hersh's geometry. As expected, the spectrum with coarse mesh turns to be the least energetic one since some smallest turbulent scales can't be modeled. That part of energy is therefore lost. However, the energetic spectra variation between middle and fine mesh of Hersh's geometries "HM" and "HF" is quite small. According to the discussion of spatial correlation in Sec. 4.2.2, over eight cells are available for each smallest turbulent scale in mesh "FH". Usually only four cells are required for a precise simulation, which may be the case of middle sized mesh "MH".

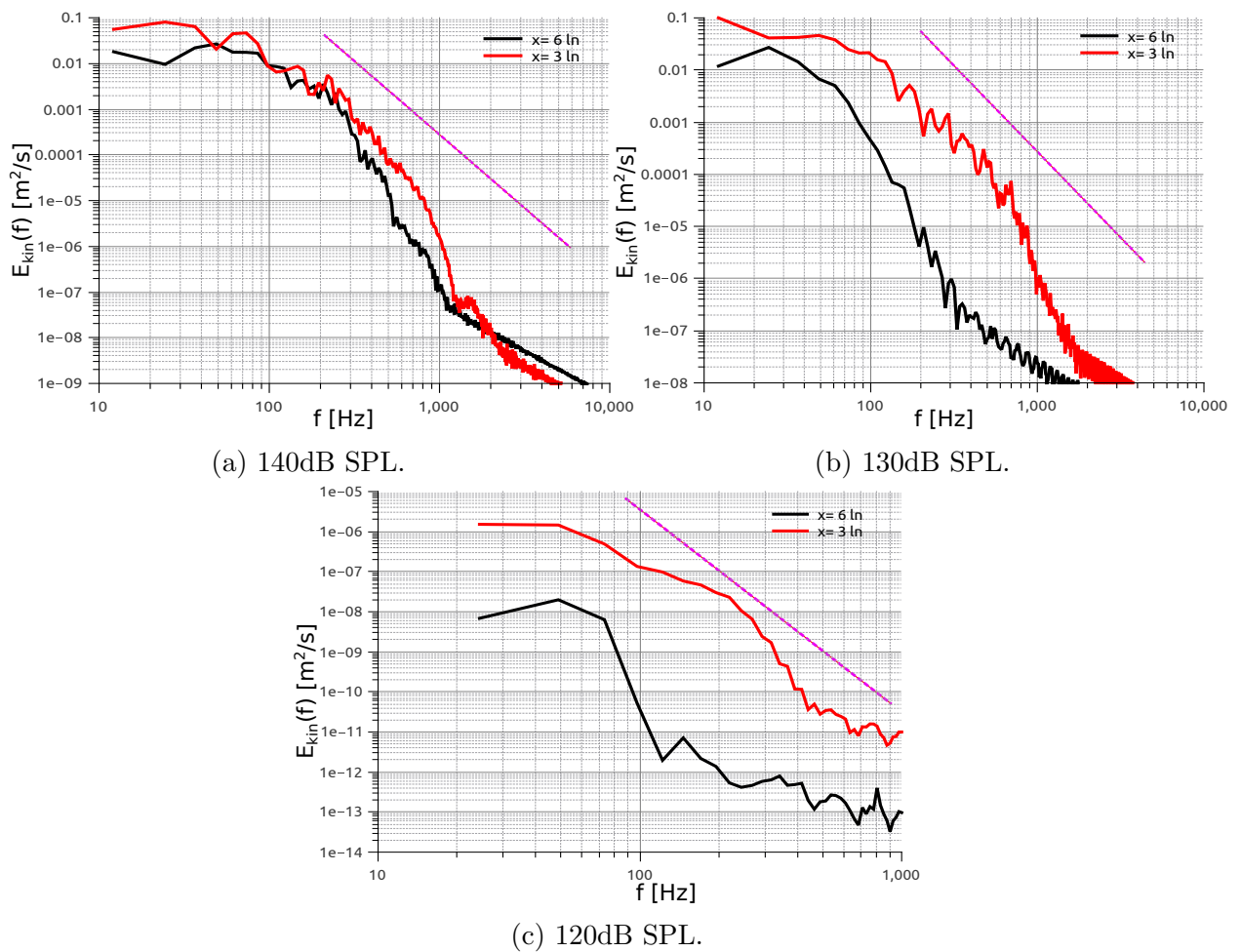


Figure 4.21: Temporal TKE spectrum with different axial positions and SPLs.

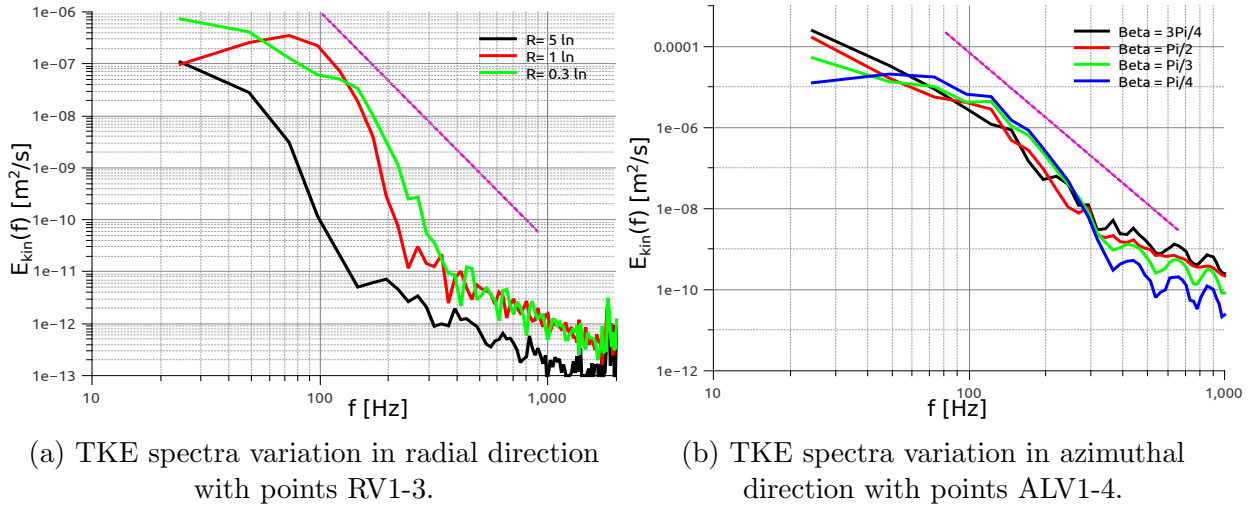


Figure 4.22: Temporal TKE spectra with different radius (left) and angles (right).

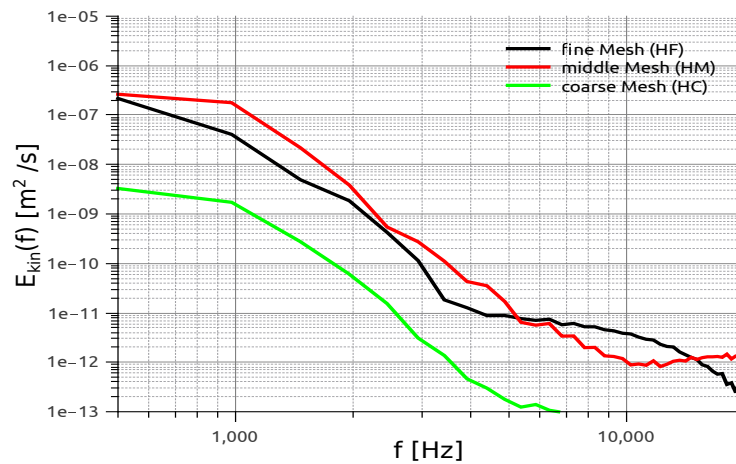


Figure 4.23: Temporal TKE spectra with different mesh qualities according to point XV1.

4.3 SGS Comparison In Other Criteria

4.3.1 Visualization Through Vorticity and Q-Criterion

Above discussions are made through different acoustic and fluid dynamic criteria, which includes a lot of indirect mathematical graphics. However, a visualization of turbulent structures can also be presented through some turbulent characteristics like vorticity and Q-criterion. These can also be treated as judgments to evaluate turbulent developments through LES SGS models in this thesis.

Figure 4.24 shows the comparison of Q-criterion as well as vorticity among different LES SGS models. The backgrounds of resonator are colored with logarithmic vorticity and the bubble structures are defined through isosurface of Q-criterion with the value 1000. As expected from above estimations, at the same instant in time the differences among all SGS models are small. Considering the background of logarithmic spectrum expressed vorticity, similar high values mainly located in resonator orifice range. More obvious differences can

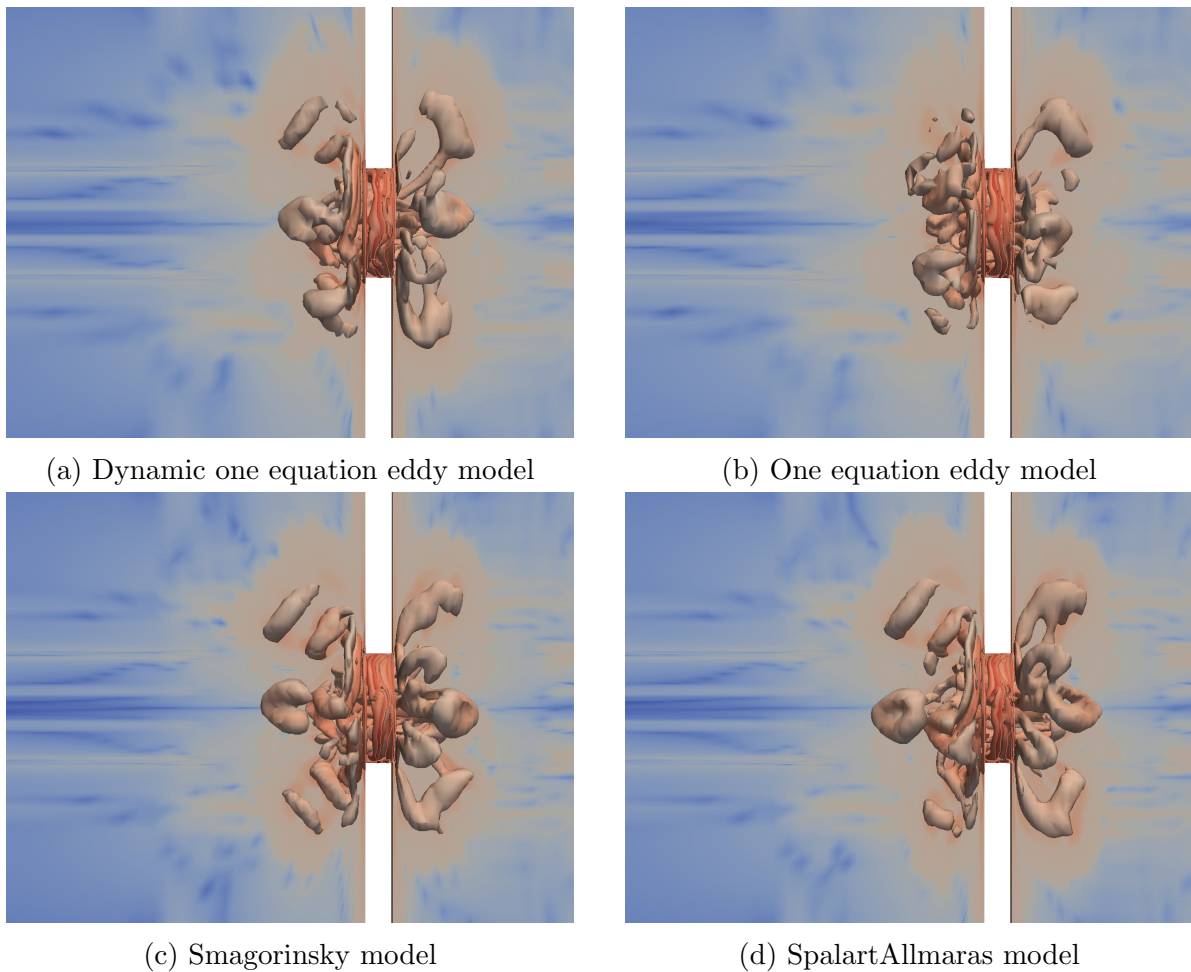


Figure 4.24: Turbulence structure visualization with different SGS models with logarithmic vorticity background and Q-criterion isosurfaces of value 1000.

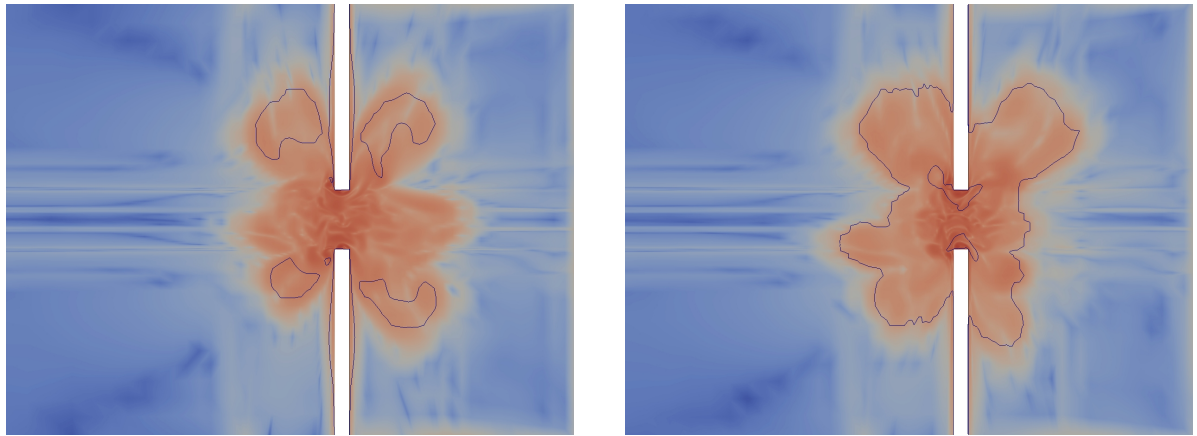
be found in Q-criterion, where OneEqEddy model shows less "bubbles" also with smaller bubble filled ranges. Among all the other models, Spalart Allmaras model represents more details within Q-criterion also with a larger effected range. It means in this model, simulated turbulence influences a larger flow range within the resonator. That may be caused by more effective acoustic energy absorption within this model. Besides these two models, Smagorinsky model is more like the Spalart Allmaras, while the dynamic model presents more similarity to the OneEqEddy.

4.3.2 $k_{RES}/k_{SGS} = 4$ Criterion

Another criterion can be called as, $k_{RES}/k_{SGS} = 4$ criterion, where k_{RES} the resolved kinetic energy of flows and k_{SGS} the modeled energy through SGS definition. According to Pope's book [12], where the ratio over 4 can be treated as range that is suitable for the usage of LES SGS model. However, the ratio under 4 should be regarded as less effective. As can be expected, this criterion can be influenced both by SGS models and mesh quality in this case.

In Fig. 4.25, the $k_{RES}/k_{SGS} = 4$ criterion of one equation eddy models and Homogeneous dynamic one equation eddy model model are compared, since in the value of k_{SGS} is easier to obtain in these models. Also with logarithmic vorticity spectrum background, blue lines as $k_{RES}/k_{SGS} = 4$ contour lines encircled the range, where this ratio smaller as 4. Generally the encircled area also covers the high vorticity value range, especially for the dynamic model. However, the contour lines surrounds less area in OneEqEddy model as the dynamic one, which means this model is more suitable for the simulation here according to this criterion. Another difference that can be noticed here locates in the boundary region. Some areas at boundary layer before and behind the resonator orifice are also surrounded by the contour lines for the OneEqEddy model, which is caused by the unchangeable definition coefficient within the definition of model. Since the dynamic model also adapts these coefficients during the simulation processes, smoother contour lines can thus be followed along the boundary layer.

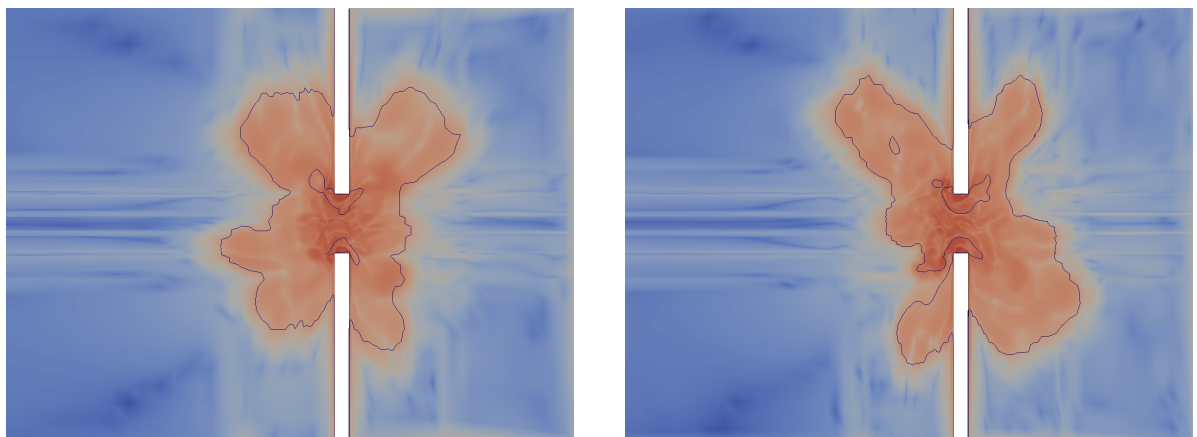
Similar comparison can also be made for different mesh qualities like Fig. 4.26. This time Homogeneous dynamic oneEqEddy model is used, since OneEqEddy model already shows good performance even for the middle sized mesh. However, according to the result in Fig. 4.26, finer mesh will not help to make the case suitable for dynamic model, as only a very small range of by contour lines surrounded area is freed. The only advantage is, that turbulence in the backing volume seems to be improved for for dynamic model, with smaller encircled areas.



(a) OneEqEddy model.

(b) Homogeneous dynamic oneEqEddy model.

Figure 4.25: $k_{RES}/k_{SGS} = 4$ criterion (blue contour lines) for OneEqEddy and Homogeneous dynamic oneEqEddy model model.



(a) With middle mesh.

(b) With fine mesh.

Figure 4.26: $k_{RES}/k_{SGS} = 4$ criterion (blue contour lines) by Homogeneous dynamic oneEqEddy model model for different mesh sizes.

4.4 Turbulence Judgment

With the similarity in all LES SGS models, it is necessary to judge whether the generated vorticity really means turbulence. A criterion already used is the Kolmogorov's "-5/3" law in TKE spectra. Better following of that slope can be found in the region II of temporal spectra as Fig. 4.18. However, the spatial spectra shows lacking quality by this criterion as Fig. 4.17. Another criterion is the ratio of turbulent viscosity to molecular viscosity ν_{SGS}/ν . The complete simulated flow viscosity can be expressed as sum of these two viscosities. Turbulent viscosity ν_{SGS} is a modeled parameter in OpenFoam which is theoretically various defined according to different models like Eqs. (2.65), (2.71). The molecular viscosity can be computed through Sutherland's law [34] as:

$$\nu = \frac{A_s T^{3/2}}{(T + T_s)\rho}, \quad (4.9)$$

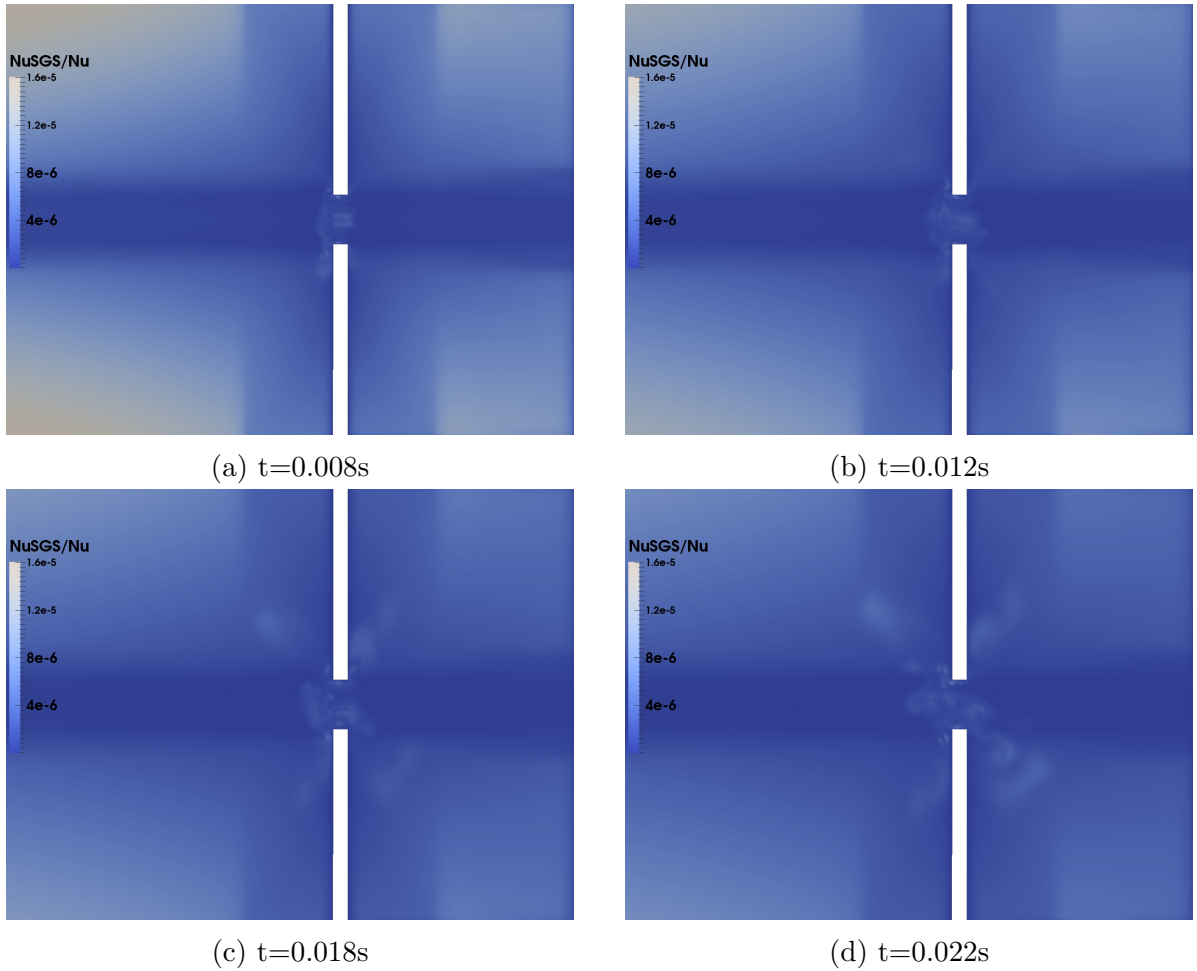


Figure 4.27: Criterion of ν_{SGS}/ν for Spalart Allmaras model in neck range with different time points.

4.4 Turbulence Judgment

where the constants A_s and T_s are defined as $1.4792 \times 10^{-6} \frac{kg}{ms\sqrt{K}}$ and $116K$, respectively. The ratio can be very large to over 100 in some turbulent boundary layers, and quite low in laminar flows. In turbulent open flow, the value should be between these two conditions. As a general case in Spalart Allmaras model in Sec. 2.1.5, the ratio is 2.97×10^{-7} in free stream.

Figure 4.27 shows how the ratio of ν_{SGS}/ν develops with time close to neck of Helmholtz Resonator by Spalart Allmaras model. It can be found, that the ratio of expressed turbulent structures is generally quite small at about 10^{-5} . It is larger than the value for the free stream of 2.97×10^{-7} , which means turbulent structures in this region are indeed generated. However, with such small number of ratio, the influence of SGS modeled structure to the complete system becomes perspective minimal, which results the high similarity in simulation in all SGS models as well as the laminar one. The absolute value of this ratio also shows no change over time even with an enlarged influenced ranges, so that the similarity of all SGS models vary also quite small over time.

5 Conclusion and Outlook

5.1 Conclusion

Turbulent flow is such kind of three dimensional chaotic flows that includes a large number of length and time scales. Especially in Helmholtz Resonator, the turbulent structures can be strongly influenced by acoustic waves, which results also in inhomogeneity within the structure. Therefore, a careful simulation setup in OpenFoam as well as suitable parameter and criteria selection for estimation is needed.

The turbulence here is assessed through a LES approach, with different compressible SGS models implemented in OpenFoam. Without mean flow, turbulence is completely generated by acoustic waves in this work, which makes the turbulent behavior different from usual ones. To deal with the inhomogeneity and reduce the acoustic perturbation effect, azimuthal velocity is utilized instead of axial and radial ones for the data post-processing.

In the acoustic part, parameter variation of different SGS models, SPLs and mesh qualities are investigated to ensure the findings. Nonlinear behavior of resistance is used to compare the difference between SGS models as well as the experimental data. However, almost all models, including the laminar one, showed quite similar results. The Spalart Allmaras model turns out to be the closest to the experimental data. This conclusion is also true for changed SPLs. However, the difference between simulated and experimental data increases by SPL growth. Reflection coefficient difference according to SGS models is proven to be even minor. But with different SPLs, the amount of energy proportion that absorbed through turbulence also changes, which resulted in the inconstant value of reflection coefficient as well as the nonlinear resistance.

In the fluid dynamic part, both criteria of correlations and TKE spectra are based on azimuthal velocity. Spatial correlation can only be calculated with by hand predefined probe points, which shows whether the mesh is suitable for the used SGS model. As result, all SGS models perform quite well in spatial correlation as to model the smallest turbulent length scales properly. Compared with the spatial one, temporal correlations present the simulated turbulence qualities in time scales, where the Spalart Allmaras model also shows best characteristics. Both spatial and temporal correlations can be Fourier transformed to TKE spectra, with spatial spectrum according to wave numbers and temporal spectrum according to frequency. Komoglove's "-5/3" law helps to adjudicate the turbulence performance in both spatial and temporal spectra. Such kind of slope can be found in all simulations for the different SGS models. Additionally, Spalart Allmaras model shows to be more energetic. SPLs influence TKE spectra also significantly, since by lower SPL no "-5/3" slope can be found. However, at very high SPLs, since reflection coefficient rises and absorbed acoustic energy proportion drops, the energy included in the spectrum changes

minorly.

5.2 Outlook

Since no mean flow is regarded as the basic condition in this thesis, turbulence is simply generated through acoustic waves. However, in a more general case, pruging or grazing flow can also generate turbulence in a pure fluid dynamic way. In that case, turbulence becomes a action that is influenced by both flow velocity and acoustic properties, where the intensity of turbulence may also increase. How different LES SGS models perform in that more industrial condition is still unknown. Besides, a connection between spatial and temporal TKE spectra as the "frozen turbulence hypothesis" might be validated, which provides another fluid dynamic judgment criterion for future works.

Appendices

A Theoretical Deviations

A.1 Deviation of Helmholtz Resonator Equations

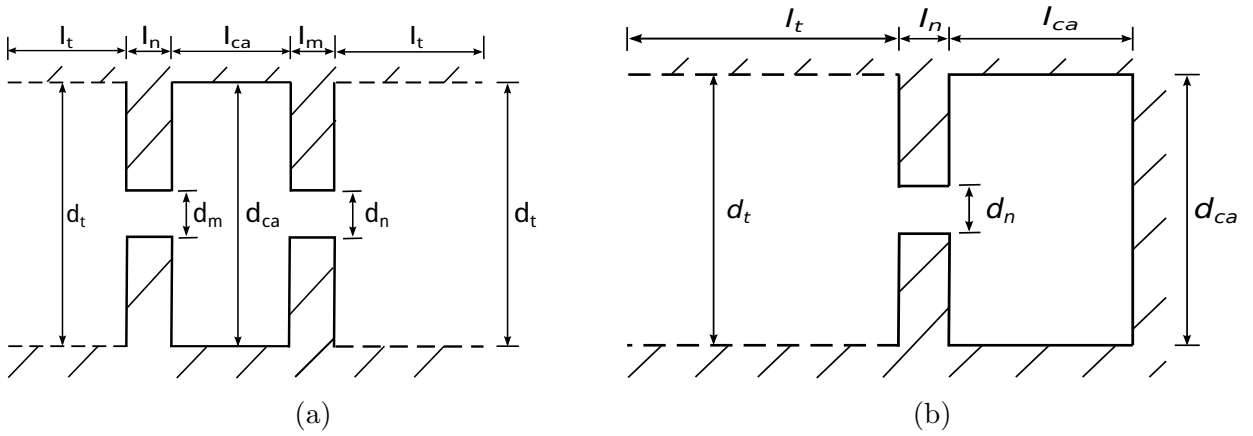


Figure A.1: General Helmholtz Resonator with original acoustic wave f (left) and Helmholtz Resonator with original and reflected acoustic wave f, g (right)

Figure A.1a is a typical general resonator geometry, which consist of the outside tube, neck part, and resonator cave. Physically, the resonator acts like a mass-spring-damper system [6]. The mass in neck part and resonator cave is accelerated by the pressure fluctuating from outside tube. The so caused flow motion, especially in near of the neck wall region, results viscous losses, which turns to flow separation with increasing excitation amplitudes. These separation converts the acoustic energy to hydrodynamic mode, which means laminar flow fluctuation by moderate excitation level but turbulent vortices by large levels [6]. When the acoustic wave frequency is close to the resonator eigenfrequency, the strongest acoustical losses appears, where the turbulence also mostly exist.

In Figure. A.1a, l_t , l_n and l_{ca} represent the length of computed outside tube, the length of two resonator necks and the height of resonator cave, respectively. In the mean while d_t reads the diameter of computed outside tube, d_n and d_m the diameter of orifice and d_r the diameter of resonator.

With the help of Fig. A.1a, we can derive a physical and mathematical describing for the general resonator from basic mass and momentum conservation by following Keller and Zauner's model [3]. The mass equation between the region of necks n and m can be described as:

$$\frac{\partial \rho}{\partial t} V = (U_n + u_n) \rho A_n - (U_m + u_m) \rho A_m, \quad (\text{A.1})$$

where U_n and U_m represent the mean flow velocities in neck regions n, m respectively, and the u_n, u_m, A_n, A_m the departure velocities and flow areas of them. This mass conservation can theoretically also be formulated only for the mean flow:

$$U_n A_n - U_m A_m = 0. \quad (\text{A.2})$$

Combine Eq. (A.1) and (A.2), the mass conservation for only departure velocities can be written as:

$$\frac{\partial \rho}{\partial t} V = U_n \rho A_n - U_m \rho A_m. \quad (\text{A.3})$$

For the momentum equation, only the orifice region m will be first considered. The equation can then be written as:

$$A_m l_m \rho \frac{\partial u_m}{\partial t} = A_m P_{ca} - A_m \zeta_m \frac{\rho}{2} (U_m + u_m) |U_m + u_m| - A_m P_t, \quad (\text{A.4})$$

where the first and third terms on the right hand-side read the pressure difference between the resonator cave and outside tube, the second term on right hand-side accounts for the force due to the acceleration of fluid from pulsation system in resonator cave into the tube element through orifice m . This force depends on the sign of velocity $U_m + u_m$. ζ_m is a loss coefficient, which defined as $\zeta_m = 1 - \left(\frac{A_{ca}}{A_m}\right)^2$. $\zeta_m = 1$ by loss-free cases, otherwise $\zeta_m < 1$.

Now the Helmholtz Approximation can be introduced as: the effect from difference of density in time serious is much smaller as that from difference of velocity. Mathematically the definition can be expressed as:

$$\mathcal{O}\left(\frac{\partial \rho}{\partial t} \frac{\partial u_m}{\partial t}\right) \ll \mathcal{O}\left(\rho \frac{\partial^2 U_m}{\partial t^2}\right), \quad (\text{A.5})$$

$$\mathcal{O}\left(\frac{\partial \rho}{\partial t} [U_m + u_m]\right) \ll \mathcal{O}\left(\rho \frac{\partial U_m}{\partial t}\right). \quad (\text{A.6})$$

Differentiating Eq. (A.4) with respect to time and then reduce it by using Eq. (A.5) (A.6) yields:

$$l_m \rho \frac{\partial^2 u_m}{\partial t^2} = \frac{\partial P_{ca}}{\partial t} - \zeta_m \rho \frac{\partial u_m}{\partial t} (U_m + u_m) - \frac{\partial P_t}{\partial t}. \quad (\text{A.7})$$

Suppose the acoustic wave f and g in Eq. (2.107) and (2.108) to be harmonic, which can be expressed as:

$$f = a \exp\left(i\omega t + \frac{i\omega x}{c} + \varphi x\right), \quad (\text{A.8})$$

$$g = b \exp\left(i\omega t - \frac{i\omega x}{c} - \varphi x\right). \quad (\text{A.9})$$

where $\varphi \ll \omega/c$, and following Rott and Hartunian φ can be defined as:

$$\varphi = [1 + i] \frac{\sqrt{2\omega\nu_{air}}}{D_t c} \left[1 + \frac{\gamma - 1}{\text{Pr}^{1/2}}\right]. \quad (\text{A.10})$$

A.1 Deviation of Helmholtz Resonator Equations

In this equation, D represents the diameter of tube and ν_{air} the kinetic viscosity of air. In symmetric case $a = b$, U' and P' in Eq. 2.107 and (2.108) can be expressed as:

$$U' = f - g = ae^{i\omega t} \cosh\left(\frac{i\omega x}{c} + \varphi x\right) \approx ae^{i\omega t}, \quad (\text{A.11})$$

$$P' = \rho c(f + g) = -ae^{i\omega t} \sinh\left(\frac{i\omega x}{c} + \varphi x\right) \rho c \approx -ae^{i\omega t} \left(\frac{i\omega x}{c} + \varphi x\right) \rho c. \quad (\text{A.12})$$

With the consideration of thermal boundary layer, a coefficient \mathcal{T} can be write as:

$$\mathcal{T} = \frac{1 + \frac{\gamma-1}{Pr^{1/2}}}{D_t} \sqrt{\frac{2\nu_{air}}{\omega}}. \quad (\text{A.13})$$

For the orifice region m , Combination of Eq. (A.10), (A.11) and (A.12) yields:

$$P'_{ca} - P'_t = [1 + \mathcal{T}]\rho l_m \frac{\partial U'}{\partial t} + \mathcal{T}\rho l_m \omega U' \quad (\text{A.14})$$

Now turn back to the Eq. (A.4). Consider also the thermal boundary layer with Eq. (A.14), it can be reduced as:

$$[1 + \mathcal{T}_m]l_m \rho \frac{\partial^2 u_m}{\partial t^2} = \frac{\partial P_{ca}}{\partial t} - \zeta_m \rho \frac{\partial u_m}{\partial t} |U_m + u_m| - \mathcal{T}_m l_m \rho \omega \frac{\partial u_m}{\partial t} - \frac{\partial P_t}{\partial t}, \quad (\text{A.15})$$

$$\mathcal{T}_m = \left[1 + \frac{\gamma - 1}{Pr^{1/2}}\right] \sqrt{\frac{\pi \nu_{air}}{2\omega A_m}}. \quad (\text{A.16})$$

The same strategy can also be used in orifice region n , which leads:

$$[1 + \mathcal{T}_n]l_n \rho \frac{\partial^2 u_n}{\partial t^2} = \frac{\partial P_t}{\partial t} - \zeta_n \rho \frac{\partial u_n}{\partial t} |U_n + u_n| - \mathcal{T}_n l_n \rho \omega \frac{\partial u_n}{\partial t}, \quad (\text{A.17})$$

As we supposed the time-dependent part of pressure in pulsating system (the tube) is harmonic oscillated:

$$P_t = [P_t] - P_t^* \sin(\omega[t - t_0]), \quad (\text{A.18})$$

where $[\cdot]$ refers to time average and t_0 accounts for a shift of original time coordinate which should be chosen suitably. Suppose the time changing of average pressure is incredibly small: $\frac{\partial [P_t]}{\partial t} = 0$, Eq. (A.15) is reduced to:

$$[1 + \mathcal{T}_m]l_m \rho \frac{\partial^2 u_m}{\partial t^2} = \frac{\partial P_{ca}}{\partial t} - \zeta_m \rho \frac{\partial u_m}{\partial t} |U_m + u_m| - \mathcal{T}_m l_m \rho \omega \frac{\partial u_m}{\partial t} - \omega P_t^* \cos(\omega[t - t_0]). \quad (\text{A.19})$$

Another translation can be included here but actually only strictly valid for isotropic flow:

$$\frac{\partial P_{ca}}{\partial t} = c^2 \frac{\partial \rho}{\partial t}. \quad (\text{A.20})$$

Then the combination of Eq. (A.3) and (A.20) yields:

$$\frac{\partial P_{ca}}{\partial t} = \frac{A_n u_n \rho c^2}{V} - \frac{A_m u_m \rho c^2}{V}. \quad (\text{A.21})$$

As a direct outcome from pressure oscillation, the velocity in orifice m and n can also be represented as harmonic oscillation form. However, the time shift t_0 and position difference finally results a time delay ς for the velocity in orifice n . All these two velocities can be formulated as:

$$u_m = u_m^* \sin(\omega t), \quad u_n = -u_n^* \sin(\omega[t - \varsigma]) \quad (\text{A.22})$$

Now combine all the strategies and derivations above and eliminates the P_t term, the momentum equation will finally transferred for the orifice m and n like:

$$(1 + \mathcal{T}_m)l_m\rho\frac{\partial^2 u_m}{\partial t^2} + \frac{A_m\rho c^2}{V}u_m - \frac{A_n\rho c^2}{V}u_n = -\zeta_m\rho\frac{\partial u_m}{\partial t}|U_m + u_m| - \mathcal{T}_m l_m \rho \omega \frac{\partial u_m}{\partial t} + \frac{\partial P}{\partial t}, \quad (\text{A.23})$$

$$(1 + \mathcal{T}_n)l_n\rho\frac{\partial^2 u_n}{\partial t^2} + \frac{A_n\rho c^2}{V}u_n - \frac{A_m\rho c^2}{V}u_m = -\zeta_n\rho\frac{\partial u_n}{\partial t}|U_n + u_n| - \mathcal{T}_n l_n \rho \omega \frac{\partial u_n}{\partial t}. \quad (\text{A.24})$$

Now we can turn back to the special case which this thesis really interested in, the Helmholtz Resonator like Figure. A.1b shows. Compare with the general resonator, Helmholtz Resonator can be mathematically simplified as: $A_n = 0$ $t_0 = 0$ $U_n = U_m = 0$, so that the momentum equation can be reduced as:

$$(1 + \mathcal{T})l_m\rho\frac{\partial^2 u}{\partial t^2} - \frac{A_m\rho c^2}{V}u = -\zeta\rho\frac{\partial u}{\partial t}|u| - \mathcal{T}l_m\rho\omega\frac{\partial u}{\partial t} - \frac{\partial P}{\partial t}. \quad (\text{A.25})$$

As the acoustic resonator is always described in the form of frequency, the Eq. (A.18) and (A.22) from above deviation can also be formulated in the form of $u = u^*e^{i\omega t}$, $P = P^*e^{i\omega t}$. The Eq. (A.25) should be rewritten as:

$$(1 + \mathcal{T})l_m\rho\omega i u^* + (\mathcal{T}\rho l_m \omega + \zeta\rho u^*)u^* - \frac{A\rho c^2}{V\omega}i u^* = -P^*. \quad (\text{A.26})$$

A.2 The Definition Of "pwelch" Function

The following derivation of "pwelch" function according to Miranda [35] writes in frequency space since more velocity data in time domain is available, so that in the analysis part more detailed comparison runs easily. Considering the discrete periodic time signal $h[k_i]$:

$$h[k_i] = \sum_{k=-\infty}^{\infty} x(k_i t_s) \delta(t - k_i t_s), \quad (\text{A.27})$$

where the t_s samples the time, and k_i the time instants, such as the Fourier transform in Eqs. (2.22) 2.21 is written in discrete meaning:

$$h[k_i] = \sum_{n=0}^{N_0-1} c_n e^{i2\pi\frac{nk_i}{N_0}}, \quad (\text{A.28})$$

A.2 The Definition Of "pwelch" Function

$$c_n = \frac{1}{N_0} \sum_{k_i=0}^{N_0-1} h[k_i] e^{-i2\pi \frac{nk_i}{N_0}} \quad (\text{A.29})$$

with N_0 acts as the discrete fundamental period. In more common non-periodic signal, a frequency space is preferred as:

$$H(f) = \sum_{k_i=-\infty}^{\infty} h[k_i] e^{-i2\pi f k_i}. \quad (\text{A.30})$$

Different from the $h[k_i]$, Hf definite mainly in continuous space, which make the PSD definition possible like:

$$\Pi(f) = \lim_{N \rightarrow 0} \frac{|H(f)|^2}{2N}. \quad (\text{A.31})$$

However Eq. (A.30) is also true in a infinite numbers of data series $N < \infty$, where the Discrete Fourier Transform (DFT) acts:

$$H(n) = \sum_{k_i=-\infty}^{\infty} h[k_i] e^{-i2\pi \frac{nk_i}{N}}. \quad (\text{A.32})$$

Combined with Eq. (A.29), the coefficient c_n and Power Spectrum $\mathcal{D}(n)$ can be simply expressed as:

$$c_n = \frac{H[n]}{N}, \mathcal{D}(n) = \frac{|H[n]|^2}{N^2}. \quad (\text{A.33})$$

Mathematically it is hard to define a PSD through the DFT series $H[n]$, since it is only defined in discrete frequencies. However PSD estimation is helpful in some discrete problems like in this thesis, a concept of Empirical Power Spectral Density (EPSD) $\mathcal{ED}[n]$ which donates:

$$\sum_{k_i=-\infty}^{N-1} |h[k_i]|^2 = \sum_{n=-\infty}^{N-1} |H[n]|^2 = \sum_{n=0}^{N-1} \mathcal{ED}[n] \Delta f, \quad (\text{A.34})$$

and the EPSD can be computed as:

$$\mathcal{ED}[n] = \frac{|H[n]|^2}{N^2 \Delta f}. \quad (\text{A.35})$$

Eq. (A.35) is a general definition of PSD in "Matlab", however, for big data series, a optimized and smoothed process can help to make the estimation clear as well as more efficient. That is why the windowing is introduced in the function of "pwelch".

A.2.1 Windowed PSD

Consider that a finite range discrete time signal equals an infinite time signal $h[k_i]$ multiplied by a rectangular time window function $r[k]$ as:

$$h^w[k_i] = h[k_i] r[k_i] \quad (\text{A.36})$$

where the window function writes for example:

$$r[k_i] = \begin{cases} 1 & \text{if } 0 \leq k_i \leq N - 1 \\ 0 & \text{if } k_i \geq N \end{cases} \quad (\text{A.37})$$

Use the Fourier Transform for all the terms in Eq. (A.36), then discrete Fourier series can be expressed as:

$$H^w[n] = \sum_{l=0}^{N-1} H[l]R[n-l], \quad (\text{A.38})$$

which generated an finite range of signals. With a variety in non zero range of window function like $r[k_i]$, the finite windowed range moves, that covers the whole range of to be analyzed signal. Using different window functions $r[k_i]$ can reduce the effect of *leakage*, which is named as the distribution between the adjacent frequencies. Available window functions like Hanning, Flattop, Blackman-Harris are not discussed here, but can be tried in defining the structure of "pwelch". Overlapping of two neighboring windowed range also turns to be a parameter that controls the final results.

With help of Eq. (A.38), the Power Spectrum of the windowed signal $h^w[k]$ can be transformed from Eq. (A.33) to:

$$\mathcal{D}^w(n) = \frac{|H^w[n]|^2}{N^2}. \quad (\text{A.39})$$

Also by normal computation a EPSPD is used, like in this thesis:

$$\mathcal{ED}[n] = \frac{|H^w[n]|^2}{ENBW}. \quad (\text{A.40})$$

where the ENBW called *Equivalent Noise Band Width* and defines as:

$$ENBW = \frac{\sum_{k_i=0}^{N-1} r^2[k_i]}{(\sum_{k_i=0}^{N-1} r[k_i])^2} N \Delta f, \quad (\text{A.41})$$

Bibliography

- [1] A.S. Hersh, B.E. Walker, and J.W. Celano. Helmholtz resonator impedance model, part 1: Nonlinear behavior. *AIAA journal*, 41(5):795–808, 2003.
- [2] P.K. Tang and W.A. Sirignano. Theory of a generalized Helmholtz Resonator. *Journal of Sound and Vibration*, 26(2):247–262, 1973.
- [3] J.J. Keller and E. Zauner. On the use of Helmholtz Resonators as sound attenuators. *Zeitschrift für angewandte Mathematik und Physik ZAMP*, 46(3):297–327, 1995.
- [4] K. Förner, M.A. Temiz, W. Polifke, and I.L. Arteaga. On the non-linear influence of the edge geometry on vortex shedding in Helmholtz Resonators. 2015.
- [5] K. Förner, J. Tournadre, P. Martínez-Lera, and W. Polifke. Characterization of the nonlinear response of a Helmholtz Resonator. In N. A. Adams, R. Radespiel, T. Sattelmayer, W. Schröder, and B. Weigand, editors, *Annual Report*, pages 33 – 45. Sonderforschungsbereich/Transregio 40, 2015.
- [6] K. Förner and W. Polifke. Aero-Acoustic Characterization of Helmholtz Resonators in the Linear Regime with System Identification. In *22nd International Congress on Sound and Vibration (ICSV22)*, Florence, Italy, 12 - 16 July 2015.
- [7] Q. Zhang and D.J. Bodony. Numerical investigation and modelling of acoustically excited flow through a circular orifice backed by a hexagonal cavity. *Journal of Fluid Mechanics*, 693:367–401, 2012.
- [8] L. Davidson. How to estimate the resolution of an les of recirculating flow. In *Quality and Reliability of Large-Eddy Simulations II*, pages 269–286. Springer, 2011.
- [9] J. Smagorinsky. General circulation experiments with the primitive equations: I. the basic experiment*. *Monthly weather review*, 91(3):99–164, 1963.
- [10] A.N. Kolmogorov. The local structure of turbulence in incompressible viscous fluid for very large reynolds numbers. *Proceedings: Mathematical and Physical Sciences*, pages 9–13, 1991.
- [11] L. Davidson. Fluid mechanics, turbulent flow and turbulence modeling, lecture notes in msc courses. Technical report, Chalmers University of Technology, 2010.
- [12] S.B. Pope. *Turbulent flows*. Cambridge university press, 2000.

- [13] E. De Villiers. *The potential of large eddy simulation for the modelling of wall bounded flows*. 2006.
- [14] G.T. Mase, R.E. Smelser, R.M. Smelser, and G.E. Mase. *Continuum mechanics for engineers*. CRC series in computational mechanics and applied analysis. Taylor and Francis, 2009.
- [15] A. Cabrena. Linear system identification of the heat transfer behavior of a cylinder in pulsating cross-flow at $Re = 3900$ using large eddy simulation. Master's thesis, Technische Universität München, 2015.
- [16] C. Wagner, T. Hüttl, and P. Sagaut. *Large-eddy simulation for acoustics*, volume 20. Cambridge University Press, 2007.
- [17] A. W. Vreman. *Direct and large-eddy simulation of the compressible turbulent mixing layer*. University of Twente, 1995.
- [18] B. Vreman, B. Geurts, and H. Kuerten. Subgrid-modelling in les of compressible flow. *Applied scientific research*, 54(3):191–203, 1995.
- [19] A. Yoshizawa. Statistical theory for compressible turbulent shear flows, with the application to subgrid modeling. *Physics of Fluids (1958-1988)*, 29(7):2152–2164, 1986.
- [20] C. Fureby, A.D. Gosman, G. Tabor, H.G. Weller, N. Sandham, and M. Wolfshtein. Large eddy simulation of turbulent channel flows. *Turbulent shear flows*, 11:28–13, 1997.
- [21] U. Germano, M. and Piomelli, P. Moin, and W.H. Cabot. A dynamic subgrid-scale eddy viscosity model. *Physics of Fluids A: Fluid Dynamics (1989-1993)*, 3(7):1760–1765, 1991.
- [22] U. Piomelli. Large-eddy simulation: achievements and challenges. *Progress in Aerospace Sciences*, 35(4):335–362, 1999.
- [23] D.K. Lilly. A proposed modification of the germano subgrid-scale closure method. *Physics of Fluids A: Fluid Dynamics (1989-1993)*, 4(3):633–635, 1992.
- [24] S. Ghosal, T. S. Lund, P. Moin, and K. Akselvoll. A dynamic localization model for large-eddy simulation of turbulent flows. *Journal of Fluid Mechanics*, 286:229–255, 1995.
- [25] U. Piomelli, W.H. Cabot, P. Moin, and S. Lee. Subgrid-scale backscatter in turbulent and transitional flows. *Physics of Fluids A: Fluid Dynamics (1989-1993)*, 3(7):1766–1771, 1991.
- [26] J.W. Deardorff. A numerical study of three-dimensional turbulent channel flow at large reynolds numbers. *Journal of Fluid Mechanics*, 41(02):453–480, 1970.

BIBLIOGRAPHY

- [27] C. Fureby, G. Tabor, H.G. Weller, and A.D. Gosman. Differential subgrid stress models in large eddy simulations. *Physics of Fluids (1994-present)*, 9(11):3578–3580, 1997.
- [28] P.R. Spalart and S.R. Allmaras. A one equation turbulence model for aerodynamic flows. *AIAA Journal*, 94-0439, 1992.
- [29] G.A. Ashford and K.G. Powell. An unstructured grid generation and adaptive solution technique for high-reynolds-number compressible flows. *Lecture series-van Karemman Institute for fluid dynamics*, 6:J1–J110, 1996.
- [30] M.A. Cárdenas. *Influence of Enhanced Heat Transfer in Pulsating Flow on the Damping Characteristics of Resonator Rings*. Dissertation, Technische Universität München, München, 2014.
- [31] T.J. Poinso and S.K. Lele. Boundary conditions for direct simulations of compressible viscous flows. *Journal of computational physics*, 101(1):104–129, 1992.
- [32] G. Sebastian. Changes and settings for standard turbulence model implementation in openfoam (special in spalartallmara), <http://turbmodels.larc.nasa.gov/changestoopenfoam.pdf>. 2014.
- [33] U. Ingard and H. Ising. Acoustic nonlinearity of an orifice. *The journal of the Acoustical Society of America*, 42(1):6–17, 1967.
- [34] W. Sutherland. The viscosity of gases and molecular force. *The London, Edinburgh, and Dublin Philosophical Magazine and Journal of Science*, 36(223):507–531, 1893.
- [35] A. Miranda. *Identification of Sound Sources in Duct Singularities*. Dissertation, Technische Universität München, München, 2016.